

1

# Suitably impressive thesis title

2



3

Mikkel Bjørn

4

St. Anne's College

5

University of Oxford

6

A thesis submitted for the degree of

7

*Doctor of Philosophy*

8

Trinity 2020

## Acknowledgements

10 suitable thank you's

# Abstract

11

<sup>12</sup> World's best measurement of  $\gamma$ . Details to be added.

# Contents

13

14	<b>Preface</b>	vii
15	<b>1 Theoretical background</b>	1
16	1.1 The C, P and T symmetries and their violation . . . . .	1
17	1.2 CP violation in the Standard Model . . . . .	3
18	1.2.1 The CKM matrix and the Unitarity Triangle . . . . .	4
19	1.2.2 Measuring $\gamma$ in tree level decays . . . . .	7
20	1.3 Measuring $\gamma$ using multi-body D final states . . . . .	11
21	1.3.1 Dalitz plots and the phase space of multi-body decays . . . . .	11
22	1.3.2 The GGSZ method to measure $\gamma$ . . . . .	13
23	1.3.3 A model-independent approach . . . . .	15
24	1.3.4 Measuring strong-phase inputs at charm factories . . . . .	17
25	1.3.5 Global CP asymmetry and the relation to GLW and ADS measurements . . . . .	21
26	1.4 Strategy for the LHCb measurement . . . . .	25
28	<b>2 The LHCb experiment</b>	28
29	2.1 Subdetectors . . . . .	28
30	2.1.1 The VELO . . . . .	28
31	2.1.2 Magnet and tracking stations . . . . .	28
32	2.1.3 The RICH . . . . .	28
33	2.1.4 Calorimeters . . . . .	28
34	2.1.5 Muon detectors . . . . .	28
35	2.2 Track reconstruction . . . . .	28
36	2.3 The LHCb triggering system . . . . .	28
37	2.3.1 The level-0 hardware trigger . . . . .	28
38	2.3.2 High-level triggers . . . . .	28
39	2.3.3 Offline data filtering: the LHCb stripping . . . . .	28
40	2.4 Simulation . . . . .	28

41	<b>3 Neutral kaon <math>CP</math> violation and material</b>	30
42	<b>interaction in BPGGSZ measurements</b>	
43	3.1 CP violation and material interaction of neutral kaons . . . . .	30
44	3.1.1 A first look at the impact on $\gamma$ measurements . . . . .	34
45	3.2 Impact on BPGGSZ measurements of $\gamma$ :	
46	principles . . . . .	36
47	3.2.1 Modified symmetry relations . . . . .	36
48	3.2.2 Relationship between the $K_S^0$ and $K_L^0$ amplitudes . . . . .	37
49	3.2.3 Modification of the BPGGSZ yield equations . . . . .	38
50	3.3 Impact on BPGGSZ measurements of $\gamma$ :	
51	LHCb and Belle II measurements . . . . .	41
52	3.3.1 Detector geometries . . . . .	42
53	3.3.2 Kaon momentum distributions . . . . .	43
54	3.3.3 Experimental time acceptance . . . . .	44
55	3.3.4 Detector material budget . . . . .	45
56	3.3.5 Calculation procedure . . . . .	47
57	3.3.6 Results . . . . .	48
58	3.3.7 Coupled $B^\pm \rightarrow DK^\pm$ and $B^\pm \rightarrow D\pi^\pm$ measurements . . . . .	50
59	3.4 Concluding remarks . . . . .	51
60	<b>4 A BPGGSZ measurement with <math>B^\pm \rightarrow Dh^\pm</math> decays</b>	53
61	4.1 Candidate reconstruction and selection . . . . .	53
62	4.1.1 Initial requirements . . . . .	54
63	4.1.2 Boosted decision tree . . . . .	56
64	4.1.3 Particle-identification requirements . . . . .	61
65	4.1.4 Final requirements . . . . .	63
66	4.1.5 Selected candidates . . . . .	64
67	4.2 Background studies . . . . .	64
68	4.2.1 Charmless decays . . . . .	66
69	4.2.2 Background from four-body $D$ decays . . . . .	68
70	4.2.3 Semi-leptonic backgrounds . . . . .	68
71	4.2.4 Cross-feed from other $D \rightarrow K_S^0 h^+ h^-$ decays . . . . .	75
72	4.2.5 Swapped-track backgrounds . . . . .	77
73	4.3 Signal and background mass shapes . . . . .	78
74	4.3.1 Signal decays . . . . .	79
75	4.3.2 Cross-feed between $B^\pm \rightarrow Dh^\pm$ channels . . . . .	80
76	4.3.3 Partially reconstructed backgrounds . . . . .	83
77	4.3.4 Combinatorial background . . . . .	88
78	4.3.5 Fit results . . . . .	88

79	4.4	Measurement of the CP-violation observables . . . . .	90
80	4.4.1	Fit setup . . . . .	92
81	4.4.2	Main results . . . . .	95
82	4.4.3	Cross checks . . . . .	98
83	4.5	Systematic uncertainties . . . . .	105
84	4.5.1	Mass shapes . . . . .	105
85	4.5.2	Charmless backgrounds . . . . .	105
86	4.6	Obtained constraints on $\gamma$ . . . . .	105
87	<b>Appendices</b>		
88	<b>A</b>	<b>Projections of main fit to data</b>	<b>107</b>
89	<b>Bibliography</b>		<b>108</b>

# Preface

91 The work presented in this thesis has been resulted in two papers, either under  
 92 review or published in the Journal of High Energy Physics. These are

93 [1] *Measurement of the CKM angle  $\gamma$  using  $B^\pm \rightarrow [K_S^0 h^+ h^-]_D h^\pm$  decays,*  
 94 submitted to JHEP.

95 This paper describes a measurement of the CKM angle  $\gamma$  using  $pp$  collision  
 96 data taken with the LHCb experiment during the Run 1 of the LHC, in 2011  
 97 and 2012, and during the full Run 2, in 2015–2018. The measurement uses the  
 98 decay channels  $B^\pm \rightarrow D h^\pm$  where  $D \rightarrow K_S^0 h'^+ h'^-$ , in which  $h$  and  $h'$  denotes  
 99 pions or kaons. It obtains a value of  $\gamma = (? \pm ?)^\circ$ , which constitutes the world's  
 100 best single-measurement determination of  $\gamma$ . The work is the main focus of  
 101 this thesis and described in detail in Chapter 4.

102 [2] *CP violation and material interaction of neutral kaons in measurements*  
 103 *of the CKM angle  $\gamma$  using  $B^\pm \rightarrow D K^\pm$  decays where  $D \rightarrow K_S^0 \pi^+ \pi^-$* , JHEP  
 104 19 (2020) 106.

105 This paper describes a phenomenological study of the impact of neutral  
 106 kaon  $CP$  violation and material interaction on measurements of  $\gamma$ . With the  
 107 increased measurement precision to come in the near future, an understanding  
 108 of these effects is crucial, especially in the context of  $B \rightarrow D\pi$  decays; however  
 109 no detailed study had been published at the start of this thesis. The study is  
 110 the subject of Chapter 3. Some text excerpts and figures from the paper have  
 111 been reproduced in the thesis.

112 All of the work described in this thesis is my own, except where clearly referenced  
 113 to others. Furthermore, I contributed significantly to an analysis of  $B^\pm \rightarrow D K^\pm$   
 114 decays with LHCb data taken in 2015 and 2016, now published in

115 [3] *Measurement of the CKM angle  $\gamma$  using  $B^\pm \rightarrow D K^\pm$  with  $D \rightarrow K_S^0 \pi^+ \pi^-$*   
 116  *$K_S^0 K^+ K^-$  decays*, JHEP 08 (2018) 176.

117 I was responsible for the analysis of the signal channel, whereas the control channel  
 118 was analysed by Nathan Jurik. The measurement is superseded by that of Ref. [1]  
 119 and is not described in detail in the thesis.

# 1

120

121

## Theoretical background

122 This chapter lays out the theoretical framework of the thesis. Section 1.1 introduces  
123 charge and parity symmetry violation in general, while Section 1.2 covers the  
124 description in the Standard Model and the general theory behind charge-parity  
125 symmetry violation measurements in charged  $B$  decays. Section 1.3 focuses on  
126 the theory of measurements using  $B^\pm \rightarrow Dh^\pm$  decays with multi-body  $D$  final  
127 states, after which the specific analysis strategy for the measurement described  
128 in the thesis is outlined out in Section 1.4.

### 129 **1.1 The C, P and T symmetries and their vio-** 130 **lation**

131 The concept of symmetry play a fundamental role in modern physics. By Noether's  
132 theorem [4], the simple assumption of invariance of our physical laws under universal  
133 temporal and spatial translations leads to the very non-trivial prediction of conserved  
134 energy and momentum; within the field of particle physics, the interactions and  
135 dynamics of the Standard Model (SM) follow completely simply from requiring  
136 the fundamental particle fields to satisfy a local  $U(1) \times SU(2) \times SU(3)$  gauge  
137 symmetry [5]; and one of the short-comings of the SM, is that it fails to explain  
138 the apparent *lack* of symmetry in our matter-dominated universe [6]. Indeed, it is  
139 important to experimentally establish the symmetries of our world at a fundamental  
140 level, and the degree to which they are broken.

141 Three discrete symmetries of importance are the symmetries under

I'll  
adjust  
this para-  
graph  
when  
I've  
written  
the intro-  
duction.

- 142     1. The charge operator  $C$ , which conjugates all internal quantum numbers of a  
 143       quantum state and thus converts particles into their anti-particle counter parts.  
 144       For example,  $C$  transforms the electric charge of a particle state  $Q \rightarrow -Q$ .
- 145     2. The parity operator  $P$ , which inverts the spatial dimensions of space time:  
 146        $\vec{x} \rightarrow -\vec{x}$ . As such, it transforms left-handed particle fields into right-handed  
 147       particle fields and vice versa.
- 148     3. The time-inversion operator  $T$ , which inverts the temporal dimension of space  
 149       time:  $t \rightarrow -t$ .

150     These are fundamentally related by the *CPT* theorem [7] , which states that any  
 151       Lorentz-invariant Quantum Field Theory (QFT) must be symmetric under the  
 152       simultaneous application of *all* three operators. However, any one of the symmetries  
 153       can be broken individually, and experiments have shown the physical laws of our  
 154       world to violate each of the  $C$ ,  $P$ , and  $T$  symmetries.

155     Such a symmetry-breaking effect was established for the first time in 1956, when  
 156       Chien-Shiung Wu observed parity violation in weak decays of Co-60 nuclei [8], after  
 157       carrying out an experiment that was proposed by Yang Chen-Ning and Tsung-Dao  
 158       Lee [9]. While this experiment established the breaking of  $P$  symmetry, it left open  
 159       the possibility that the physical laws are invariant under a combination of a charge-  
 160       and parity inversion; that they are *CP* symmetric. However, this was disproved in  
 161       1964 when Kronin and Fitch observed that long-lived kaons, which predominantly  
 162       decay to the *CP*-odd  $3\pi$  state, could also decay to the *CP*-even  $\pi\pi$  states [10].

163     Since then *CP* violation has been found in the  $B^0$  system by the BaBar and Belle  
 164       collaborations [11,12] during the early 2000's; the  $B$  factories, along with CDF, also  
 165       saw evidence for *CP* violation in  $B^\pm$  decays [13–18] later confirmed by LHCb [19],  
 166       and *CP* violation was measured for the  $B_s^0$  meson by LHCb in 2013 [20]; within the  
 167       last year and a half, the first observation of *CP*-violation in  $D^0$  decays has also been  
 168       made by the LHCb collaboration [21], and most recently evidence for *CP*-violation in  
 169       the neutrino sector has been reported by the T2K collaboration [22]. The observed  
 170       effects can be divided into distinct classes. The conceptually simplest case is

- 171     1. *CP-violation in decay*, where  $|A/\bar{A}| \neq 1$  for some decay amplitude  $A$ , and the  
 172       amplitude  $\bar{A}$  of the *CP*-conjugate decay. The result is different decay rates in  
 173       two *CP*-conjugate decays

$$\Gamma(M \rightarrow f) \neq \Gamma(\bar{M} \rightarrow \bar{f}). \quad (1.1)$$

This type of  $CP$  violation was not seen until the late 1980ies [23, 24], more than 20 years after the first observation of  $CP$  violation, and only finally established around the year 2000 [25, 26]. Also this discovery was made in  $K \rightarrow \pi\pi$  decays.

$CP$ -violation in decay is the only type possible for charged initial states, and it is thus the main focus of the thesis. Two additional  $CP$ -violating effect are possible for neutral initial states (a situation that will be the main focus of Chapter 3). These effects are

2.  $CP$ -violation in mixing, which denotes the case where the mixing rates between the  $M^0$  and  $\bar{M}^0$  states differ

$$\Gamma(M^0 \rightarrow \bar{M}^0) \neq \Gamma(\bar{M}^0 \rightarrow M^0). \quad (1.2)$$

The  $CP$  violation first observed by Kronin and Fitch in the neutral kaon sector [10] is (dominantly) of this type.

3.  $CP$ -violation in interference between mixing and decay, which can be present for a neutral initial states  $M^0$  decaying into a final state  $f$  common to both  $M^0$  and  $\bar{M}^0$ . The decay rate includes an interference term between two amplitudes: the amplitude for a direct  $M^0 \rightarrow f$  decay and the amplitude for a decay after mixing:  $M^0 \rightarrow \bar{M}^0 \rightarrow f$ . Even in the absence of the two aforementioned effects, the rates  $\Gamma(M^0 \rightarrow f)$  and  $\Gamma(\bar{M}^0 \rightarrow \bar{f})$  can differ due to the interference term. Such  $CP$  asymmetries have been measured in eg.  $B^0 \rightarrow J/\psi K$  by LHCb and the  $B$  factories, and in  $B_s^0 \rightarrow J/\psi \phi$  decays by the LHC and Tevatron experiments [27].

$CP$  violation measurements thus have a long, rich, and still-developing history.

## 1.2 CP violation in the Standard Model

All existing measurements of  $CP$  violation in the quark sector are naturally explained in the SM; indeed, the need to explain the observation  $CP$  violation in neutral kaons was a driving force in the development of the model in the first place, when it lead Kobayashi and Maskawa to predict the existence of then-unknown particles in 1973 [28] (now known to be the third generation quarks).

### 1.2.1 The CKM matrix and the Unitarity Triangle

The SM contains three generations of quarks, each consisting of an up-type quark ( $u$ ,  $c$ , and  $t$ ) and a down-type quark ( $d$ ,  $s$ , and  $b$ ). The charged weak interaction of the  $W^\pm$  boson couples up and down-type quarks. The quark states that couple to the  $W$  are not (a priori) identical to the mass eigenstates, and can be denoted  $(u', c', \text{ and } t')$  and  $(d', s', \text{ and } b')$ . A basis for the quark states can be chosen such that the weakly coupling up-quark states are identical to the propagating quark states,  $u = u'$ , but then the down-type quark state are different:  $d' \neq d$ . The two bases of the down-type quarks are related via the Cabibbo-Kobayashi-Maskawa (CKM) matrix [28, 29]<sup>1</sup>

$$\begin{pmatrix} d' \\ s' \\ t' \end{pmatrix} = V \begin{pmatrix} d \\ s \\ t \end{pmatrix} = \begin{pmatrix} V_{ud} & V_{us} & V_{ub} \\ V_{cd} & V_{cs} & V_{cb} \\ V_{td} & V_{ts} & V_{tb} \end{pmatrix} \begin{pmatrix} d \\ s \\ t \end{pmatrix}. \quad (1.3)$$

Thus the Lagrangian terms representing the coupling of a  $W^\pm$  boson with a  $u$ - and a  $d$ -type quark is

$$\mathcal{L}_{W^+} = -\frac{g}{\sqrt{2}} V_{ud} (\bar{u} \gamma^\mu W_\mu^+ d) \quad \mathcal{L}_{W^-} = -\frac{g}{\sqrt{2}} V_{ud}^* (\bar{d} \gamma^\mu W_\mu^- u) \quad (1.4)$$

where  $g$  is the weak coupling constant,  $\gamma_u$  are the Dirac matrices, and  $u$  and  $d$  represent the left-handed components of the physical quark states.

The CKM matrix is a unitary complex  $3 \times 3$  matrix, and hence has  $3^2 = 9$  independent, real parameters. However, 5 of these can be absorbed into non-physical phases of the quark states (both mass and weak eigenstates) and hence the matrix has 4 real, physical parameters: 3 mixing angles and a single phase. Chau and Keung [30] proposed the parameterisation

$$V = \begin{pmatrix} 1 & 0 & 0 \\ 0 & c_{23} & s_{23} \\ 0 & -s_{23} & c_{23} \end{pmatrix} \begin{pmatrix} c_{13} & 0 & s_{13}e^{-i\delta_{CP}} \\ 0 & 1 & 0 \\ -s_{13}e^{-i\delta_{CP}} & 0 & c_{13} \end{pmatrix} \begin{pmatrix} c_{12} & s_{12} & 0 \\ -s_{12} & c_{12} & 1 \\ 0 & 0 & 1 \end{pmatrix} \\ = \begin{pmatrix} c_{12}c_{13} & s_{12}c_{13} & s_{13}e^{-i\delta_{CP}} \\ -s_{12}c_{23} - c_{12}s_{23}s_{13}e^{i\delta_{CP}} & c_{12}c_{23} - s_{12}s_{23}s_{13}e^{i\delta_{CP}} & s_{23}c_{13} \\ s_{12}s_{23} - c_{12}c_{23}s_{13}e^{i\delta_{CP}} & -c_{12}s_{23} - s_{12}s_{23}s_{13}e^{i\delta_{CP}} & c_{23}c_{13} \end{pmatrix} \quad (1.5)$$

which is the preferred standard by the PDG [31]. Here,  $s_{ij} \equiv \sin \theta_{ij}$  and  $c_{ij} \equiv \cos \theta_{ij}$  denote the sine and cosine of three rotation angles in quark space;  $\theta_{12} = \theta_C$  being the usual Cabibbo angle [29].

<sup>1</sup> A basis for the quarks can of course be chosen, such that neither the up-quarks or the down-quarks are expressed in their mass eigenstates. In that case the CKM matrix is recovered as  $V = U_u^* U_d$ , where  $U_{u/d}$  is the unitary transformation matrices that brings the  $u/d$  quarks into their mass eigenstates.

The presence of the complex phase  $\delta_{CP}$  in the Lagrangian term of the  $W$  coupling causes  $CP$  violation because, as evident from Eq. (1.4), if  $\delta_{CP}$  enters the amplitude for some decay mediated by a  $W$  boson,  $A = |A|e^{i(\delta_0 + \delta_{CP})}$ , then it will enter the  $CP$  conjugate decay amplitude with the opposite sign:  $\bar{A} = |A|e^{i(\delta_0 - \delta_{CP})}$ . In these expressions,  $\delta_0$  denotes a  $CP$  conserving phase that is not caused by complex terms in the Lagrangian, but arises due to potential intermediate states in the decay amplitude.<sup>2</sup> Usually the underlying mechanism is due to QCD effects, and these  $CP$  conserving phases are therefore generally dubbed *strong* phases, as opposed to the  $CP$  violating *weak* phase of the  $W$  coupling [31]. This terminology will be applied throughout the thesis.

Experimentally, it has been observed that the CKM matrix elements of Eq. (1.5) satisfy  $s_{13} \ll s_{23} \ll s_{12}$ . This motivates an often used, alternative parameterisation of the matrix, where the elements are expressed as power series in a parameter  $\lambda$  that naturally incorporates this hierarchy: the Wolfenstein parameterisation [32]. The definitions

$$\begin{aligned} s_{12} &\equiv \lambda \\ s_{23} &\equiv \lambda^2 A \\ s_{13} &\equiv \lambda^3 (\rho - i\eta) \end{aligned} \tag{1.6}$$

are made, after which the unitarity conditions (or Eq. 1.5) determine the remaining elements to any order in  $\lambda$ .<sup>3</sup> To  $\mathcal{O}(\lambda^5)$  the Wolfenstein parameterisation of the CKM matrix is [34, 35]

$$V = \begin{pmatrix} 1 - \frac{\lambda^2}{2} - \frac{\lambda^4}{8} & \lambda & A\lambda^3(\rho - i\eta) \\ -\lambda + \frac{\lambda^5}{2}A^2(1 - 2(\rho + i\eta)) & 1 - \frac{\lambda^2}{2} - \frac{\lambda^4}{8}(1 + 4A^2) & A\lambda^2 \\ A\lambda^3(1 - (\rho + i\eta)(1 - \frac{\lambda^2}{2})) & -A\lambda^2(1 - \frac{\lambda^2}{2}(1 - 2(\rho + i\eta))) & 1 - \frac{1}{2}A^2\lambda^4 \end{pmatrix}. \tag{1.7}$$

The unitarity condition  $V^\dagger V = \mathbb{1}$  of the CKM matrix defines 9 relations between the CKM elements of the form

$$\sum_j V_{jq}^* V_{jq} = 1 \quad , \quad q \in \{d, s, b\} \quad \text{along the diagonal} \tag{1.8a}$$

$$\sum_j V_{jq}^* V_{jq'} = 0 \quad , \quad q, q' \in \{d, s, b\}, q \neq q' \quad \text{off-diagonal.} \tag{1.8b}$$

---

<sup>2</sup>It is generally true that all phases of a single term in a given amplitude will be convention dependent, but that the phase differences between terms are not.

<sup>3</sup>Other variants of the Wolfenstein parameterisation do exist [33]. They all agree at the lowest orders of  $\lambda$ .

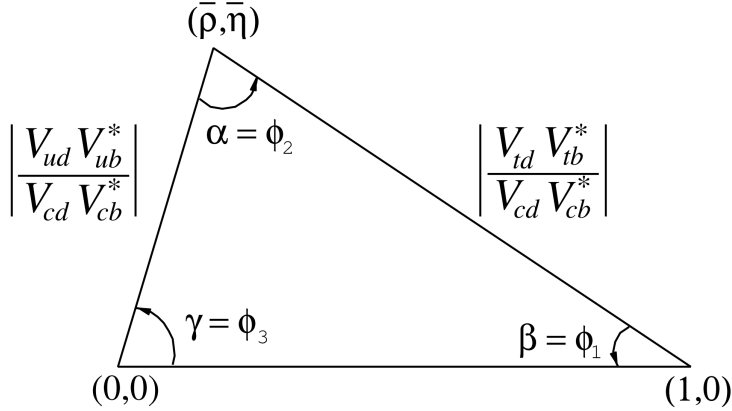


**Figure 1.1:** Definition of the lengths and sides of the Unitarity Triangle. Figure is taken from the *CKM Quark-Mixing Matrix* review of the PDG [31].

The off-diagonal conditions constrain three complex numbers to sum to zero, and can thus be visualised as triangles in the complex plane, the so-called unitarity triangles. Of these, the triangle corresponding to the  $(d, b)$  elements plays a special role, because all three sides are of the same order of magnitude,  $\mathcal{O}(\lambda^3)$ . When expressed in the form

$$\frac{V_{ud}^* V_{ub}}{V_{cd}^* V_{cb}} + \frac{V_{td}^* V_{tb}}{V_{cd}^* V_{cb}} + 1 = 0, \quad (1.9)$$

it is often referred to as the singular Unitarity Triangle, illustrated in Fig. 1.1 where the usual names for the three angles are also given.

Over-constraining the unitarity triangle by making separate measurements of all sides and angles, in as many different decay channels as possible, is an important, and non-trivial test of the SM. The current experimental constraints are in agreement with the SM predictions, as visualised in Fig. 1.2. The CKM angle

$$\gamma \equiv \arg(-V_{ud}V_{ub}^*/V_{cd}V_{cb}^*) = \arg(-V_{cb}V_{cd}^*/V_{ub}V_{ud}^*) \quad (1.10)$$

is unique among the CKM parameters, in that it can be measured in tree-level processes without significant theoretical uncertainty from lattice QCD calculations [36]. Because tree-level processes are less likely to be affected by Beyond-Standard-Model (BSM) effects, direct measurements of  $\gamma$  can be considered a SM benchmark, which can be compared to estimates based on measurements of other CKM elements that are measured in loop-level processes, and thus are more likely to be affected by BSM effects [37]. The current, worldwide combination of direct measurements, published by the CKMFitter group, is  $\gamma = (72.1^{+5.4}_{-5.7})^\circ$ , to be compared with the estimate from loop-level observables of  $\gamma = (65.66^{+0.90}_{-2.65})^\circ$  [38]. Other world averages

Not sure if I should spend time explaining the non-gamma measurements entering?

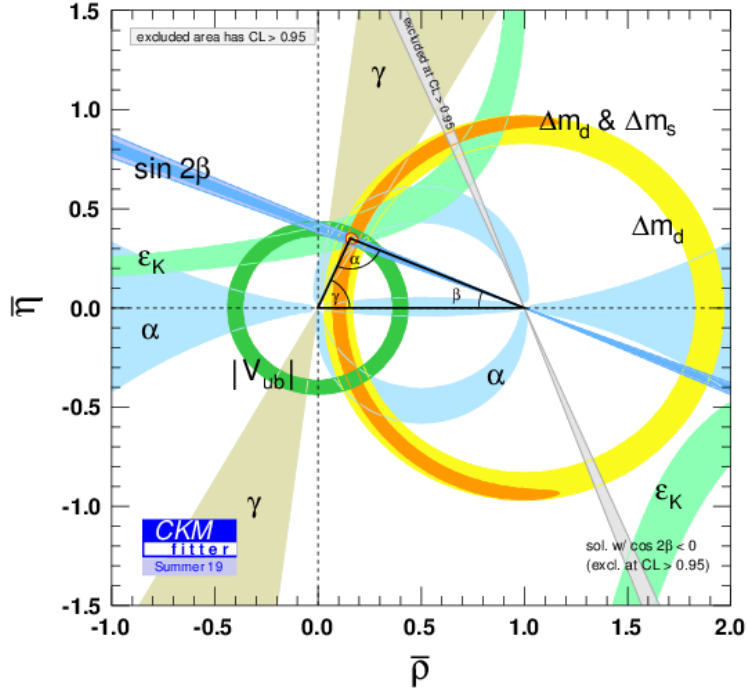


**Figure 1.2:** Current constraints on the Unitarity Triangle parameters as determined by the CKMFitter group for the EPS 2019 conference [38].

exist [27, 39], but the overall picture is the same: the ability to constrain BSM physics is currently limited by the uncertainty of the direct measurements. Hence further precision measurements of  $\gamma$  are highly motivated. Presently, the precision is driven by time-integrated measurements of direct  $CP$ -violation in  $B^\pm \rightarrow DK^\pm$  decays; such a measurement is the topic of this thesis and the theory behind is treated in detail in the following section. It is also possible to measure  $\gamma$  in time-dependent mixing analyses of  $B_s^0 \rightarrow D_s^\mp K^\pm$ ,  $B^0 \rightarrow D^\mp \pi^\pm$  and related decays, by measuring  $CP$  violation in interference between mixing and decay. These modes are expected to provide competitive measurements in the future [40, 41].

### 1.2.2 Measuring $\gamma$ in tree level decays

The phase  $\gamma$  can be measured in tree-level processes with interference between  $b \rightarrow c\bar{s}u$  and  $b \rightarrow \bar{c}s u$  transitions. The canonical example, also the subject of this thesis, is based on measurements sensitive to interference between the  $B^\pm \rightarrow D^0 K^\pm$  and  $B^\pm \rightarrow \bar{D}^0 K^\pm$  decay amplitudes. As illustrated in Fig. 1.3 for the case of  $B^-$  decays, the electro-weak phase difference between the two decays

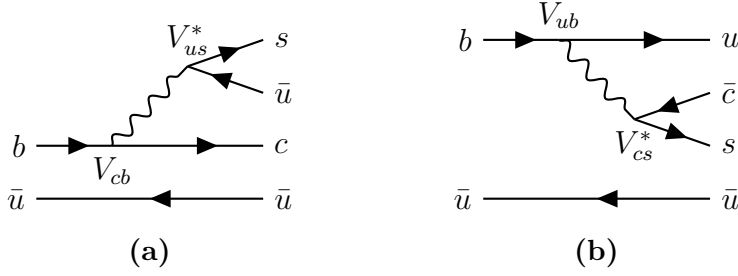


**Figure 1.3:** Tree level Feynman diagrams describing (a)  $B^- \rightarrow D^0 K^-$  and (b)  $B^- \rightarrow \bar{D}^0 K^-$  decays. The electro-weak phase difference between the two decays is  $\Delta\phi = \arg(V_{cb}V_{us}^*/V_{ub}V_{cs}^*) \simeq \gamma$ .

is  $\Delta\phi = \arg(V_{cb}V_{us}^*/V_{ub}V_{cs}^*)$ . While  $\Delta\phi$  is not identical to the definition of  $\gamma$  in Eq. (1.10), the ratio of the involved CKM matrix elements is [42]

$$\begin{aligned} -\frac{V_{cd}^*/V_{ud}^*}{V_{us}^*/V_{cs}^*} &= -\frac{-\lambda[1 - \frac{\lambda^4}{2}A^2(1 - 2(\rho - i\eta))](1 - \frac{\lambda^2}{2} - \frac{\lambda^4}{8}(1 + 4A^2))}{\lambda(1 - \frac{\lambda^2}{2} - \frac{\lambda^4}{4})} \\ &= 1 - \lambda^4 A^2(1 - 2(\rho - i\eta)) + \mathcal{O}(\lambda^5). \end{aligned} \quad (1.11)$$

The ratio equals unity to  $\mathcal{O}(\lambda^4) \simeq 2.6 \times 10^{-3}$ , and thus  $\Delta\phi \simeq \gamma$  is a good approximation within current experimental uncertainties. For the remainder of this thesis the approximation will be used without further comment. The diagrams in Fig. 1.3 describe the leading order contributions to the two amplitudes

$$\begin{aligned} A[B^- \rightarrow D^0 K^-] &\equiv A_B \\ A[B^- \rightarrow \bar{D}^0 K^-] &\equiv \bar{A}_B \equiv r_B A_B e^{i(\delta_B - \gamma)}, \end{aligned} \quad (1.12a)$$

where the last equality introduces two new parameters: the amplitude magnitude ratio  $r_B \equiv |\bar{A}_B|/|A_B|$ , and  $\delta_B$ , the strong-phase difference between the decay amplitudes. Since all  $CP$ -violation is attributed to the electro-weak phase in the SM, the  $CP$ -conjugate decay amplitudes are [43]

$$\begin{aligned} A[B^+ \rightarrow \bar{D}^0 K^+] &= A_B \\ A[B^+ \rightarrow D^0 K^+] &= \bar{A}_B = r_B A_B e^{i(\delta_B + \gamma)}. \end{aligned} \quad (1.12b)$$

In an experimental setting, the  $D^0$  and  $\bar{D}^0$  mesons are reconstructed in some final state,  $f$  or its  $CP$ -conjugate  $\bar{f}$ . In analogy with the  $B^\pm$  decays, the  $D$  decay amplitude can be related<sup>4</sup>

$$\begin{aligned} A[D^0 \rightarrow f] &= A[\bar{D}^0 \rightarrow \bar{f}] = A_D \\ A[\bar{D}^0 \rightarrow f] &= A[D^0 \rightarrow \bar{f}] = r_D A_D e^{i\delta_D}. \end{aligned} \quad (1.13)$$

<sup>4</sup>In this notation  $\delta_D$  is thus phase of the suppressed  $D$ -decay amplitude minus the phase of the favoured  $D$ -decay amplitude. This is the opposite convention to that used in the LHCb measurements with the ADS technique, but aligns with the notation used in the literature on  $\gamma$  measurements in  $D \rightarrow K_S^0 \pi^+ \pi^-$  decays.

where the assumption has been made that  $CP$  violation in the  $D$  decays is negligible, and  $\delta_D$  denotes a  $CP$ -conserving strong-phase difference. While  $CP$ -violation in  $D$  decays has recently been measured [21], the size of the effect is small and it is considered negligible in this thesis. Based on Eqs. 1.12 and (1.13), the decay rates of  $B^+$  and  $B^-$  mesons into the possible final states can be seen to satisfy

$$\Gamma(B^- \rightarrow D(\rightarrow f)K^-) \propto 1 + r_D^2 r_B^2 + 2r_B r_D \cos [\delta_B + \delta_D - \gamma], \quad (1.14a)$$

$$\Gamma(B^+ \rightarrow D(\rightarrow \bar{f})K^+) \propto 1 + r_D^2 r_B^2 + 2r_B r_D \cos [\delta_B + \delta_D + \gamma], \quad (1.14b)$$

$$\Gamma(B^- \rightarrow D(\rightarrow \bar{f})K^-) \propto r_D^2 + r_B^2 + 2r_B r_D \cos [\delta_B - \delta_D - \gamma], \quad (1.14c)$$

$$\Gamma(B^+ \rightarrow D(\rightarrow f)K^+) \propto r_D^2 + r_B^2 + 2r_B r_D \cos [\delta_B - \delta_D + \gamma]. \quad (1.14d)$$

The processes in Eqs. (1.14a) and (1.14b) are  $CP$ -conjugate and it is clear how, in the general case where  $\delta_B + \delta_D \neq 0$ , a non-zero value of  $\gamma$  leads to  $CP$  violation in the form of differing decay rates. The same is true for the processes in Eqs. (1.14c) and (1.14d). Depending on the choice of  $D$  final state, these expressions can be used to relate  $\gamma$  to various observables that are experimentally accessible. This thesis concerns the choice  $f = K_S^0 \pi^+ \pi^-$  or  $f = K_S^0 K^+ K^-$ , where the terms related to the  $D$  decay all have a non-trivial variation over the phase space of the decay. However, it is useful to first analyse the simpler case where  $f$  is a two-body state.

The simplest case is when  $f$  is chosen to be a  $CP$  eigenstate, so that  $f = \pm \bar{f}$  and the rate equations of (1.14a)–(1.14d) simplify, because  $r_D = 1$  and  $\delta_D \in \{0, \pi\}$ . Measurements of  $\gamma$  in such decay modes are denoted GLW measurements, after Gronau, London, and Wyler who described the approach in the early 90ies [43, 44]. Experimentally it is preferable to measure yield ratios rather than absolute rates, and the observables of interest are thus the  $CP$  asymmetry

$$\begin{aligned} A_{CP=\pm 1} &= \frac{\Gamma[B^- \rightarrow D_{CP} K^-] - \Gamma[B^+ \rightarrow D_{CP} K^+]}{\Gamma[B^- \rightarrow D_{CP} K^-] + \Gamma[B^+ \rightarrow D_{CP} K^+]} \\ &= \frac{\pm r_B \sin \delta_B \sin \gamma}{1 + r_B^2 \pm 2r_B \cos \delta_B \cos \gamma}, \end{aligned} \quad (1.15a)$$

as well as the ratio

$$\begin{aligned} R_{CP=\pm 1} &= 2 \frac{\Gamma[B^- \rightarrow D_{CP} K^-] + \Gamma[B^+ \rightarrow D_{CP} K^+]}{\Gamma[B^- \rightarrow D^0 K^-] + \Gamma[B^+ \rightarrow \bar{D}^0 K^+]} \\ &= 1 + r_B^2 \pm 2r_B \cos \delta_B \cos \gamma. \end{aligned} \quad (1.15b)$$

In practice,  $A_{CP}$  and  $R_{CP}$  are obtained from measured yield ratios that are corrected with appropriate branching fractions. A measurement of  $A_{CP}$  and  $R_{CP}$  alone is not sufficient to determine the underlying physics parameters  $(\gamma, r_B, \delta_B)$ , and this is not solely due to the number of parameters exceeding the number of constraints:

the equations also allow for multiple, ambiguous solutions for  $(\gamma, \delta_B)$ . One way to break the ambiguity, first noted in the original paper [43], is to make further measurements in additional  $B$  decays. These can be described with the formalism described above, but will not share the same ambiguous solutions because  $(r_B, \delta_B)$  are unique to a given  $B$  decay. Another method is to analyse  $D$  decay final states that are not  $CP$  eigenstates.

A few years later, Atwood, Dunietz, and Sonis analysed an alternative choice of  $D$  final states: a simultaneous analysis of a Cabibbo-favoured (CF) decay  $D^0 \rightarrow f$  and the doubly-Cabibbo-suppressed (DCS) decay  $D^0 \rightarrow \bar{f}$  into the  $CP$  conjugate final state [45, 46]. Their suggested method is named the ADS method after the authors. The classical example is to take  $f = K^-\pi^+$  and  $\bar{f} = \pi^-K^+$ . The relative suppression means that the  $r_D$  of Eq. (1.14) is small, typically of the same order of magnitude as  $r_B$ , and thus the  $CP$  asymmetry of the suppressed decay is  $\mathcal{O}(1)$ :

$$\begin{aligned} A_{ADS(\bar{f})} &= \frac{\Gamma[B^- \rightarrow D(\rightarrow \bar{f})K^-] - \Gamma[B^+ \rightarrow D(\rightarrow f)K^+]}{\Gamma[B^- \rightarrow D(\rightarrow \bar{f})K^-] + \Gamma[B^+ \rightarrow D(\rightarrow f)K^+]} \\ &= \frac{r_D r_B \sin(\delta_B - \delta_D) \sin \gamma}{r_D^2 + r_B^2 + 2r_D r_B \cos(\delta_B - \delta_D) \cos \gamma}. \end{aligned} \quad (1.16a)$$

The large  $CP$  asymmetry is a prime feature of the ADS method. However, also the suppressed-to-favoured yield ratio is sensitive to the physics parameters of interest:

$$\begin{aligned} R_{ADS(\bar{f})} &= \frac{\Gamma[B^- \rightarrow D(\rightarrow \bar{f})K^-] + \Gamma[B^+ \rightarrow D(\rightarrow f)K^+]}{\Gamma[B^- \rightarrow D(\rightarrow f)K^-] + \Gamma[B^+ \rightarrow D(\rightarrow \bar{f})K^+]} \\ &= \frac{r_B^2 + r_D^2 + 2r_D r_B \cos(\delta_B - \delta_D) \cos \gamma}{1 + r_D^2 r_B^2 + 2r_D r_B \cos(\delta_B + \delta_D) \cos \gamma}. \end{aligned} \quad (1.16b)$$

The interpretation of  $A_{ADS}$  and  $R_{ADS}$  in terms of  $(\gamma, r_B, \delta_B)$  requires knowledge of the  $r_D$  and  $\delta_D$  parameters, but these can be measured independently. In general, the constraints from a single set of ADS observables suffer the same ambiguities as in the GLW case. However, unlike the GLW case, each  $D$  decay mode provides an independent set of constraints, because the parameters related to the  $D$  decay vary.

The discussion of this section has centred on the classical case of  $B^\pm \rightarrow DK^\pm$  decays with a two-body  $D$  final state. With minor modifications the techniques have been used to make measurements of  $\gamma$  in  $B^0$  decays [?], with  $B$  decay final states including excited  $D$  mesons [?], excited kaons [?], or pions [?]. The decay  $B^\pm \rightarrow D\pi^\pm$  also is also  $CP$ -violating, although the effect is much smaller than in the  $B^\pm \rightarrow DK^\pm$  decay, because it is expected that  $r_B^{D\pi^\pm} \simeq 0.005$  [47], whereas  $r_B^{DK^\pm} \simeq 0.1$ . Furthermore, it is possible to use multi-body  $D$  final states. However, in some cases, a better precision can then be obtained by exploiting phase-space dependent decay rates. This is the topic of the next section.

### 345 1.3 Measuring $\gamma$ using multi-body D final states

346 In multi-body  $D$  decays, the  $r_D$  and  $\delta_D$  parameters of the fundamental rate equations  
 347 in Eq. (1.14) vary over the phase space of the  $D$  decay. This section describes a  
 348 model-independent approach to measure  $\gamma$  in  $B \rightarrow D(\rightarrow K_S^0\pi^+\pi^-)h^\pm$  decays by  
 349 exploiting this variation. The theory is identical for  $D \rightarrow K_S^0K^+K^-$  decays, and  
 350 similar ideas have been proposed for the  $D \rightarrow K_S^0\pi^+\pi^-\pi^0$  [48] and  $D \rightarrow 2\pi^+2\pi^-$   
 351 modes [49]. First, however, the formalism for describing amplitudes of multi-  
 352 body decays is briefly reviewed.

#### 353 1.3.1 Dalitz plots and the phase space of multi-body decays

354 In general, the phase space of the  $n$ -body decay  $P \rightarrow p_1 + p_2 + \dots + p_n$  consists of  $n$   
 355 four momenta, with a total of  $4n$  components. The requirement that each of the final  
 356 state particles is on-shell provides  $n$  constraints on these components, and energy-  
 357 momentum conservation removes a further 4 degrees of freedom. If the original  
 358 particle  $P$  is a scalar, the decay is isotropic, which removes an additional 3 degrees  
 359 of freedom, leaving the total number of degrees of freedom at  $3n - 7$ . For the specific  
 360 case of three-body decays, the available phase space can thus be parameterised with  
 361 only two parameters. A practical and often used choice is the invariant masses

$$s_{12} = m^2(p_1 p_2) = (p_1^\mu + p_2^\mu)^2, \quad s_{13} = m^2(p_1 p_3) = (p_1^\mu + p_3^\mu)^2. \quad (1.17)$$

362 The choice of particle pairs is arbitrary, and the coordinates easily related

$$m_P^2 + m_{p_1}^2 + m_{p_2}^2 + m_{p_3}^2 = m^2(p_1 p_2) + m^2(p_1 p_3) + m^2(p_2 p_3). \quad (1.18)$$

363 A scatter plot of  $(s_{12}, s_{13})$  values for a sample of particle decays is denoted a Dalitz  
 364 plot [50]. It has the very useful feature that the presence of (narrow) resonances  
 365 in the decay leads to visible bands in the scatter plot. Figure 1.4 illustrates how  
 366 the limits of the Dalitz plot are defined by kinematic constraints, and shows an  
 367 example of a Dalitz plot for  $D \rightarrow K_S^0\pi^+\pi^-$  decays in which the  $K^*(892)^\pm$  and  $\rho(770)$   
 368 resonances are clearly visible. The plot shows the sample of  $B^+ \rightarrow D\pi^+$  decays  
 369 used to make the measurement described in Chapter 4 and thus the  $D$  meson is in  
 370 a superposition of  $D^0$  and  $\bar{D}^0$  states (as detailed in the following section).

371 In terms of the coordinates of Eq. (1.17) the differential decay rate is given by

$$d\Gamma = \frac{1}{32(2\pi)^3 m_P^3} |\mathcal{M}|^2 ds_{12} ds_{13}, \quad (1.19)$$

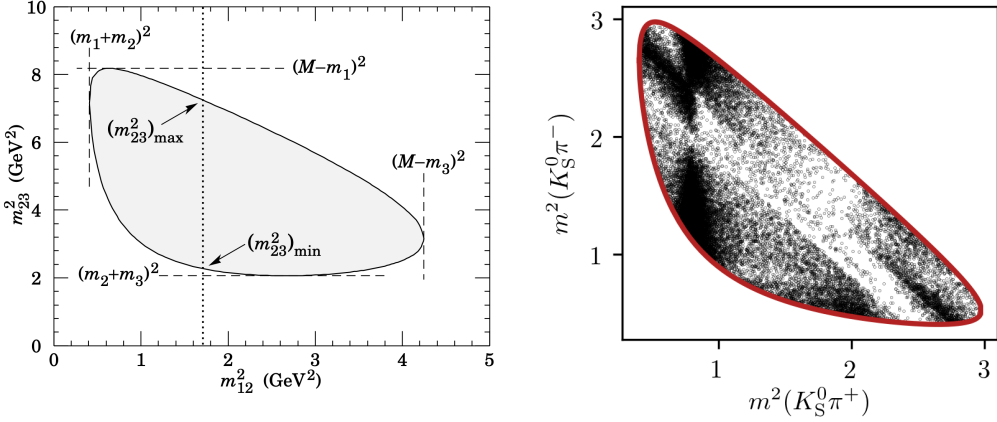


**Figure 1.4:** (Left) Schematic of a Dalitz plot and the limits of the kinematically allowed phase space limits. (Right) Example of a Dalitz plot for  $D \rightarrow K_S^0 \pi^+ \pi^-$  decays where the  $D$  meson originates in a  $B^+ \rightarrow D\pi^+$  decay; the decaying  $D$  meson is in a superposition of the  $D^0$  and  $\bar{D}^0$  states, but predominantly  $\bar{D}^0$ -like.

where  $\mathcal{M}$  is the QFT matrix element, or total decay amplitude, corresponding to the decay. In general, it is not possible to calculate  $\mathcal{M}$  from first principles. Instead, a model is defined with an empirically well motivated form, in which a number of free parameters must be determined experimentally. The simplest case is that of an *isobar* model, where it is assumed that the full decay can be decomposed into consecutive two-body decays of the form  $P \rightarrow R_{12}(\rightarrow p_1 + p_2)p_3$ . Thus,  $\mathcal{M}$  is expressed as a non-resonant constant amplitude term,  $k_{NR}$ , plus a sum of resonance terms

$$\mathcal{M}(s_{12}, s_{13}) = k_{NR} + \sum_r k_r \mathcal{M}^r(s_{12}, s_{13}). \quad (1.20)$$

The exact form of the  $\mathcal{M}^r$  function depends on the resonance in question. An overview is given in the PDG review on resonances and references therein [31]. The isobar formalism breaks down when resonances in the decay are not well separated. In this case, models of the form in Eq. (3.27) can still be employed, if the contribution from overlapping resonances are collected in a single term. An example of such a model, is the amplitude model for  $D^0 \rightarrow K_S^0 \pi^+ \pi^-$  decays developed by the Belle collaboration for a measurement of the CKM angle  $\beta$  in 2018 [51]. In this model, individual terms are included for  $D^0 \rightarrow K^*(\rightarrow K_S^0 \pi^\pm)\pi^\mp$  decays, whereas the  $\pi\pi$  and  $K\pi$   $S$ -wave contributions are modelled with the so-called  $K$ -matrix- and LASS formalisms [52, 53]. The amplitude and phase of  $\mathcal{M}$  as predicted by this model are shown in Fig. 1.5.

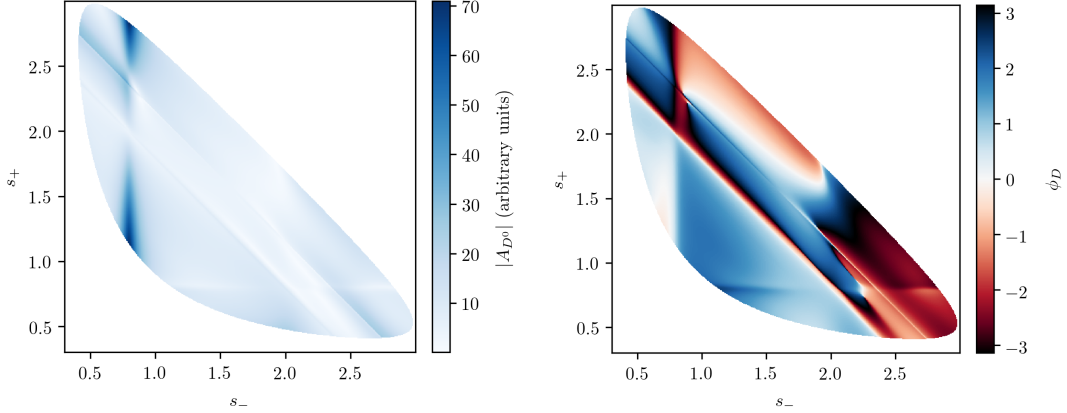


**Figure 1.5:** The (left) magnitude and (right) phase of the  $D \rightarrow K_S^0 \pi^+ \pi^-$  amplitude in the Belle 2018 model [51].

### 1.3.2 The GGSZ method to measure $\gamma$

The non-trivial phase-space dependence of the  $D \rightarrow K_S^0 \pi^+ \pi^-$  decay amplitude can be exploited to measure  $\gamma$  with  $B^\pm \rightarrow DK^\pm$  or  $B^\pm \rightarrow D\pi^\pm$  decays. This approach was proposed independently by Bondar [54], and by Giri, Grossman, Soffer, and Zupan [55] after whom it takes the commonly used acronym GGSZ. For this specific decay  $s_-$  and  $s_+$  are used to describe the Dalitz coordinates  $m^2(K_S^0 \pi^-)$  and  $m^2(K_S^0 \pi^+)$ , respectively, and the  $D$  decay amplitude is a function of these coordinates

$$A_S^{\bar{D}}(s_-, s_+) = A(\bar{D}^0 \rightarrow K_S^0 \pi^+ \pi^-). \quad (1.21)$$

To a good approximation the  $K_S^0$  meson is a  $CP$  eigenstate, meaning that the  $K_S^0 \pi^+ \pi^-$  state is self-conjugate. Assuming this approximation to be exact, and that  $CP$  violation in the  $D$  decay is negligible, the  $D$  decay amplitude satisfies the symmetry relation

$$A_S^{\bar{D}}(s_-, s_+) = A_S^D(s_+, s_-). \quad (1.22)$$

The impact of the  $K_S^0$  meson *not* being an exact  $CP$  eigenstate is treated in detail in Chapter 3. In order to simplify equations, the short-hand notation

$$(s_{-+}) = (s_-, s_+), \quad (s_{+-}) = (s_+, s_-), \quad (1.23)$$

will be employed for the remainder of the thesis, so that the relation in Eq. (1.22) can be expressed as  $A_S^{\bar{D}}(s_{-+}) = A_S^D(s_{+-})$ . Thus, the rate equations of Eq. (1.14)

405 for the  $D \rightarrow K_S^0\pi^+\pi^-$  decay mode are

$$\begin{aligned} d\Gamma^-(s_{-+}) &\propto |\mathcal{A}_S^-|^2 = |A_B|^2 |A_{K_S^0}|^2 \\ &\times [|A_S^D(s_{-+})|^2 + r_B^2 |A_S^D(s_{+-})|^2 + 2r_B |A_S^D(s_{-+})| |A_S^D(s_{+-})| \\ &\times (\cos[\delta_D(s_{-+})] \cos[\delta_B - \gamma] + \sin[\delta_D(s_{-+})] \sin[\delta_B - \gamma])], \end{aligned} \quad (1.24a)$$

$$\begin{aligned} d\Gamma^+(s_{-+}) &\propto |\mathcal{A}_S^+|^2 = |A_B|^2 |A_{K_S^0}|^2 \\ &\times [|A_S^D(s_{+-})|^2 + r_B^2 |A_S^D(s_{-+})|^2 + 2r_B |A_S^D(s_{-+})| |A_S^D(s_{+-})| \\ &\times (\cos[\delta_D(s_{-+})] \cos[\delta_B + \gamma] - \sin[\delta_D(s_{-+})] \sin[\delta_B + \gamma])]. \end{aligned} \quad (1.24b)$$

406 Here,  $\delta_D(s_{-+}) = \phi_D(s_{-+}) - \phi_D(s_{+-}) = -\delta_D(s_{+-})$ , where  $\phi_D(s_{-+})$  denotes the  
 407 complex phase of the  $A_S^D(s_{-+})$  amplitude, and a standard trigonometric relation  
 408 have been employed to factorise the terms depending on the complex phases of the  $B$   
 409 and  $D$  decays. It can be seen that in the case where  $\gamma = 0$  the  $B^+$  and  $B^-$  decay rates  
 410 are symmetric if the Dalitz coordinates are exchanged:  $\Gamma^+(s_-, s_+) = \Gamma^-(s_+, s_-)$ .  
 411 The presence of  $CP$  violation in the  $B$  decay breaks the symmetry. Therefore it is  
 412 possible to measure  $\gamma$  (and the nuisance parameters  $r_B$  and  $\delta_B$ ) from the phase-space  
 413 distribution of  $B^\pm \rightarrow D(\rightarrow K_S^0\pi^+\pi^-)K^\pm$  decays, given knowledge of  $A_S^D(s_{-+})$ .

414 A series of measurements of  $\gamma$  have been made that use amplitude models of the  
 415  $D$  decay [56–63]. However, a model-independent approach has been proposed by  
 416 Bondar and Poluektov [64, 65] that relies on binning phase-space, in which case the  
 417 necessary information on the  $D$  decay amplitude can be summarised in a small set  
 418 of coefficients that can be measured in a separate experiment. That is the approach  
 419 followed in this thesis, and has been used previously by the Belle [66] and LHCb  
 420 collaborations [67]. It is described in detail in the following section.

421 Such a model-independent approach is favourable for two reasons. Firstly,  
 422 uncertainty estimates related to model inputs and the choice of parameterisation in  
 423 an amplitude model are non-trivial, yet would become the leading systematic with  
 424 the very high precision expected for  $\gamma$  measurements in the near future. Secondly,  
 425 amplitude models are notoriously hard to reproduce, and in a high-precision era it  
 426 is favourable that any experiment is easy to reinterpret in various extensions of the  
 427 SM. This is a lot easier for an experiment that measures a small set of well-defined  
 428 observables, than for an experiment that fits a complicated amplitude model.

429 An alternative model-independent approach has recently been proposed by  
 430 Poluektov [68] where the externally measured input on the  $D$ -decay phase are  
 431 Fourier expansion coefficients, and which therefore avoids binning phase space; this  
 432 approach may have the potential to improve the obtainable precision in the future.

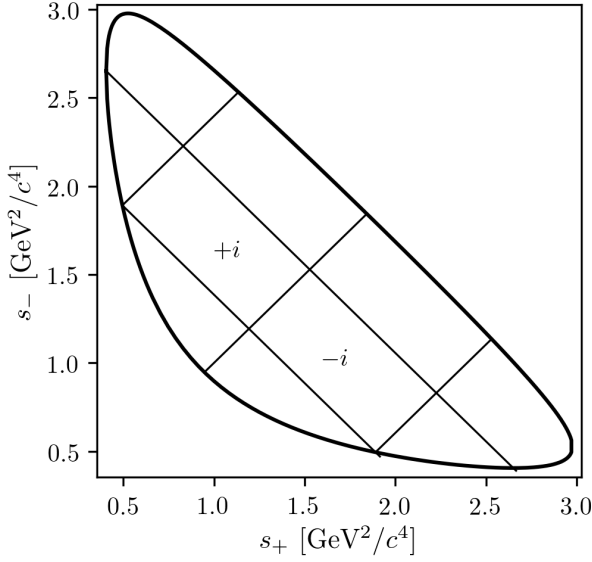


**Figure 1.6:** Illustration of the binning scheme used in GGSZ measurements: the bins are symmetric around the  $m^2(K_S^0\pi^+) = m^2(K_S^0\pi^-)$  diagonal, and numbered so that opposite bins have the same number, but with opposite sign.

### 1.3.3 A model-independent approach

The phase-space distribution can be analysed in a model-independent way, if the  $D$ -decay phase space is split into regions, or bins, and the  $B$  decay yield in each bin determined experimentally. A measurement of  $\gamma$  using this approach is the main topic of the thesis. This section describes the fundamental principle, whereas the details pertaining to the exact experimental approach are delegated to Section 1.4.

The amplitude symmetry of Eq. (1.22) is exploited by defining  $2N$  bins to be symmetric around the  $s_- = s_+$  diagonal of the Dalitz plot, numbered  $i = -N$  to  $N$  (omitting zero) such that if the point  $(s_-, s_+)$  is in bin  $i$ , then  $(s_+, s_-)$  is in bin  $-i$ , and by convention  $i > 0$  for bins where  $s_- > s_+$ . The principle is illustrated in Fig. 1.6, but the binning schemes used in actual measurements are more complicated. The decay rates in Eq. (1.24) can be integrated over such bins, and give the bin yields

$$\begin{aligned} N_i^- &\propto h^- \left[ K_i + r_B^2 K_{-i} + 2\sqrt{K_i K_{-i}} (c_i x_- + s_i y_-) \right], \\ N_i^+ &\propto h^+ \left[ K_{-i} + r_B^2 K_i + 2\sqrt{K_i K_{-i}} (c_i x_+ - s_i y_+) \right], \end{aligned} \quad (1.25)$$

where the parameters describing the  $B$  decay have been expressed in terms of the observables

$$x_\pm = r_B \cos(\delta_B \pm \gamma), \quad y_\pm = r_B \sin(\delta_B \pm \gamma), \quad (1.26)$$

448 and a number of phase-space integrated quantities related to the  $D$ -decay have  
449 been introduced. The  $K_i$  parameters denote fractional yield of a flavour-tagged  
450  $D^0$  decaying into bin  $i$ , defined as

$$K_i = \frac{1}{N_K} \int_i ds^2 |A_S^D(s_{-+})|^2, \quad N_K = \int ds^2 |A_S^D(s_{-+})|^2, \quad (1.27)$$

451 where  $\int_i ds^2$  denotes integration over bin  $i$  of the Dalitz plot. The  $c_i$  and  $s_i$  denote  
452 the amplitude-weighted average of  $\cos \delta_D(s_{-+})$  and  $\sin \delta_D(s_{-+})$  over bin  $i$

$$\begin{aligned} c_i &= \frac{\int_i ds^2 |A_S^D(s_{-+})| |A_S^D(s_{-+})| \cos[\delta_D(s_{-+})]}{\sqrt{\int_i ds^2 |A_S^D(s_{-+})|^2} \sqrt{\int_i ds^2 |A_S^D(s_{-+})|^2}}, \\ s_i &= \frac{\int_i ds^2 |A_S^D(s_{-+})| |A_S^D(s_{-+})| \sin[\delta_D(s_{-+})]}{\sqrt{\int_i ds^2 |A_S^D(s_{-+})|^2} \sqrt{\int_i ds^2 |A_S^D(s_{-+})|^2}}. \end{aligned} \quad (1.28)$$

453 By the symmetry properties of  $\delta_D(s_{-+})$  these parameters satisfy  $c_i = c_{-i}$  and  
454  $s_i = -s_{-i}$ . The normalisation constants  $h^+$  and  $h^-$  are identical in the ideal case,  
455 but it is convenient to define them separately for practical reasons: depending on  
456 the experimental setup, there may be overall production and detection asymmetries  
457 that affect the total signal yields. An experimental analysis can be made insensitive  
458 to these effects because they can be absorbed into the normalisation constants, as  
459 long as they are constant over the  $D$ -decay phase space. This comes at the cost  
460 that the information on  $x_\pm$  and  $y_\pm$  from the overall  $CP$  asymmetry is lost, but  
461 Section 1.3.5 will show the loss in precision to be minimal.

462 Thus, for a set of  $2N$  bins, the bin yields of Eqs. (1.25) provide  $4N$  constraints  
463 on a total of  $4N + 6$  parameters:  $(h^\pm, K_i, c_i, s_i, x_\pm, y_\pm)$ . However, the  $K_i$ ,  $c_i$ , and  
464  $s_i$  parameters relate only to the  $D$  decay, and can thus, in principle, be measured  
465 in independent experiments. With such external inputs, a measurement of the  
466  $B^\pm \rightarrow D(\rightarrow K_S^0 \pi^+ \pi^-) K^\pm$  yields in a set of bins can be used to constrain  $x_\pm$  and  $y_\pm$ ,  
467 and thereby  $(\gamma, r_B, \delta_B)$ . The measurement presented in this thesis determines the  
468  $K_i$  parameters directly, but uses externally measured values of  $c_i$  and  $s_i$  as input,  
469 as measured in quantum correlated  $D$  decays by the CLEO [69] and BESIII [70]  
470 collaborations. Because these measurements are the foundation of the approach,  
471 they are described in some detail in the following section. In the future, it is possible  
472 that the  $c_i$  and  $s_i$  parameters may be measured in quantum-correlated  $D$  decays  
473 in LHCb [71], and in charm-mixing measurements [72].

### 1.3.4 Measuring strong-phase inputs at charm factories

The strong-phase parameters  $c_i$  and  $s_i$  have been measured by the CLEO and BESIII collaborations, using quantum correlated  $D^0\bar{D}^0$  pairs from decays of the  $\psi(3770)$  resonance state, itself produced in  $e^+e^-$  collisions at the resonance energy. The  $\psi(3770)$  has quantum-number  $C = -1$ , which is conserved in the strong decay into two  $D$  mesons, and thus the two  $D$  mesons are produced in an anti-symmetric wave function. By observing the decay of one  $D$  meson into a specific final state, say a  $CP$  eigenstate, the quantum state of the other  $D$  meson can be determined. The measurement is based on decays where both  $D$  decays are reconstructed, one in the  $K_S^0\pi^+\pi^-$  final state, the other in one of several different tag categories. The main principles are outlined below, but most experimental considerations and implementation details are left out for the sake of brevity.

The simplest case is when one  $D$  meson decays into a final state that uniquely tags the flavour, such as  $\bar{D}^0 \rightarrow K^+e^-\bar{\nu}_e$ . In that case, the  $D$  meson decaying to  $K_S^0\pi^+\pi^-$  is known to be in the  $D^0$  state and the decay rate is simply determined by  $A_S^D : \Gamma(s_{-+}) \propto |A_S^D(s_{-+})|^2$ . This allows for a measurement of the  $K_i$  parameters.

If one  $D$  meson is reconstructed in a  $CP$ -even state, eg.  $K^+K^-$ , or a  $CP$ -odd state, eg.  $K_S^0\pi^0$ , the  $D$  meson decaying to  $K_S^0\pi^+\pi^-$  is known to be in a state of opposite  $CP$ . Thus, for a tag-decay of  $CP = \pm 1$  the decay rate has the form

$$\Gamma_{CP=\pm 1} \propto |A_S^D(s_{-+}) \mp A_S^D(s_{+-})|^2 \quad (1.29a)$$

and the bin yields will be given by

$$M_i^\pm \propto K_i + K_{-i} \mp 2\sqrt{K_i K_{-i}} c_i. \quad (1.29b)$$

Thus a simultaneous analysis of flavour and  $CP$  tagged decays allow for a determination of the  $K_i$  and  $c_i$  parameter sets.

Finally, the case where both  $D$  mesons, for now denoted  $D$  and  $D'$ , decay into the  $K_S^0\pi\pi$  final state can be considered. The total amplitudes have contributions from the case where  $D$  is in the  $D^0$  state and  $D'$  is in the  $\bar{D}^0$  state, as well as the opposite flavour assignment. Thus the decay rate satisfies

$$\Gamma_{CP=\pm 1} \propto |A_S^D(s_{-+})A_S^D(s'_{+-}) + A_S^D(s_{+-})A_S^D(s'_{-+})|^2 \quad (1.30a)$$

where  $s_{-+}$  denotes the Dalitz-plot coordinates of the  $D$  meson, and  $s'_{-+}$  those of the  $D'$  meson. Defining  $M_{ij}$  to be the yield of decays where the  $D$  decay is in bin  $i$  and the  $D'$  in bin  $j$ , the bin yields satisfy

$$M_{ij} \propto K_i K_{-j} + K_j K_{-i} - 2\sqrt{K_i K_{-i} K_j K_{-j}} (c_i c_j + s_i s_j). \quad (1.30b)$$

503 Thus, analysing these decays in addition to the  $CP$  and flavour tagged decays provide  
 504 information on all of  $K_i$ ,  $c_i$ , and  $s_i$ . Note, however, that Eqs. (1.29) and (1.30) are  
 505 invariant under the transformation  $\delta_D \rightarrow -\delta_D$ . In practice, the analysis is extended  
 506 in a number of ways to enhance the statistics: using "flavour-tag" states that are not  
 507 exact flavour tags, such as  $K^-\pi^+$ , using self-conjugate multi-body  $D$ -decay final  
 508 states that are not exact  $CP$  eigenstates, such as  $\pi^+\pi^-\pi^0$ , and using the  $K_L^0\pi^+\pi^-$   
 509 final state as well. However, the main principles are the same as described above.

510 The measurements of  $c_i$  and  $s_i$  are made for a range of different binning schemes.  
 511 It was noted already in Ref. [65] that a rectangular binning scheme, such as the  
 512 example in Fig. 1.6, does not provide the optimal sensitivity to  $\gamma$ . A better sensitivity  
 513 can be obtained if the bins are defined such that  $\delta_D$  is approximately constant over  
 514 a given bin, by defining bin  $i$  out of  $N$  via the condition

$$\text{bin}_i = \{(s_-, s_+) \mid 2\pi(i - 3/2)/N < \delta_D(s_-, s_+) < 2\pi \times (i - 1/2)/N\}. \quad (1.31)$$

515 In practice, the binning scheme is defined by splitting the  $D$ -decay phase-space  
 516 into quadratic *micro bins* with a width of  $0.0054 \text{ (GeV}/c^2)^2$  and assigning a bin  
 517 number to each micro bin via the condition in (1.31) as evaluated in an amplitude  
 518 model of choice. The obtained binning scheme when using an amplitude model  
 519 developed by the BaBar collaboration in 2008 [57] is shown in Fig. 1.7a. In Ref [65]  
 520 it was also shown that the binning can be even further optimised for sensitivity.  
 521 The suggested figure of merit is

$$Q^2 = \frac{\sum_i \left( \frac{1}{\sqrt{N_i^B}} \frac{dN_i^B}{dx} \right)^2 + \left( \frac{1}{\sqrt{N_i^B}} \frac{dN_i^B}{dy} \right)^2}{\int ds^2 \left[ \left( \frac{1}{|\Gamma^B(s_-)|} \frac{d|\Gamma^B(s_-)|^2}{dx} \right)^2 + \left( \frac{1}{|\Gamma^B(s_-)|} \frac{d|\Gamma^B(s_-)|^2}{dy} \right)^2 \right]} \quad (1.32)$$

522 which quantifies the statistical sensitivity for a given binning, relative to the one  
 523 achievable in an unbinned analysis. The CLEO collaboration defined an *optimal*  
 524 binning scheme by an iterative procedure where, starting from the equal binning  
 525 scheme, a micro-bin is randomly reassigned new bin numbers in each step, and a  
 526 step accepted if  $Q^2$  increases. The optimisation is done for the case where  $x = y = 0$   
 527 and thus  $Q^2$  simplifies to  $Q_{x=y=0}^2 = \sum_i N_i^{x=y=0} (c_i^2 + s_i^2) / N_{total}^{x=y=0}$ . The resulting  
 528 binning scheme is shown in Fig. 1.7b. An additional binning scheme is defined,  
 529 denoted the *modified optimal* scheme and shown in Fig. 1.7c, where the  $Q^2$  figure  
 530 of merit is modified to take into account the presence of backgrounds [69]. The  
 531 modified optimal binning scheme has proven beneficial to use in measurements with  
 532 small signal yields [], but is not employed in the present thesis.

Where exactly is this phase sign known from?  
Is the overall sign not arbitrary in amplitude models?

**Table 1.1:** The experimentally measured  $c_i$  and  $s_i$  values used in the thesis. The  $D \rightarrow K_S^0\pi^+\pi^-$  values are the combined values from the BESIII and CLEO measurements published by BESIII [70]. The  $D \rightarrow K_S^0K^+K^-$  values are measured by CLEO [69].

Optimal binning scheme: $D \rightarrow K_S^0\pi^+\pi^-$		
Bin $i$	$c_i$	$s_i$
1	$-0.037 \pm 0.049$	$0.829 \pm 0.097$
2	$0.837 \pm 0.067$	$0.286 \pm 0.152$
3	$0.147 \pm 0.066$	$0.786 \pm 0.154$
4	$-0.905 \pm 0.021$	$0.079 \pm 0.059$
5	$-0.291 \pm 0.041$	$-1.022 \pm 0.062$
6	$0.272 \pm 0.082$	$-0.977 \pm 0.176$
7	$0.918 \pm 0.017$	$-0.184 \pm 0.065$
8	$0.773 \pm 0.033$	$0.277 \pm 0.118$

2-bins binning scheme: $D \rightarrow K_S^0K^+K^-$		
Bin $i$	$c_i$	$s_i$
1	$0.818 \pm 0.107$	$-0.445 \pm 0.215$
2	$-0.746 \pm 0.083$	$-0.229 \pm 0.220$

Both the CLEO and BESIII collaborations have measured the values of  $c_i$  and  $s_i$  for the equal, optimal, and modified optimal binning schemes. The results are also shown in Fig. 1.7, where they are compared to the expectation from the latest amplitude model [51]. The measurements presented in this thesis are based on a combination of the BESIII and CLEO results for the optimal binning scheme, made by the BESIII collaboration [70] and tabulated in Table 1.1.

While the *definition* and *optimisation* of these binning schemes depend on knowledge of  $A_S^D(s_-, s_+)$  via an amplitude model, it is important to note that no model information is needed when the binning schemes are used in the subsequent measurements of strong-phases<sup>5</sup> or  $CP$ -observables. Therefore the measurements will not be biased by any modelling imperfections, although the obtained precision might be lower than expected.

The preceding discussion has been focusing on the  $D \rightarrow K_S^0\pi^+\pi^-$  channel, however the  $D \rightarrow K_S^0K^+K^-$  channel can be analysed completely analogously. The CLEO collaboration measure  $c_i$  and  $s_i$  values for this mode as well, in three binning schemes [69]. These are all equal-phase binning schemes, with 2, 3, and 4 bins,

<sup>5</sup>With the exception of minimal model-dependence introduced when the  $K_L^0\pi^+\pi^-$  final state is employed to constrain the  $s_i$  parameters by the  $D$ -factories [69, 70], the impact of which is well under control.

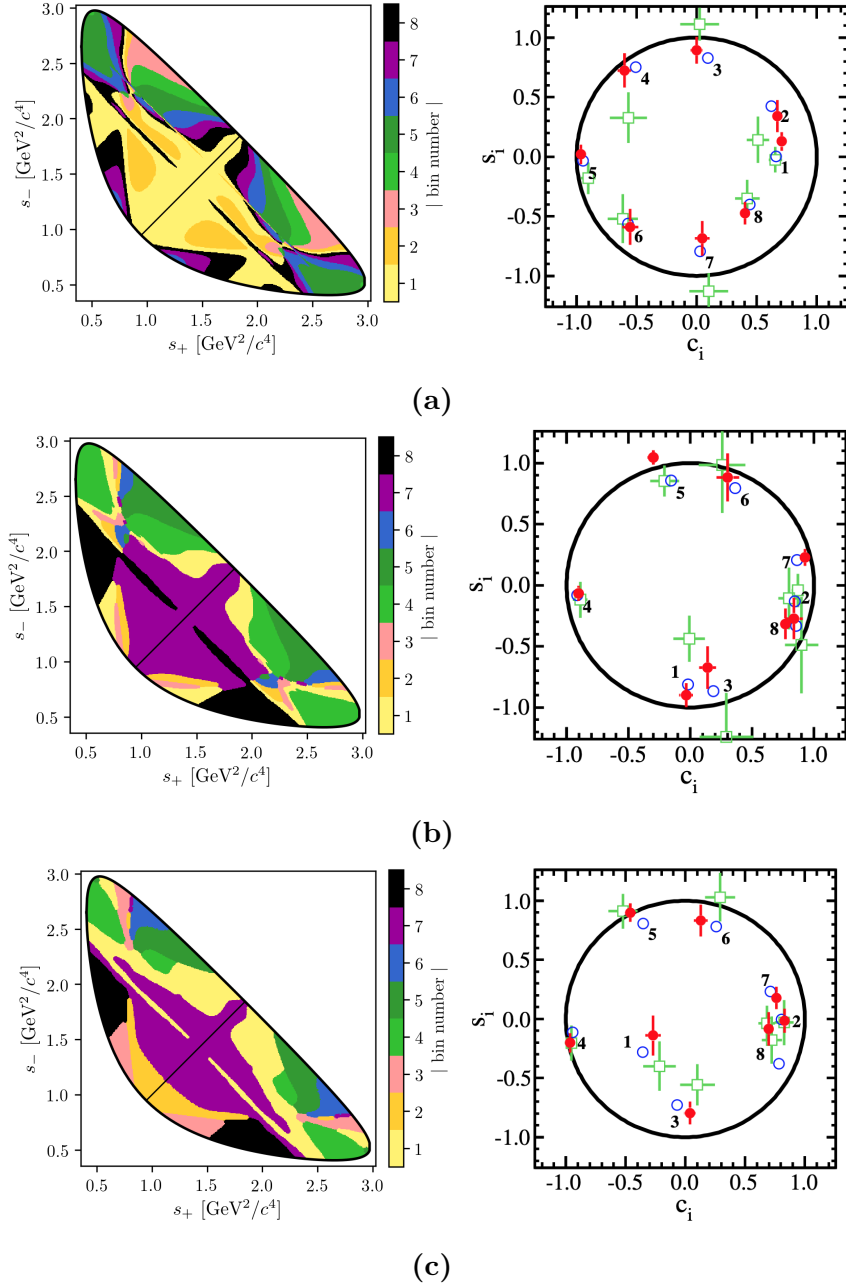


**Figure 1.7:** The (left) binning schemes and (right) measured values of  $(c_i, s_i)$  for (a) equal, (b) optimal, and (c) modified optimal binning schemes for  $D \rightarrow K_S^0 \pi^+ \pi^-$ . The plots of the measured values are taken from Ref. [70] and show the results obtained by (red) BESIII, (green) CLEO, and (blue) the model expectation using the model from Ref. [51]. The measurement featured in this thesis used the optimal binning scheme.

respectively, shown in Fig. 1.8. The  $D \rightarrow K_S^0 K^+ K^-$  decay amplitude is almost completely dominated by two  $K^+ K^-$  resonances, the  $CP$ -odd  $\phi(1020)$  and the  $CP$ -even  $a_0(980)$ , and this means that very little gain in sensitivity can be made by altering the equal-phase binning schemes. The measured  $c_i$  and  $s_i$  values are also shown in Fig. 1.8 and tabulated in Table 1.1 for the 2-bins scheme, which is used in this thesis. A BESIII measurement is in preparation, but has not been finished at the time of writing.

### 1.3.5 Global CP asymmetry and the relation to GLW and ADS measurements

The introduction of separate normalisation factors  $h^+$  and  $h^-$  in Eq. (1.25) hides the fact that information on  $\gamma$  (in principle) can be obtained from the asymmetry in phase-space-integrated  $B^+$  and  $B^-$  yields. In the ideal case where  $h^- = h^+$  the total yield asymmetry is

$$\begin{aligned} A_{GGSZ} &= \frac{\sum_i N_- - N_i^+}{\sum_{i=-N}^N N_i - +N_i^+} = \frac{\sum_{i=-N}^N \sqrt{K_i K_{-i}} c_i (x_- - x_+)}{1 + r_B^2 + 2 \sum_{i=-N}^N \sqrt{K_i K_{-i}} c_i (x_- + x_+)} \\ &= \frac{2 \sum_{i=1}^N \sqrt{K_i K_{-i}} c_i (x_- - x_+)}{1 + r_B^2 + 4 \sum_{i=1}^N \sqrt{K_i K_{-i}} c_i (x_- + x_+)}, \end{aligned} \quad (1.33)$$

where it has been exploited that  $\sum_{i=-N}^N \sqrt{K_i K_{-i}} s_i = 0$  by definition. The size of the asymmetry is governed by the factor  $\sum_{i=1}^N \sqrt{K_i K_{-i}} c_i$ , which is small for  $D \rightarrow K_S^0 \pi^+ \pi^-$  and  $D \rightarrow K_S^0 K^+ K^-$  decays. The underlying reason is that  $\delta_D(s_-, s_+)$  varies significantly across phase-space for these decays, as evident by the spread in the values of  $c_i$  in Table 1.1, which reduces the *average* of the asymmetry-generating  $D^0 - \bar{D}^0$  interference term to being close to zero. The value of  $\sum_{i=-N}^N \sqrt{K_i K_{-i}} c_i$  is closely related to the  $CP$  content of the final state in question: for a self-conjugate  $CP$  even (odd) final state

$$A_{D^0}(s_-, s_+) = {}^{(+)}_{(-)} A_{\bar{D}^0}(s_-, s_+) = {}^{(+)}_{(-)} A_{D^0}(s_+, s_-) \quad (1.34)$$

and thus  $\sum_{i=1}^N \sqrt{K_i K_{-i}} c_i = {}^{(+)}_{(-)} 1$ . This motivates the definition of the  $CP$ -even fraction of the decay

$$\mathcal{F}_+ \equiv \frac{1}{2} \left( 1 + \sum_{i=1}^N \sqrt{K_i K_{-i}} c_i \right). \quad (1.35)$$

With  $\mathcal{F}_+$  in hand, the asymmetry in Eq. (1.33) can be rewritten

$$A_{GGSZ} = \frac{(2\mathcal{F}_+ - 1)r_B \sin \delta_B \sin \gamma}{1 + r_B^2(2\mathcal{F}_+ - 1)2r_B \cos \delta_B \cos \gamma}, \quad (1.36)$$

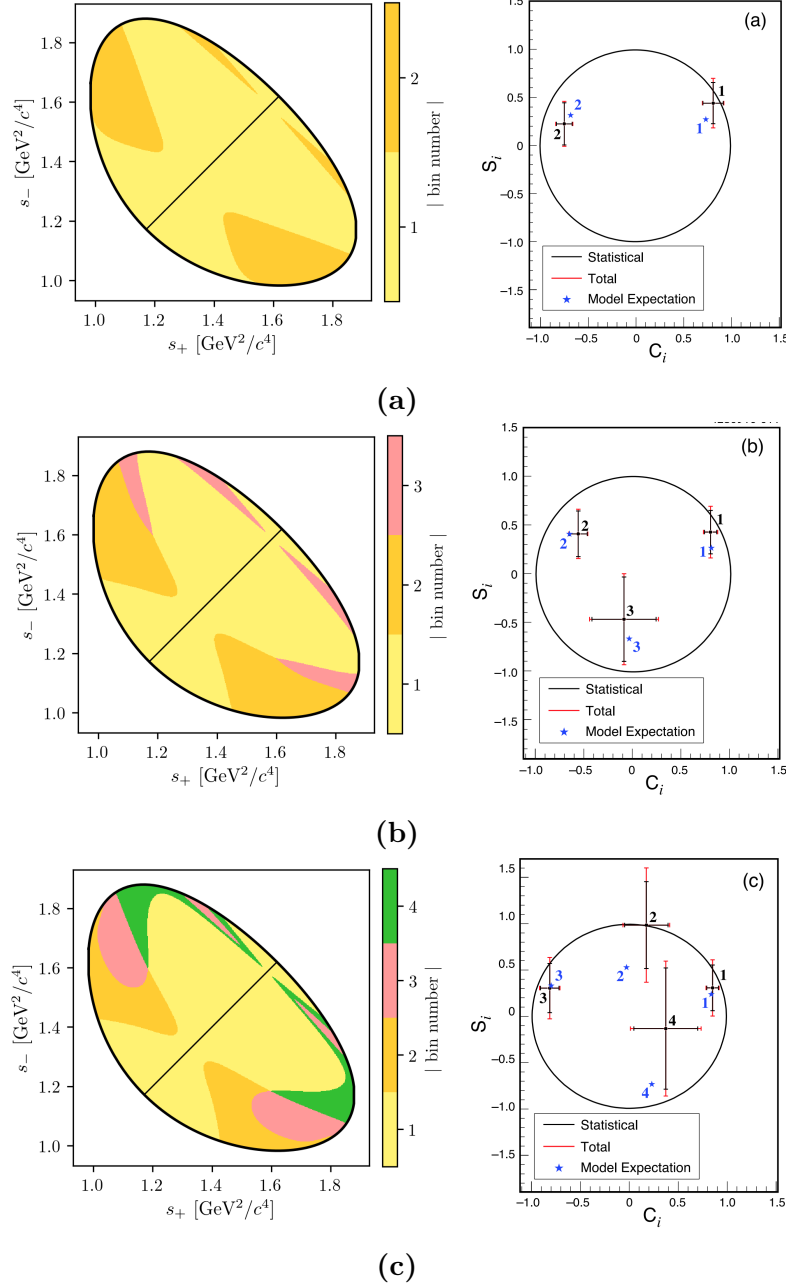


**Figure 1.8:** The (left) binning schemes and (right) measured values of  $(c_i, s_i)$  for the (a) 2-, (b) 3-, and (c) 4-bins binning schemes for  $D \rightarrow K_S^0 K^+ K^-$ . The plots of the measured values are taken from Ref. [69] and show the (error bars) results obtained by CLEO, and (blue) the model expectation using the model from Ref. [58]. The measurement featured in this thesis uses the 2-bins scheme.

which is the usual form used in quasi-GLW measurements []; for  $N = 1$  the definition in Eq. (1.35) is equivalent to  $\mathcal{F}_+$  as defined in Ref. []. The value of  $\mathcal{F}_+$  is independent of the number and shape of bins in a given binning scheme, as long as the bin definitions follow the symmetry principles outlined in Section 1.3.3. For  $D \rightarrow K_S^0\pi^+\pi^-$  and  $D \rightarrow K_S^0K^+K^-$  decays the values of  $\mathcal{F}_+$  are

$$\begin{aligned}\mathcal{F}_+(K_S^0\pi^+\pi^-) &= X? \\ \mathcal{F}_+(K_S^0K^+K^-) &= X?\end{aligned}\tag{1.37}$$

as evaluated with the Belle 2018 model for  $D \rightarrow K_S^0\pi^+\pi^-$  decays and the BaBar 2010 model for  $D \rightarrow K_S^0K^+K^-$  decays. Since  $r_B^{DK^\pm} \sim 0.1$  the predicted global asymmetries are thus approximately 1–2 %, which is not resolvable with the current experimental yields. As shown in Chapter 3,  $CP$  violation in the  $K_S^0$  sector leads to asymmetries of a similar size, further complicating the use of global asymmetries to constrain  $x_\pm$  and  $y_\pm$ . Thus these modes are ill-suited for quasi-GLW measurements, and ignoring global asymmetries leads to a negligible loss of information on  $\gamma$  in a GGSZ measurement. The reverse is true for a well-suited quasi-GLW mode, such as  $D \rightarrow \pi^+\pi^-\pi^0$ : if  $\mathcal{F}_+$  is close to either zero or unity, it means that  $(c_i, s_i)$  will be close to  $(\pm 1, 0)$  in all bins for *any* given binning scheme, and the set of bins will provide almost identical constraints on  $x_\pm$  and  $y_\pm$ . Thus, the binning of phase space leads to no significant gain in precision compared to a global analysis.

Indeed, a crucial quality of the GGSZ method, is that exactly because each bin-pair provides independent constraints on  $x_\pm$  and  $y_\pm$ , the method provides a single solution for  $(\gamma, r_B, \delta_B)$  that does not suffer the ambiguities of the ADS and GLW approaches. In order to illustrate this further, it is useful to make one more comparison of the model-independent GGSZ formalism to the ADS and GLW formalisms. If there was no  $CP$  symmetry the  $B^+$  yield in bin  $+i$  would equal the  $B^-$  yield in bin  $-i$ . Therefore the relevant  $CP$  asymmetry for a given Dalitz bin is

$$\begin{aligned}A_{GGSZ}^i &\equiv \frac{N_i^- - N_{-i}^+}{N_i^- + N_{-i}^+} \\ &= \frac{\sqrt{K_i K_{-i}}(c_i(x_- - x_+) + s_i(y_- - y_+))}{K_i + r_B^2 K_{-i} + 2\sqrt{K_i K_{-i}}(c_i(x_- + x_+) + s_i(y_- + y_+)})\end{aligned}\tag{1.38}$$

This expression is identical to the ADS asymmetry in Eq. (1.16a) if the effective  $D$ -decay parameters  $r_D^i$  and  $\delta_D^i$  are defined via

$$\kappa_i \cos \delta_D^i \equiv c_i \quad , \quad \kappa_i \sin \delta_D^i \equiv s_i \quad , \quad r_D^i \equiv \sqrt{K_i/K_{-i}},\tag{1.39}$$

and a coherence factor,  $\kappa$ , is included in the interference terms of the ADS expression, as is standard for multi-body  $D$  decays []. These parameters allow us to classify

**Table 1.2:** Classification of the bins used in model-independent GGSZ measurements, in terms of whether the interplay between the  $D^0$  and  $\bar{D}^0$  amplitudes in the bin resemble typical GLW or ADS behaviour. The parameters are calculated using the 2018 Belle model [1] for  $D \rightarrow K_S^0\pi^+\pi^-$  decays and the 2010 BaBar model [2] for  $D \rightarrow K_S^0K^+K^-$  decays.

Optimal binning scheme: $D \rightarrow K_S^0\pi^+\pi^-$					
Bin $i$	$\hat{r}_D$	$\hat{\delta}_D$	$\mathcal{F}_+$	$\kappa$	Bin type
1	0.473	91.9°	48.97 %	0.81	Mixed
2	0.164	11.1°	63.38 %	0.85	ADS-like
3	0.157	79.4°	52.50 %	0.89	ADS-like
4	0.768	175.3°	5.85 %	0.92	GLW-odd-like
5	0.759	-99.9°	42.84 %	0.87	Mixed
6	0.223	-64.5°	57.92 %	0.87	ADS-like
7	0.651	-13.3°	89.44 %	0.89	GLW-even-like
8	1.745	21.0°	87.08 %	0.92	GLW-even-like

2-bins binning scheme: $D \rightarrow K_S^0K^+K^-$					
Bin $i$	$\hat{r}_D$	$\hat{\delta}_D$	$\mathcal{F}_+$	$\kappa$	Bin type
1	0.816	19.8°	86.14 %	0.78	GLW-even-like
2	0.775	154.5°	16.23 %	0.77	GLW-odd-like

601 a given pair of bins with number  $\pm i$  as either *GLW-like*, if  $\delta_D^i$  is close to 0 or  $\pi$   
 602 and  $r_D^i$  is close to unity, or *ADS-like* if  $0 < r_D^i \ll 1$ . The  $CP$ -even fraction of the  
 603  $D$ -decay can also be defined for a given bin-pair:

$$\mathcal{F}_+^i = \mathcal{F}_+^{-i} \equiv \frac{1}{2} \left( 1 + 2c_i \frac{\sqrt{K_i K_{-i}}}{K_i + K_{-i}} \right) = \frac{1}{2} \left( 1 + 2c_i \frac{r_D^i}{1 + r_D^{i/2}} \right). \quad (1.40)$$

604 A GLW-even-like bin pair will have  $\mathcal{F}_+^i \simeq 1$  and a GLW-odd-like bin pair will  
 605 have  $\mathcal{F}_+^i \simeq 0$ .

606 Table 1.2 summarises a classification of the bins for the optimal  $D \rightarrow K_S^0\pi^+\pi^-$   
 607 binning scheme and the 2-bins  $D \rightarrow K_S^0K^+K^-$  binning scheme following these  
 608 principles. Two bins are classified as *mixed* because  $r_D^i$  is not particularly small,  
 609 but  $\mathcal{F}_+^i$  is close to 0.5. The fact that multiple bin types appear for both the  
 610  $D \rightarrow K_S^0\pi^+\pi^-$  and  $D \rightarrow K_S^0K^+K^-$  modes underline that each mode benefits from  
 611 being analysed in the GGSZ formalism, and that the bins provide independent  
 612 constraints, allowing for a non-ambiguous solution for  $(\gamma, r_B, \delta_B)$ .

## 1.4 Strategy for the LHCb measurement

The main topic of the thesis is a model-independent GGSZ measurement using  $B^\pm \rightarrow DK^\pm$  and  $B^\pm \rightarrow D\pi^\pm$  decays, and the two  $D$  final states  $K_S^0\pi^+\pi^-$  and  $K_S^0K^+K^-$ . The measurement uses the optimal binning scheme for the  $D \rightarrow K_S^0\pi^+\pi^-$  mode, with the combined strong-phase inputs from the BESIII [70] and CLEO [69] collaborations published in Ref. [70]. For the  $D \rightarrow K_S^0K^+K^-$  channel, the 2-bins scheme is used with the strong-phase parameters measured by the CLEO collaboration [69]. The details of the analysis are presented in Chapter (4), but the overall strategy and a few extensions of the formalism from the previous sections are given here.

Due to the geometry of the LHCb detector, the signal reconstruction efficiency for  $B^\pm \rightarrow D(\rightarrow K_S^0h^+h^-)h'^\pm$  decays varies significantly across the  $D$ -decay phase space. Denoting the efficiency profile as  $\eta(s_-, s_+)$ , the yield equations of Eq. (1.25) are therefore modified slightly

$$\begin{aligned} N_i^- &= h^{B^-} \left[ F_i + r_B^2 F_{-i} + 2\sqrt{F_i F_{-i}} (c'_i x_- + s'_i y_-) \right], \\ N_i^+ &= h^{B^+} \left[ F_{-i} + r_B^2 F_i + 2\sqrt{F_i F_{-i}} (c'_i x_+ - s'_i y_+) \right], \end{aligned} \quad (1.41)$$

where the phase-space integrated quantities now include the efficiency profile

$$F_i = \frac{1}{N_F} \int ds^2 \eta(s_-) |A_S^D(s_-)|^2, \quad N_F = \int ds^2 \eta(s_-) |A_S^D(s_-)|^2, \quad (1.42)$$

$$c'_i = \frac{\int_i ds^2 \eta(s_-) |A_S^D(s_-)| |A_S^D(s_-)| \cos[\delta_D(s_-)]}{\sqrt{\int_i ds^2 \eta(s_-) |A_S^D(s_-)|^2} \sqrt{\int_i ds^2 \eta(s_-) |A_S^D(s_-)|^2}}, \quad (1.43)$$

with an analogous definition of  $s'_i$ . At leading order, the strong-phase parameters are unaffected by the non-uniform efficiency, and, in addition, the bin definitions favour bins for which  $c_i$  and  $s_i$  take on similar values across each bin. Therefore, the  $c_i$  and  $s_i$  values reported by the charm factories are used directly in the measurement. The impact on the obtained central values is negligible, as described in detail in Section 4.5 where a systematic uncertainty is assigned.

The  $F_i$  are significantly different to the  $K_i$  due to the experimental acceptance profile in LHCb. Given external inputs for the strong-phase parameters, it is possible to fit the  $F_i$  parameters and  $x_\pm$  and  $y_\pm$  simultaneously in a fit to the LHCb  $B^\pm \rightarrow DK^\pm$  data set, in which case the obtained  $F_i$  parameters incorporate the correct acceptance profile correction by construction. However, the obtainable precision for the  $CP$  observables measured by this procedure is suboptimal. As

an alternative, the first LHCb measurement [67] made a simultaneous analysis of  $B^\pm \rightarrow DK^\pm$  and a much larger sample of  $B^\pm \rightarrow D\pi^\pm$  decays; since the  $F_i$  parameters relate to the  $D$  decay, they can effectively be obtained in the  $D\pi^\pm$  sample and shared between the two  $B^\pm \rightarrow Dh^\pm$  channels. However, there is  $CP$  violation present in the  $B^\pm \rightarrow D\pi^\pm$  decays, which led to a dominant systematic uncertainty. Later LHCb measurements [3, 73] instead relied on flavour tagged  $D$  mesons from  $\bar{B}^0 \rightarrow D^{*+}(\rightarrow D^0\pi^+)\mu^-\bar{\nu}_\mu X$  decays to obtain  $F_i$ , where no  $CP$  violation is possible. However, due to necessarily different triggering paths and selections, the acceptance profile is not exactly identical between semi-leptonic decays and the  $B^\pm \rightarrow Dh^\pm$  decays of interest. An efficiency correction based on simulation was therefore applied to obtain the correct  $F_i$ , and in this case, the uncertainty related to the correction constituted the largest systematic uncertainty on the measurement.

Both sources of systematic uncertainty can be avoided by making a simultaneous analysis of  $B^\pm \rightarrow DK^\pm$  and  $B^\pm \rightarrow D\pi^\pm$  decays, where  $CP$ -violating observables are measured in *both* channels and the  $F_i$  parameters are shared. Effectively, the  $F_i$  are determined in the high statistics  $B^\pm \rightarrow D\pi^\pm$  channel, but with no systematic effect from  $CP$ -violation in that channel, since the  $CP$ -violation is incorporated in the yield description. At the start of the work that lead to this thesis, it was not clear to what degree the measured  $CP$ -violating observables in  $B^\pm \rightarrow D\pi^\pm$  decays were affected by  $CP$  violation in the neutral kaon sector. The impact had been shown to scale as  $\mathcal{O}(|\epsilon|/r_B)$  [74], which is negligible for the  $B^\pm \rightarrow DK^\pm$  channel but suggests potentially large biases in the  $B^\pm \rightarrow D\pi^\pm$  channel, where  $r_B$  is 20 times smaller. However, the dedicated analysis presented in Chapter 3 has proved the effect on GGSZ measurements to be in fact be *smaller* than  $\mathcal{O}(|\epsilon|/r_B)$  and the simultaneous measurement is indeed viable.

The measurement is performed by making extended maximum-likelihood fits to the  $m_B$  spectra of  $B \rightarrow D(\rightarrow K_S^0 h^+ h^-)h'^\pm$  candidates split by charge and Dalitz bin. The  $B^\pm \rightarrow DK^\pm$  signal yields are parameterised using the expressions in Eq. (1.41) directly, thus obtaining values for  $x_\pm^{DK}$  and  $y_\pm^{DK}$  directly. The Cartesian  $CP$ -violating observables  $x_\pm$  and  $y_\pm$  are employed because they lead to better statistical behaviour than fits to data where the underlying parameters  $(\gamma, r_B^{DK^\pm}, \delta_B^{DK^\pm})$  are determined [], at the cost of introducing a fourth degree of freedom. With the addition of the  $B^\pm \rightarrow D\pi^\pm$  mode as a true signal channel, two new underlying parameters are introduced,  $r_B^{D\pi^\pm}$  and  $\delta_B^{D\pi^\pm}$ . It is only necessary to introduce an additional two, not four, Cartesian parameters [75] by defining

$$\xi_{D\pi^\pm} = \left( \frac{r_B^{D\pi^\pm}}{r_B^{DK^\pm}} \right) \exp[i(\delta_B^{D\pi^\pm} - \delta_B^{DK^\pm})] \quad (1.44a)$$

676 and letting

$$x_\xi^{D\pi} = \text{Re}[\xi_{D\pi^\pm}] \quad y_\xi^{D\pi} = \text{Im}[\xi_{D\pi^\pm}]. \quad (1.44\text{b})$$

677 In terms of these parameters, the usual Cartesian  $x_\pm$  and  $y_\pm$  are given by

$$x_\pm^{D\pi} = x_\xi^{D\pi} x_\pm^{DK} - y_\xi^{D\pi} y_\pm^{DK}, \quad y_\pm^{D\pi} = x_\xi^{D\pi} y_\pm^{DK} + y_\xi^{D\pi} x_\pm^{DK}. \quad (1.45)$$

678 Using this expression, the  $B^\pm \rightarrow D\pi^\pm$  yields can also be defined via Eq. (1.41) in the  
679 maximum-likelihood fit. This allows for a stable fit for all six  $x$  and  $y$  parameters, as  
680 well as the shared  $F_i$ , as described in much greater detail in Chapter 4. Note that  $\xi$   
681 does not depend on  $\gamma$ : all information on  $CP$  asymmetries in both the  $B^\pm \rightarrow DK^\pm$   
682 and  $B^\pm \rightarrow D\pi^\pm$  channels is encoded in  $x_\pm^{DK}$  and  $y_\pm^{DK}$ .

683 The combined analysis of  $B^\pm \rightarrow DK^\pm$  and  $B^\pm \rightarrow D\pi^\pm$  decays presents a sig-  
684 nificant step forward, because it solves the problem of obtaining  $F_i$  parameters  
685 for the appropriate acceptance profile in a manner that avoids leading systematic  
686 uncertainties, and almost all reliance on simulation. This is of great importance,  
687 if the large data samples that will be collected by LHCb in the future are to be  
688 exploited to their full potential.

# 2

689

690

## The LHCb experiment

691 We have a detector? I thought ntuples were made of magic.

### 692 **2.1 Subdetectors**

693 **2.1.1 The VELO**

694 **2.1.2 Magnet and tracking stations**

695 **2.1.3 The RICH**

696 **2.1.4 Calorimeters**

697 **2.1.5 Muon detectors**

### 698 **2.2 Track reconstruction**

### 699 **2.3 The LHCb triggering system**

700 **2.3.1 The level-0 hardware trigger**

701 **2.3.2 High-level triggers**

702 **2.3.3 Offline data filtering: the LHCb stripping**

### 703 **2.4 Simulation**

704 A short description of truth matching: note that all simulation samples described

705 in the thesis have been truth matched appropriately.

706      Include a short description of RapidSim.

# 3

707

708

709

## Neutral kaon $CP$ violation and material interaction in BPGGSZ measurements

710 The presence of a  $K_S^0$  meson in the  $D \rightarrow K_S^0 h^+ h^-$  final states introduces a small  
711 bias in BPGGSZ measurements due to  $CP$ -violation in the neutral kaon sector  
712 and asymmetries caused by the interaction between the neutral kaons and detector  
713 material. These fundamental physics effects are reviewed in Section 3.1, after which  
714 the chapter presents a detailed analysis of the impact on the LHCb measurement  
715 that is the subject of the thesis, as well as future  $\gamma$  measurements with the Belle II  
716 experiment. Prior to this analysis, the only existing work on the effect on  $\gamma$   
717 measurements suggested a small effect in  $B^\pm \rightarrow D K^\pm$  measurements but potentially  
718 very significant effects in measurements based on  $B^\pm \rightarrow D \pi^\pm$  decays [74]. However,  
719 as described in Section 3.1.1, the analysis in Ref. [74] does not take into account  
720 the fundamental aspect of the BPGGSZ method: that it relies on the phase-space  
721 distribution of signal decays, not phase-space integrated asymmetries. Furthermore,  
722 the study only considers the  $CP$ -violation effect, not material interaction. Therefore,  
723 a more detailed study was necessary before the  $B^\pm \rightarrow D \pi^\pm$  decay mode could  
724 reliably be promoted to a signal channel.

725

726

### 3.1 $CP$ violation and material interaction of neutral kaons

727

728

A brief review of the general phenomenology of mixing and  $CP$  violation in the neutral kaon system is useful, before analysing the impact on  $\gamma$  measurements.

The presentation in this section follows the PDG review of *CP violation in the quark section* [76]. The general theory considers any pair of neutral mesons  $|M^0\rangle$  and  $|\bar{M}^0\rangle$  related by  $CP$  conjugation

$$CP|M^0\rangle = e^{i\phi_M}|\bar{M}^0\rangle \quad CP|\bar{M}^0\rangle = e^{-i\phi_M}|M^0\rangle, \quad (3.1a)$$

where  $\phi_M$  is an arbitrary phase. In this thesis, the convention  $\phi_M = 0$  is chosen to equal zero, so that

$$CP|M^0\rangle = |\bar{M}^0\rangle \quad CP|\bar{M}^0\rangle = |M^0\rangle. \quad (3.1b)$$

A meson state that starts as a general superposition of  $|M^0\rangle$  and  $|\bar{M}^0\rangle$  states

$$\begin{aligned} \psi_M^0 &\equiv \psi_M(0) = a(0)|M^0\rangle + b(0)|\bar{M}^0\rangle \\ &\equiv \psi_{M^0}^0 + \psi_{\bar{M}^0}^0 \end{aligned} \quad (3.2)$$

will, over time, involve into a state that consists of a different superposition of  $|M^0\rangle$  and  $|\bar{M}^0\rangle$ , as well as components for all possible states the meson system can decay into

$$\begin{aligned} \psi_M(t) &= a(t)|M^0\rangle + b(t)|\bar{M}^0\rangle + \sum c_i(t)f_i \\ &\equiv \psi_{M^0}(t) + \psi_{\bar{M}^0}(t) + \sum c_i(t)f_i. \end{aligned} \quad (3.3)$$

For time scales that are longer than the typical strong-interaction, the time evolution of the  $M^0-\bar{M}^0$  superposition can be described by a  $2 \times 2$  Hamiltonian

$$\frac{d}{dt} \begin{pmatrix} \psi_{M^0}(t) \\ \psi_{\bar{M}^0}(t) \end{pmatrix} = -i\mathcal{H}_0 \begin{pmatrix} \psi_{M^0}(t) \\ \psi_{\bar{M}^0}(t) \end{pmatrix} \quad (3.4)$$

that is *non-Hermitian* (to allow for decay) but can be parameterised in terms of two Hermitian matrices  $\mathcal{M}$  and  $\Gamma_0$

$$\mathcal{H}_0 = \mathcal{M} - \frac{i}{2}\Gamma_0. \quad (3.5)$$

The quantum states with well-defined (real) masses,  $m_j$ , and (real) decay widths,  $\Gamma_j$ , are the two eigenstates of  $\mathcal{H}_0$  with eigenvalues  $\lambda_j = m_j - \frac{i}{2}\Gamma_j$ . The eigenstates (of course) evolve independently in time, so that

$$\psi_j(t) = e^{-i\lambda_j t}\psi_j^0 = e^{-im_j t - \frac{\Gamma_j}{2}t}\psi_j^0. \quad (3.6)$$

The eigenstates are denoted  $H$  and  $L$  according to the size of  $m_j$ , the real part of the eigenvalues, such that  $m_H > m_L$ . Assuming that  $\mathcal{H}_0$  conserves  $CPT$  the eigenstates have the general form

$$\begin{aligned} |M_H\rangle &\equiv p|M^0\rangle - q|\bar{M}^0\rangle \\ |M_L\rangle &\equiv p|M^0\rangle + q|\bar{M}^0\rangle \end{aligned} \quad (3.7)$$

where  $p$  and  $q$  are complex numbers that satisfy  $|q|^2 + |p|^2 = 1$ . With the convention in Eq. (3.1b) it follows that if  $\mathcal{H}_0$  also conserves  $CP$ , so that  $|M_H\rangle$  and  $|M_L\rangle$  are  $CP$  eigenstates, then  $p = \pm q$ , where the sign depends on which of the heavy and the light meson states is  $CP$  even, and which is  $CP$  odd.

The eigenstates of the Hamiltonian governing the neutral kaon system are almost, but not exactly, equal to the  $CP$  eigenstates

$$|K_1\rangle = \frac{|K^0\rangle + |\bar{K}^0\rangle}{\sqrt{2}} \quad |K_2\rangle = \frac{|K^0\rangle - |\bar{K}^0\rangle}{\sqrt{2}}, \quad (3.8)$$

which are  $CP$  even and odd, respectively. This approximate equality leads to the most prominent feature of the neutral kaon system: the two eigenstates of  $\mathcal{H}_0$  have lifetimes that differ by orders of magnitude. This is best understood by assuming, for a moment, that the states in Eq. (3.8) *do* equal the eigenstates with definite life times. The  $K_1$  state can decay in the  $CP$  even  $\pi^+\pi^-$  and  $\pi^0\pi^0$  modes, and does so almost 100% of the time; these decay modes are not available to the  $K_2$  (in the absence of direct  $CP$  violation) which results in a much lower decay rate and much longer life time. Therefore, the eigenstates in the kaon system are labelled the *short-lived* kaon,  $K_S^0$ , which is almost  $CP$  even, and the *long-lived* kaon,  $K_L^0$ , which is almost  $CP$  odd. The life times are [76]

$$\tau_{K_S^0} = (8.954 \pm 0.004) \times 10^{-11} \text{s} \quad \tau_{K_L^0} = (5.116 \pm 0.021) \times 10^{-8} \text{s}. \quad (3.9)$$

Experimentally, it is found that the  $K_S^0$  corresponds to the light eigenstate, but that the mass splitting [76]

$$\begin{aligned} \Delta m = m_{K_L^0} - m_{K_S^0} &= (0.5289 \pm 0.0009) \times 10^{10} \hbar s^{-1} \\ &\simeq 3.5 \times 10^{-6} \text{ eV} \end{aligned} \quad (3.10)$$

is tiny compared to the neutral kaon masses of  $m_{K_S^0} = 497.6 \text{ MeV}/c^2$  [76].

However, the discovery of  $K_L^0 \rightarrow \pi\pi$  decays by Kronin and Fitch in 1964 established that the  $K_S^0$  and  $K_L^0$  are *not* exactly equal to the  $CP$  eigenstates in Eq. (3.8), because the  $\mathcal{H}_0$  relevant to the kaon system is  $CP$ -violating. The  $CP$  violation in the kaon sector is conventionally parameterised in terms of the complex parameters  $\epsilon$  and  $\epsilon'$ , in terms of which

$$\frac{A(K_L^0 \rightarrow \pi^+\pi^-)}{A(K_S^0 \rightarrow \pi^+\pi^-)} = \epsilon + \epsilon' \quad \frac{A(K_L^0 \rightarrow \pi^0\pi^0)}{A(K_S^0 \rightarrow \pi^0\pi^0)} = \epsilon - 2\epsilon'. \quad (3.11)$$

In these expressions  $\epsilon$  denotes the contribution from  $CP$  violation in mixing and  $\epsilon'$  the contribution due to direct  $CP$  violation in the decays. The  $\epsilon$  parameter has been measured to be [76]

$$|\epsilon| = (2.228 \pm 0.011) \times 10^{-3}, \quad \arg \epsilon = (43.52 \pm 0.05)^\circ. \quad (3.12)$$

775 Direct  $CP$  violation is ignored for the remainder of the thesis, because  $\epsilon'$  is measured  
776 to be three orders of magnitude smaller than  $\epsilon$ . In terms of the  $CP$  eigenstates  
777 of Eq. (3.8), the mass eigenstates  $K_S^0$  and  $K_L^0$  are given by

$$\begin{aligned} |K_S^0\rangle &= \frac{|K_1\rangle + \epsilon|K_2\rangle}{\sqrt{1+|\epsilon|^2}} &= \frac{(1+\epsilon)|K^0\rangle + (1-\epsilon)|\bar{K}^0\rangle}{\sqrt{2(1+|\epsilon|^2)}} \\ |K_L^0\rangle &= \frac{|K_2\rangle + \epsilon|K_1\rangle}{\sqrt{1+|\epsilon|^2}} &= \frac{(1+\epsilon)|K^0\rangle - (1-\epsilon)|\bar{K}^0\rangle}{\sqrt{2(1+|\epsilon|^2)}}, \end{aligned} \quad (3.13)$$

778 corresponding to the definition  $p = (1+\epsilon)/\sqrt{2(1+|\epsilon|^2)}$  and  $q = (1-\epsilon)/\sqrt{2(1+|\epsilon|^2)}$   
779 in Eq. (3.7).

780 In an experimental setting, the time evolution of a neutral kaon state is affected  
781 by nuclear interactions with the detector. The interaction is governed by the strong  
782 force, and therefore sensitive to the *flavour* of the kaon state; the interaction  
783 strength is thus different for  $K^0$  and  $\bar{K}^0$  mesons. This difference introduces a  
784 non-zero  $K_S^0 \leftrightarrow K_L^0$  transition amplitude for neutral kaons traversing a detector  
785 segment. This effect was predicted early in the history of kaon physics [77] and is  
786 commonly denoted *kaon regeneration*. The effect can be described by including a  
787 material-interaction term in the Hamiltonian that is diagonal in the  $(|K^0\rangle, |\bar{K}^0\rangle)$   
788 basis, so that the equation governing the time evolution is [78, 79]

$$\frac{d}{dt} \begin{pmatrix} \psi_{K^0}(t) \\ \psi_{\bar{K}^0}(t) \end{pmatrix} = -i \left[ \mathcal{H}_0 + \begin{pmatrix} \chi & 0 \\ 0 & \bar{\chi} \end{pmatrix} \right] \begin{pmatrix} \psi_{K^0}(t) \\ \psi_{\bar{K}^0}(t) \end{pmatrix}. \quad (3.14)$$

789 The complex parameters  $\chi$  and  $\bar{\chi}$  describe the material interaction of the  $K^0$   
790 and  $\bar{K}^0$  flavour eigenstates and are related to their scattering cross section, as  
791 described further in Section 3.3.4. The solution of Eq. (3.14) for the time evolution  
792 in the  $K_S^0$  and  $K_L^0$  states is [79]

$$\begin{aligned} \psi_S(t) &= e^{-i\Sigma t} \left( \psi_S^0 \cos \Omega t + \frac{i}{2\Omega} (\Delta\lambda\psi_S^0 - \Delta\chi\psi_L^0) \sin \Omega t \right), \\ \psi_L(t) &= e^{-i\Sigma t} \left( \psi_L^0 \cos \Omega t - \frac{i}{2\Omega} (\Delta\lambda\psi_L^0 + \Delta\chi\psi_S^0) \sin \Omega t \right), \end{aligned} \quad (3.15)$$

793 in terms of the parameters

$$\begin{aligned} \Delta\chi &= \chi - \bar{\chi}, \\ \Delta\lambda &= \lambda_L - \lambda_S = (m_L - m_S) - \frac{i}{2}(\Gamma_L - \Gamma_S), \\ \Sigma &= \frac{1}{2}(\lambda_S + \lambda_L + \chi + \bar{\chi}), \\ \Omega &= \frac{1}{2}\sqrt{\Delta\lambda^2 + \Delta\chi^2}. \end{aligned} \quad (3.16)$$

794 In the vacuum limit where  $\chi = \bar{\chi} = 0$ , the expressions in Eq. (3.6) and Eq. (3.15) are  
795 equal.

### 3.1.1 A first look at the impact on $\gamma$ measurements

The effects described above have an impact on measurements of  $CP$  asymmetries in modes with a neutral kaon in the final state. This was analysed for the first time in relation to  $\gamma$  measurements by Grossman and Savastio in 2014 [74]. The authors point out two sources of corrections to be included:

- the fact that  $K_S^0$  is not an exact  $CP$  eigenstate can break potential symmetry relations employed in an analysis, and
- that when the neutral kaon is reconstructed in a  $\pi\pi$  final state there will be contributions from both  $K_S^0$  and  $K_L^0$  decays.

The analysis in this chapter considers yet another effect, not treated by Grossman and Savastio, namely that

- material interaction can emulate the effect of neutral kaon  $CP$  violation, because it couples the almost- $CP$ -even  $K_S^0$  and the almost- $CP$ -odd  $K_L^0$  states.

Due to the presence of  $K_L^0 \rightarrow \pi\pi$  decays, Grossman and Savastio point out that the relevant decay rates to consider in an experimental setting are of the form

$$d\Gamma(t) \propto |\psi_S(t) + \epsilon\psi_L(t)|^2. \quad (3.17)$$

The time dependence of the decay rates considered in Chapter 1 was left out because all terms shared a common time dependence. That is not the case in Eq. (3.17), due to the very different decay rates of the  $K_S^0$  and  $K_L^0$  components of the kaon state. As a consequence, the time-integrated yields have the form

$$N \propto \int dt \eta(t) |\psi_S(t) + \epsilon\psi_L(t)|^2, \quad (3.18)$$

where  $\eta(t)$  is the time acceptance in a given experimental setting. Thus, the acceptance is crucial to model in order to correctly estimate the impact of kaon  $CP$ -violation effects on a given measurement.

Considering BPGBSZ measurements, the main effect of neutral kaon  $CP$  violation is a breakdown of the fundamental Dalitz-plot symmetry that is exploited in the derivation of the bin yield equations. Extending the amplitude definition of Eq. (1.21) to include  $K_L^0$  decays

$$A_{S(L)}^{(\overline{D})}(s_-, s_+) = A((\overline{D})^0 \rightarrow K_{S(L)}^0 \pi^+ \pi^-), \quad (3.19)$$

the authors point out that  $CP$ -violation in the  $K_S^0$  system means that the relation  $A_S^{(\overline{D})}(s_{-+}) = A_S^D(s_{+-})$  is not exactly true; and in addition, there is now a

dependence on  $A_L^D(s_{-+})$  which satisfies a different approximate symmetry, namely  $A_L^{\bar{D}}(s_{-+}) \simeq -A_L^D(s_{+-})$ . Grossman and Savastio describe these symmetry breaking effects in detail, but do not explicitly derive the corrections to the yield equations of Chapter 1, nor try to quantify the potential bias on  $\gamma$  in a measurement based on the binned yields. Instead, they derive expressions for the bias in a measurement obtained from phase-space integrated  $CP$  asymmetries. This is done for both GLW measurements that use  $D \rightarrow K_S^0 X$  final states and for the  $D \rightarrow K_S^0 h^+ h^-$  final states; however, for their quantitative estimate of  $\Delta\gamma$  the authors make an approximation that corresponds to assuming that the  $D \rightarrow K_S^0 h^+ h^-$  final state is a  $CP$  eigenstate, making the two results identical. The authors find that in this case, assuming a uniform experimental acceptance for all kaon decay times, the asymmetry has the form<sup>1</sup>

$$A = \frac{2r_B \sin \gamma \sin \delta_B + 2\text{Re}[\epsilon]}{1 + r_B^2 - 2r_B \cos \gamma \cos \delta_B}, \quad (3.20)$$

If a measured value of  $A$  is interpreted to obtain  $\gamma$  without taking the  $\epsilon$  term into account, it leads to a bias of

$$\Delta\gamma = -\frac{\text{Re}[\epsilon]}{r_B \cos \gamma \sin \delta_B} + O(|\epsilon|). \quad (3.21)$$

The scaling  $\Delta\gamma \sim \mathcal{O}(r_B/|\epsilon|)$  is the main result of the analysis by Grossman and Savastio. For  $B^\pm \rightarrow D K^\pm$  decays, where  $r_B^{DK^\pm} \simeq 0.1$  this suggests a bias at the percent level, which is negligible compared to current experimental uncertainties. However, in the  $B^\pm \rightarrow D \pi^\pm$  case, where  $r_B^{D\pi^\pm} \simeq 0.005$  [47], their result suggests relative biases that are potentially of  $\mathcal{O}(1)$ .

The conclusions are lacking on two accounts, however. Firstly, as made clear in Section 1.3.5, the  $K_S^0 \pi^+ \pi^-$  and  $K_S^0 K^+ K^-$  states are *far from*  $CP$  eigenstates. From the asymmetry expression in that section, it is clear that the bias in a determination of  $\gamma$  based on phase-space asymmetries will in fact scale as

$$\Delta\gamma \sim \mathcal{O}\left(\frac{|\epsilon|}{(2\mathcal{F}_+ - 1)r_B}\right), \quad (3.22)$$

which suggests that Grossman and Savastio severely *underestimates* the potential impact. This is described in detail in Section 3.2.3. More importantly, the analysis of the phase-space integrated asymmetry is in fact *irrelevant* to BPGGSZ measurements as they are currently performed: as described in Section 1.3.5 the information from

---

<sup>1</sup>In fact the expression in Eq. (3.20) is missing a term, as will be clear when an analogous expression is derived in detail in Section 3.2.3.

the global asymmetry is completely discarded. Therefore it is necessary to analyse the effects of kaon  $CP$ -violation on a full, binned analysis of  $D \rightarrow K_S^0 h^+ h^-$  decays, which is done in detail in the following sections. While the aim is to extend the analysis if Grossman and Savastio, the treatment in the following sections is completely independent of that in Ref. [74].

## 3.2 Impact on BPGBSZ measurements of $\gamma$ : principles

The analysis of the impact on BPGBSZ measurements is carried out in two stages. This section treats the leading order effects analytically, and derives the overall order of magnitude of the expected bias in a general setting. Then Section 3.3 presents a detailed numerical study of the expected effect in measurements with the LHCb and Belle II experiments specifically, because these will be crucial to constrain  $\gamma$  during the coming decade [80, 81].

### 3.2.1 Modified symmetry relations

In order to derive the corrections to the asymmetry relation  $A_S^D(s_{-+}) \simeq A_S^{\bar{D}}(s_{+-})$ , it is beneficial to express  $A_{S(L)}^D$  in terms of the amplitudes

$$A_{1/2}^{\bar{D}} = A(\bar{D}^0 \rightarrow K_{1/2}^0 \pi^+ \pi^-), \quad (3.23)$$

because these amplitude satisfy the exact symmetries  $A_1^D(s_{-+}) = A_1^{\bar{D}}(s_{+-})$  and  $A_2^D(s_{-+}) = -A_2^{\bar{D}}(s_{+-})$ . This approach is different to that of Grossman and Savastio, but the final results are equivalent. After the decay of a  $D^0$  meson to a neutral kaon, the kaon state is

$$\begin{aligned} \psi^0 &= A_1^D |K_1\rangle + A_2^D |K_2\rangle \\ &= N \left[ (A_1^D - \epsilon A_2^D) |K_S^0\rangle + (A_2^D - \epsilon A_1^D) |K_L^0\rangle \right], \end{aligned} \quad (3.24)$$

with the normalisation constant  $N = \sqrt{1 + |\epsilon|^2}/(1 - \epsilon^2)$ . Thus it can be seen that

$$\begin{aligned} A_S^D(s_{-+}) &= N \left[ (A_1^D(s_{-+}) - \epsilon A_2^D(s_{-+})) \right], \\ A_L^D(s_{-+}) &= N \left[ (A_2^D(s_{-+}) - \epsilon A_1^D(s_{-+})) \right], \end{aligned} \quad (3.25)$$

with an analogous expression for the  $\bar{D}^0$  decay amplitudes. Therefore, the generalised relations between the  $D^0$  and  $\bar{D}^0$  amplitudes are

$$\begin{aligned} A_S^{\bar{D}}(s_{+-}) &= N[A_1^{\bar{D}}(s_{+-}) - \epsilon A_2^{\bar{D}}(s_{+-})] \\ &= N[A_1^D(s_{-+}) + \epsilon A_2^D(s_{-+})] = A_S^D(s_{-+}) + 2N\epsilon A_2^D(s_{-+}), \\ A_L^{\bar{D}}(s_{+-}) &= N[A_2^{\bar{D}}(s_{+-}) - \epsilon A_1^{\bar{D}}(s_{+-})] \\ &= -N[A_2^D(s_{-+}) + \epsilon A_1^D(s_{-+})] = -A_L^D(s_{-+}) - 2N\epsilon A_1^D(s_{-+}). \end{aligned} \quad (3.26)$$

### 3.2.2 Relationship between the $K_S^0$ and $K_L^0$ amplitudes

The decay amplitude  $A(D^0 \rightarrow K_S^0 \pi^+ \pi^-)$  has been carefully studied, and a number of amplitude models have been published [51, 56–58, 61]. No models have been published for  $D^0 \rightarrow K_L^0 \pi^+ \pi^-$  decays. However, following an approach laid out by the CLEO collaboration [69], the two amplitudes can be related. Again, this is most easily done by relating the  $A_1^D(s_{+-})$  and  $A_2^D(s_{+-})$  amplitudes. In the isobar formalism, the decay amplitude  $A(D^0 \rightarrow K_1 \pi^+ \pi^-)$  is expressed as a non-resonant constant amplitude plus a sum of resonances

$$A(D^0 \rightarrow K_1 \pi^+ \pi^-) = k_{NR} + \sum_{CF} k_i R^i(s_{K\pi^-}) + \sum_{DCS} k_j R^j(s_{K\pi^+}) + \sum_{R_{\pi\pi}} k_k R^k(s_{\pi^+\pi^-}). \quad (3.27)$$

The resonances are split into Cabibbo-favoured (CF)  $K^{*-}$  resonances, doubly Cabibbo-suppressed (DCS)  $K^{*+}$  resonances and  $\pi\pi$  resonances.<sup>2</sup> The CF resonances couple to the  $\bar{K}^0$  component of  $K_1 (\propto K^0 + \bar{K}^0)$ , and therefore the corresponding  $k_i$  in the  $K_2 (\propto K^0 - \bar{K}^0)$  amplitude will have a relative minus sign. The DCS resonances couple to the  $K^0$  component of  $K_1$ , and so the corresponding  $k_j$  in the  $K_2$  amplitude will have a relative plus sign. For the  $h^+ h^-$  resonances, there will be a coupling to both the  $K^0$  and  $\bar{K}^0$  components, however the coupling to the  $K^0$  component is expected to be suppressed with a Cabibbo suppression factor  $r_k e^{i\delta_k}$ , where  $r_k \simeq \tan^2 \theta_C \simeq 0.05$  is determined by the Cabibbo angle  $\theta_C$  and  $\delta_k$  can take any value. Therefore, the  $k_k$  for these resonances have a relative  $-(1 - 2r_k e^{i\delta_k})$  factor in the  $K_2$  amplitude. The same effect leads to the differences in decay rates between  $D^0 \rightarrow K_S^0 \pi^0$  and  $D^0 \rightarrow K_L^0 \pi^0$  decays [82, 83]. Thus, given a model of the

---

<sup>2</sup>In modern models, the  $\pi\pi$  and  $K\pi$   $S$ -wave components are modelled via the  $K$ -matrix formalism and LASS parametrisations, respectively, instead of sums of individual resonances [51]. This does not alter the arguments below, as the  $R$  functions of Eq. (3.27) can equally well represent such terms.

894 form in Eq. (3.27), a model for the  $A(D^0 \rightarrow K_2\pi^+\pi^-)$  amplitude will have the form

$$A(D^0 \rightarrow K_2\pi^+\pi^-) = k_{NR} + \sum_{CF} (-k_i) R^i(s_{K\pi^-}) + \sum_{DCS} (+k_j) R^j(s_{K\pi^+}) \\ + \sum_{R_{\pi\pi}} (-(1 - 2r_k e^{i\delta_k}) k_k) R^k(s_{\pi^+\pi^-}). \quad (3.28)$$

895 An important consequence of these substitution rules is that

$$A_2^D(s_{+-}) = -A_1^D(s_{+-}) + r_A \Delta A(s_{+-}), \quad (3.29)$$

896 where  $r_A \simeq \tan^2 \theta_C$  and  $\Delta A(s_{+-}) \sim A_1^D(s_{+-})$  are of the same order of magnitude  
897 (at least when averaged over the bins used in  $\gamma$  measurements). This relation is  
898 sufficient to make the qualitative arguments of this section, while the full set of  
899 substitution rules above are used in the quantitative studies of Section 3.3.

### 900 3.2.3 Modification of the BPGBSZ yield equations

901 With suitable models to calculate  $A_{S(L)}^{\bar{D}}$  (or  $A_{1/2}^{\bar{D}}$ ) and knowledge of  $\Delta\chi$  for the  
902 materials relevant to an experimental setting, the relations derived in the preceding  
903 sections can be employed to calculate the expected phase-space bin yields,  $N_i^\pm$ ,  
904 including the effects of kaon  $CP$  violation and material interaction. The decay  
905 rates have additional terms compared to those in Eq. (1.24), because the  $K_L^0$   
906 contribution must be taken into account

$$d\Gamma(t, s_{+-}) \propto |\psi_S(t, s_{+-}) + \epsilon\psi_L(t, s_{+-})|^2, \quad (3.30)$$

907 where the time-dependence of  $\psi_{S/L}(t, s_{+-})$  is governed by Eq. (3.15), and the phase-  
908 space dependence is included in the state component, by defining  $\psi_{S/L}^0$  in terms of  
909  $A_{S(L)}^{\bar{D}}(s_{+-})$ . For example, for the case of a  $B^- \rightarrow DK^-$  decay, the definition is

$$\begin{aligned} \psi_{S/L}^{0,B^-}(s_{+-}) &= A_S^D(s_{+-}) + r_B e^{i(\delta_B - \gamma)} A_S^{\bar{D}}(s_{+-}) \\ &= A_1^D(s_{+-}) - \epsilon A_2^D(s_{+-}) + r_B e^{i(\delta_B - \gamma)} (A_1^{\bar{D}}(s_{+-}) - \epsilon A_2^{\bar{D}}(s_{+-})) \\ &= A_1^D(s_{+-}) - \epsilon A_2^D(s_{+-}) + r_B e^{i(\delta_B - \gamma)} (A_1^D(s_{+-}) + \epsilon A_2^D(s_{+-})). \end{aligned} \quad (3.31)$$

910 It is useful to look at the corrections to the BPGBSZ yield expressions in Eq. (1.25)  
911 to lowest order in  $\epsilon$  and  $r_\chi = \frac{1}{2} \frac{\Delta\chi}{\Delta\lambda}$ , the dimensionless parameter governing material  
912 interactions. For LHCb and Belle II the average  $|r_\chi| \simeq 10^{-3}$ , as detailed in the  
913 Section 3.3. To first order in  $r_\chi$ , the time-dependent kaon states within a material,  
914 given in Eq. (3.15), simplify to [79]

$$\begin{aligned} \psi_S(t, s_{+-}) &= e^{-\frac{i}{2}(x+\bar{x})t} e^{-i\lambda_S t} (\psi_S^0(s_{+-}) - r_\chi (1 - e^{-i\Delta\lambda t}) \psi_L^0(s_{+-})), \\ \psi_L(t, s_{+-}) &= e^{-\frac{i}{2}(x+\bar{x})t} e^{-i\lambda_L t} (\psi_L^0(s_{+-}) + r_\chi (1 - e^{+i\Delta\lambda t}) \psi_S^0(s_{+-})). \end{aligned} \quad (3.32)$$

By inserting these expressions into Eq. (3.30) and employing the definition in Eq. (3.31) (and a similar definition for  $B^+$  decays), the binned yields can be calculated by an integration over time and phase space. In the remainder of this section, it is assumed that the experimental time acceptance is  $\eta(t) = 1$  for all times and that  $r_\chi$  is constant at all times; more realistic assumptions are introduced in Section 3.3. In this case, the binned yields are given by the expression

$$\begin{aligned} N_i^- &= h_B^{-'} \left( \hat{K}_{+i} + r_B^2 \hat{K}_{-i} + 2\sqrt{\hat{K}_{+i} \hat{K}_{-i}} (x_- \hat{c}_i + y_- \hat{s}_i) + O(r\epsilon) \right), \\ N_i^+ &= h_B^{+'} \left( \hat{K}_{-i} + r_B^2 \hat{K}_{+i} + 2\sqrt{\hat{K}_{+i} \hat{K}_{-i}} (x_+ \hat{c}_i - y_+ \hat{s}_i) + O(r\epsilon) \right), \end{aligned} \quad (3.33)$$

where a number of new parameters have been defined, and where  $O(r\epsilon)$  denotes terms of  $O(r_A\epsilon)$ ,  $O(r_B\epsilon)$ ,  $O(r_A r_\chi)$ , and  $O(r_B r_\chi)$ . Since  $r_B \sim r_A \sim 10^{-1}$  (in  $B^\pm \rightarrow D K^\pm$  decays) and  $r_\chi \sim \epsilon \sim 10^{-3}$ , these terms are all of the same order of magnitude.

The new normalisation constants  $h_B^{\pm'} = h_B^\pm (1 + |\epsilon + r_\chi|^2 \frac{\Gamma_S}{\Gamma_L} \mp \Delta h)$  are defined in terms of

$$\Delta h = 2\text{Re}[\epsilon + r_\chi] - 4 \frac{\Gamma_S}{\Gamma_L + \Gamma_S} \frac{\text{Re}[\epsilon + r_\chi] + \mu \text{Im}[\epsilon + r_\chi]}{1 + \mu^2}, \quad \mu = 2 \frac{m_L - m_S}{\Gamma_L + \Gamma_S}. \quad (3.34)$$

The  $\hat{K}_i$  parameters are defined to be

$$\hat{K}_i = \frac{1}{1 + |\epsilon + r_\chi|^2 \frac{\Gamma_S}{\Gamma_L}} \left( K_i^{(1)} + |\epsilon + r_\chi|^2 \frac{\Gamma_S}{\Gamma_L} K_i^{(2)} \right), \quad (3.35)$$

in which the  $K_i^{(1/2)}$  parameters are phase-space integrals, defined as in Eq. (1.27) but for  $A_{1/2}^D$ . To lowest order, the  $\hat{K}_i$  correspond to the fractional  $D^0$  decay yield in each bin, as obtained in a measurement that averages  $D^0$  and  $\bar{D}^0$  decays, and assumes the  $A_S^{\bar{D}}(s_{-+}) = A_S^D(s_{+-})$  symmetry to be exact:

$$K_i^{\text{meas}} \equiv \frac{N_i^D + N_{-i}^{\bar{D}}}{\sum_j N_j^D + N_{-j}^{\bar{D}}} = \hat{K}_i + \mathcal{O}(r\epsilon). \quad (3.36)$$

Here,  $N_i^D$  ( $N_i^{\bar{D}}$ ) is the expected yield of flavour tagged  $D^0$  ( $\bar{D}^0$ ) mesons into bin  $i$  of the  $D$  decay phase-space.

In similar fashion, the parameters  $(\hat{c}_i, \hat{s}_i)$  have been introduced to denote the measured average strong-phases, which are expected to differ from  $(c_i, s_i)$  at  $O(\epsilon)$ , since neutral kaon  $CP$  violation is not taken into account in the measurements by CLEO. Thus, any corrections arising if  $(\hat{c}_i, \hat{s}_i)$  and  $(c_i, s_i)$  are substituted in Eq. (3.33) will appear in the  $O(r_B\epsilon)$  terms.

Two observations can be made from the expression in (3.33). The first is that the phase-space distribution is only changed at  $O(r\epsilon)$  compared to the expression in

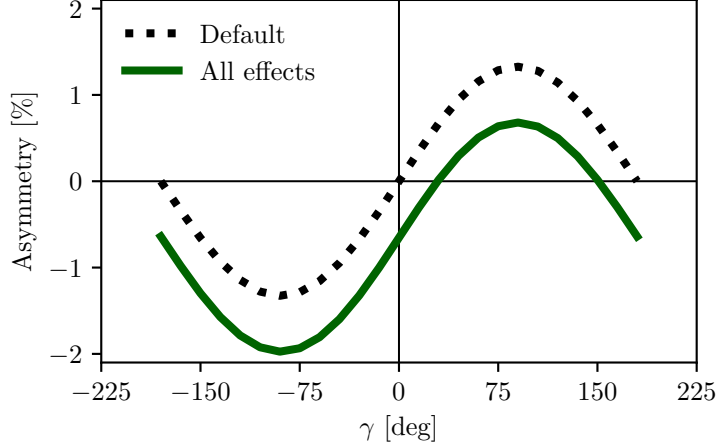


**Figure 3.1:** The asymmetry  $A_{\text{total}}$  as a function of  $\gamma$  calculated to  $O(\epsilon)$  using Eq. (3.37). The calculation is made using for (black dotted line) the default case where  $\Delta h = 0$  and (green) including neutral kaon  $CP$ -violation and material interaction with  $r_\chi = \epsilon$ .

Eq. (1.25), if the measured  $\hat{K}_i$  are used in the experimental analysis. This equally true whether the  $K_i$  are fitted in the signal channel along with  $x_\pm$  and  $y_\pm$ , as is the case in the measurement presented in the thesis, or if they are obtained in a control channel with flavour tagged  $D$  decays, according to Eq. (3.36). As the  $D^0 - \bar{D}^0$  interference term that provides sensitivity to  $\gamma$  enters at order  $O(r_B)$ , the impact on  $\gamma$  measurements can be expected to be  $\Delta\gamma/\gamma \sim O(r\epsilon/r_B)$ . For  $B \rightarrow DK$  analyses, where  $r_B \simeq 0.1$ , this is at the permille level, so the induced  $\Delta\gamma$  bias can be expected to be smaller than  $1^\circ$ . Even in the case of  $B^\pm \rightarrow D\pi^\pm$  decays, this suggests biases that are maximally a few percent. This is the main result of the chapter, because it means that the effect of neutral kaon  $CP$  violation and material interaction is small compared to the precision of the measurement that is the main subject of the thesis.

The second observation relates to potential future measurements of  $\gamma$ , which may also include sensitivity from the total, phase-space-integrated yield asymmetry

$$A_{\text{total}} = \frac{N^- - N^+}{N^- + N^+} = \frac{2(2\mathcal{F}_+ - 1)r_B \sin \delta_B \sin \gamma + \Delta h}{1 + r_B^2 + 2(2\mathcal{F}_+ - 1)r_B \cos \delta_B \cos \gamma} + O(r\epsilon), \quad (3.37)$$

where the definition of  $\mathcal{F}_+$  from Section 1.3.5 has been employed. In the limit  $r_B \rightarrow 0$  the expression agrees with the result for the analogous asymmetry in  $D^\pm \rightarrow \pi^\pm K_S^0$  decays in Ref. [84], evaluated to  $O(\epsilon)$  for an infinite and uniform time-acceptance. As hinted at above, the fact that  $\mathcal{F}_+ \simeq 0.5$  means that the asymmetry due to  $\gamma$  being non-zero is not  $\mathcal{O}(r_B)$ , but of approximately the same order of magnitude as the asymmetry due to  $CP$  violation in the neutral kaon sector, governed by  $\Delta h$ . This is illustrated in Fig. 3.1, where the expression in Eq. (3.37) is plotted in the default

case where  $\Delta h = 0$ , using the model in Ref. [51] to calculate  $K_i$  and  $c_i$ , as well as including neutral kaon  $CP$  violation and material interaction effects, calculated using  $r_\chi = \epsilon$ , with  $\epsilon$  taking the value in Eq. (3.12). The asymmetry changes significantly when including the latter effects. Therefore, measurements based only on the global asymmetry will suffer relative biases of tens of degrees, not a few degrees, if neutral kaon  $CP$  violation and material interaction is not taken into account.

### 3.3 Impact on BPGBSZ measurements of $\gamma$ : LHCb and Belle II measurements

The previous section has established that the bias due to neutral kaon  $CP$  violation and material interaction is at the sub-percent level for measurements based on  $B^\pm \rightarrow DK^\pm$  decays, and just a few percent in  $B^\pm \rightarrow D\pi^\pm$  decays. Thus, the effects only contribute a manageable systematic uncertainty in the measurement that is the subject of the thesis. However, the expected precision on  $\gamma$  measurements will increase significantly in the coming decade, as both the LHCb [81] and Belle II [80] collaborations expect to make BPGBSZ measurements that measure  $\gamma$  with a precision of 1–3°. Therefore a deeper understanding of the expected bias for these specific experiments is important.

This section details a study, where the equations of the previous section are evaluated numerically to all orders, and care is taken to realistically model the experiment specific conditions. The scope of the original analysis, published in Ref. [2], was a stand-alone paper that covers both LHCb and Belle II, and which therefore does not rely on full detector simulation. Instead the following approaches are taken to model the necessary input

- the experimental time-acceptance is modelled based on the detector geometry and typical neutral kaon momentum spectrum
- the material interaction is included, using the material budget information available in the technical design reports on each experiment
- both the time-acceptance and material interaction depends on the neutral kaon momentum, for which realistic distributions are estimated using the `RapidSim` simulation package [85].

Each input is described in detail in the following sections. The study has been repeated to assign a systematic uncertainty to the LHCb measurement in Chapter 4, with slight adjustments to match the exact fit setup and with the inputs above extracted from full LHCb simulation. This is described further in Section 3.3.7.

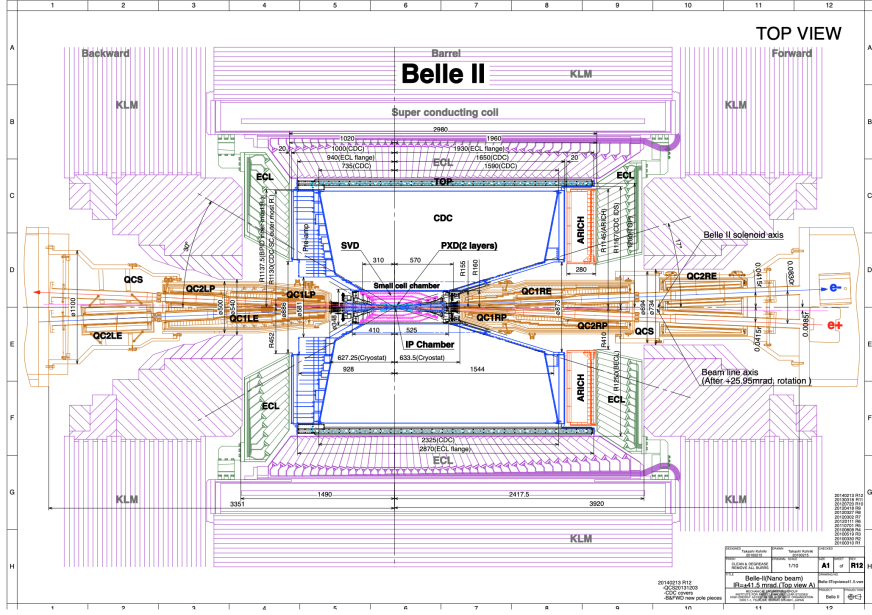


**Figure 3.2:** Schematic of the Belle II detector, reproduced from Ref. [80].

### 3.3.1 Detector geometries

The LHCb geometry and sub detectors are described in details in Chapter 2. In the LHCb measurement discussed in Chapter 4, the  $K_S^0$  mesons are reconstructed in the  $\pi^+\pi^-$  final state and two distinct categories of decay are considered, depending on where in the detector the  $K_S^0$  decay occurs. The categories have very different decay-time acceptance, and therefore two scenarios are considered for LHCb: one in which the decay products of the  $K_S^0$  leave reconstructed tracks in both the silicon vertex detector and downstream tracking detectors (denoted *long-long* or LL), and one in which the decay products of the  $K_S^0$  only leave tracks in the downstream tracking detectors (denoted *down-down* or DD).

The Belle II detector is a general purpose spectrometer, built to collect data from asymmetric  $e^+e^-$  collisions made by the SuperKEKB accelerator in Japan [80]. A schematic of the detector is shown in Fig. 3.2. The relevant sub detectors for the present study are the tracking detectors: a central silicon vertex detector, comprised of a total of six layers within 140 mm of the beam, and a large volume drift chamber with 56 wire layers, extending to a radius of 1130 mm [80]. A single scenario is considered for Belle II, because essentially all the  $K_S^0$  mesons produced in signal decays in Belle II decay within the tracking volume, with more than 90 % decaying in the vertex detector according to the studies described below. Thus, three scenarios are considered in total: LL LHCb, DD LHCb, and Belle II.

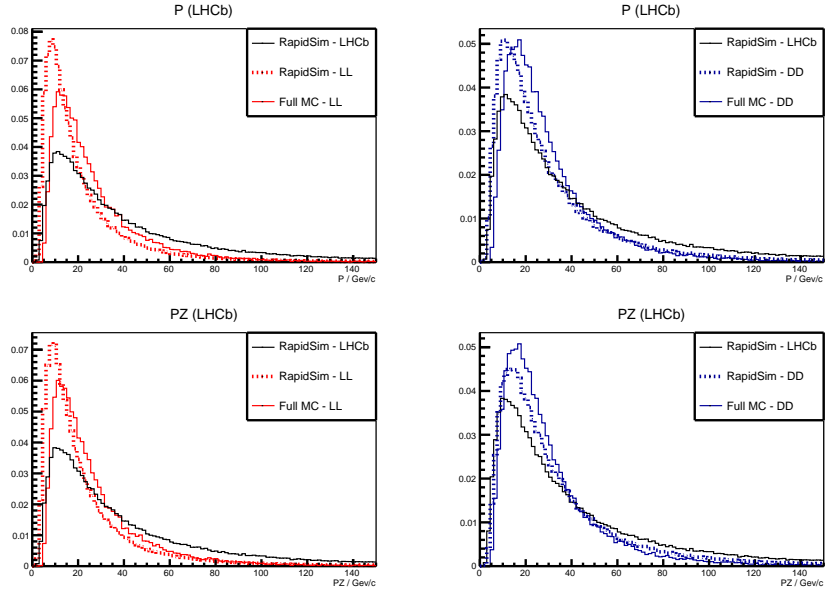


**Figure 3.3:** Momentum spectra for the  $K_S^0$  meson in LHCb, as generated using **RapidSim** (black lines) directly, as well as reweighted to match decay time acceptance in the (red) LL and (blue) DD data categories of LHCb. The LHCb spectra are compared with the spectra in fully simulated signal decays, for both (dotted red lines) LL and (dotted blue lines) DD data categories.

### 3.3.2 Kaon momentum distributions

The neutral kaon momentum distributions are obtained using **RapidSim** [85], a simple tool to generate MC samples. **RapidSim** has an inbuilt capability to generate decays of  $B$  mesons with the kinematic distribution found in LHCb collisions and falling in the LHCb acceptance. However, the distributions need to be reweighted to take the kaon-decay-time acceptance into account. After being reweighted, the **RapidSim** momentum spectra are reasonably close to those found in full LHCb simulation samples of  $B^\pm \rightarrow D(\rightarrow K_S^0\pi^+\pi^-)K^\pm$  decays, as seen in Fig. 3.3

At Belle II, the signal  $B$  mesons stem from decays of  $\Upsilon(4S)$  mesons produced in asymmetric electron-positron collisions. This leads to substantially different decay kinematics in comparison to those found at LHCb. The momentum distribution in Belle II is estimated by letting **RapidSim** decay  $B$  mesons with a momentum of 1.50 GeV/ $c$  along the  $z$ -axis using **RapidSim**, corresponding to the  $\gamma\beta = 0.28$  boost of the centre-of-mass system in Belle II when operated at the  $\Upsilon(4S)$  resonance [80]. A perfect  $4\pi$  angular acceptance is assumed. It is not necessary to reweigh the Belle II momentum spectrum to account for the kaon-decay-time acceptance because all produced  $K_S^0$  mesons decay in the tracking volume.

The resulting momentum distributions for the three types of sample are shown in Fig. 3.4.

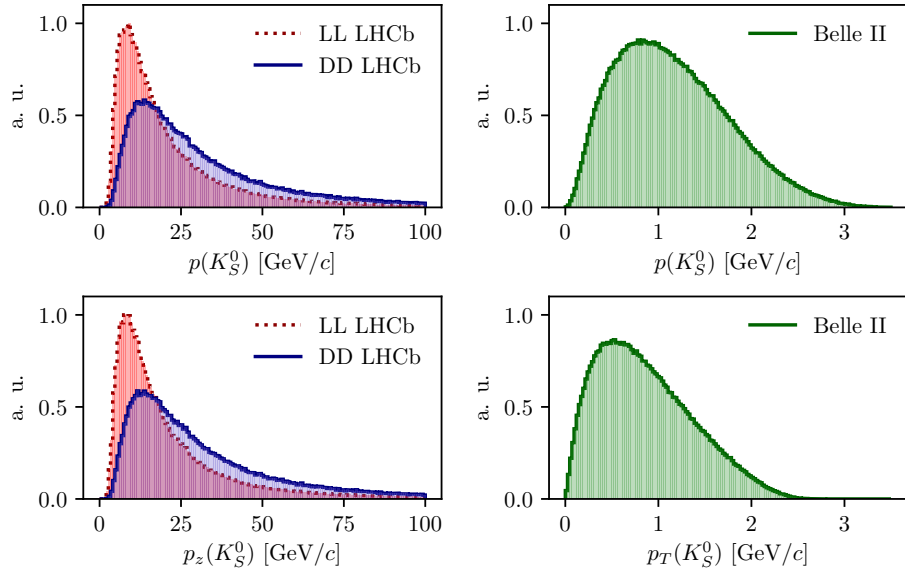


**Figure 3.4:** Momentum distributions for the LHCb (red dotted line) LL and (blue) DD categories, as well as (green) Belle II, obtained using `RapidSim`.

### 3.3.3 Experimental time acceptance

In order to model the experimental time acceptance, the time-dependent decay rates are only integrated over a finite time interval  $(\tau_1, \tau_2)$ . The intervals are defined for each of the three experimental categories, by requiring that a neutral kaon, if produced at  $x = y = z = 0$  with momentum  $p = (p_T, p_z)$ , decays within the relevant part of the corresponding detector. For the LL LHCb category, it is required that the kaon decays before reaching  $z_{max} = 280$  mm, corresponding to a decay where the decay products traverse at least 3 VELO segments (ignoring a number of widely spaced VELO segments placed at a distance of up to  $z = 750$  mm from the interaction point) [86]. For the DD LHCb category a decay at  $z \in [280, 2350]$  mm is required, corresponding to decay between the LL cut-off and the first downstream tracking station [87]. The time acceptance has a significant impact for the LHCb categories, where some 20 % of the kaons escape the tracking stations completely before decaying.

For Belle II, it is assumed that the  $K_S^0$  reconstruction is similar to the Belle  $K_S^0$  reconstruction, which is based on a neural network and reconstructs  $K_S^0$  decays for which the decay product leave tracks in both the drift chamber and silicon vertex detectors, as well as decays that leave tracks in the drift chamber only [88, 89]. Therefore, the  $K_S^0$  decay is required to be within  $r_{max} = 1130$  mm of the beam axis, corresponding to a decay within the outer radius of the drift-chamber. In practice,

most of the kaons decay inside the silicon vertex detector, and requiring a decay before 1130 mm is essentially equivalent to having no time cut-off.

### 3.3.4 Detector material budget

The effect of the material interaction is governed by parameter  $\Delta\chi$  of Eq. (3.16). The parameter varies along a given kaon path, as the kaon intersects detector components made of different materials. In these studies, the calculations are simplified by using a single average material parameter for each experimental scenario. The average material parameters can be estimated for a given experimental scenario by considering the type and length of material traversed by a kaon in the relevant sub-detector(s). The average value is estimated, by exploiting that  $\Delta\chi$  is related to the forward scattering amplitude  $f$  ( $\bar{f}$ ) of  $K^0$  ( $\bar{K}^0$ ) mesons in a given material [78,79]

$$\Delta\chi = -\frac{2\pi\mathcal{N}}{m_K}(f - \bar{f}) = -\frac{2\pi(N_A\rho/A)}{m_K}(f - \bar{f}), \quad (3.38)$$

where  $\mathcal{N} = N_A\rho/A$  is the scattering centre density of the material,  $m_K$  is the mass of the kaon state,  $A$  and  $\rho$  are the nucleon number and density of the material, and  $N_A$  is Avogadro's number. Measurements made for a range of nuclei [90] show that in the momentum range  $p_K \in [20, 140] \text{ GeV}/c$

$$\left| \frac{f - \bar{f}}{p_K} \right| = 2.23 \frac{A^{0.758}}{p_K^{0.614}(\text{GeV}/c)} \text{ mb}, \quad \arg[f - \bar{f}] = -\frac{\pi}{2}(2 - 0.614), \quad (3.39)$$

where the phase of  $\Delta f$  is determined via a phase-power relation [91]. In the numerical studies presented here, Eq. (3.39) is also used for the low momentum neutral kaons in the Belle II calculations, as a more detailed modelling of the low momentum  $\Delta\chi$  based on Ref. [92] is found to yield very similar results. The scattering centre density  $\mathcal{N}$  is approximated as being constant, equal to the average density along a neutral kaon path due to its intersection with different detector segments. This average is estimated using the simplifying assumption that the total detector material budget is due to silicon. In practice,  $\mathcal{N} = N_A\rho/A$  is calculated using  $A = 28$  and  $\rho = f^{\text{Si}}\rho^{\text{Si}}$ , where  $f^{\text{Si}} < 1$  is the average fraction of a neutral kaon path length that is inside detector material, estimated via the known dimensions of the detector, the average nuclear interaction length seen by a track traversing it cf. the technical design reports [86,93], and the nuclear interaction length of silicon  $\lambda_I^{\text{Si}} = 465.2 \text{ mm}$  [76]. The average value of  $r_\chi = \frac{1}{2}\frac{\Delta\chi}{\Delta\lambda}$ , which governs the size of the matter regeneration effect, can be calculated for the three considered experimental scenarios and satisfy  $|r_\chi^{\text{LL}}| = 2.7 \times 10^{-3}$ ,  $|r_\chi^{\text{DD}}| = 2.2 \times 10^{-3}$ , and  $|r_\chi^{\text{Belle II}}| = 1.0 \times 10^{-3}$ .

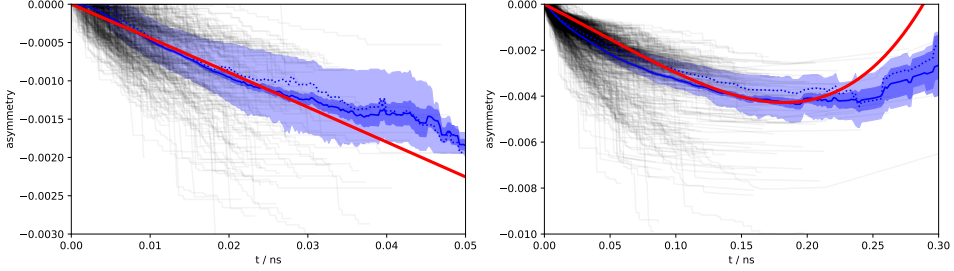


**Figure 3.5:** The asymmetry in Eq. (3.40) as a function of time for (left) LL and (right) DD  $K_S^0$  tracks in a simulated LHCb sample. The black lines show individual tracks. The light blue area is the central 50 % quantile, the dark blue area is the  $1\sigma$  uncertainty band on the mean. The red lines are calculated using the average  $\Delta\chi$  values that are also used in the calculation of biases in BPGGSZ measurements.

1083 The neutral kaon tracks in LHCb generally pass through somewhere between  
1084 zero (for a significant amount of the LL tracks) and a hundred (for some DD tracks)  
1085 distinct detector segments. Therefore it is worth examining the degree to which  
1086 using a single average  $\Delta\chi$  value, obtained following the procedure outlined above,  
1087 provides a reasonable description of the average material interaction. This can be  
1088 done using full LHCb simulation, where the kaon state for a simulated track can be  
1089 evaluated at all times, by applying Eq. (3.15) iteratively for each detector segment  
1090 the track traverses, using a  $\Delta\chi$  value appropriate for that segment. This is done  
1091 in Fig. 3.5 for a simple observable: the yield asymmetry

$$A_{K^0} = \frac{|\psi_{K^0}(t)|^2 - |\psi_{\bar{K}^0}(t)|^2}{|\psi_{K^0}(t)|^2 + |\psi_{\bar{K}^0}(t)|^2}, \quad (3.40)$$

1092 where  $\psi_{K^0}(t)$  ( $\psi_{\bar{K}^0}(t)$ ) is the amplitude for an initial  $K^0$  ( $\bar{K}^0$ ) to decay to two pions at  
1093 time  $t$ . In this calculation, it is assumed that  $\epsilon = 0$  to isolate the material effect with  
1094 no asymmetry contribution from the inherent  $CP$ -violation in the neutral kaon sector.  
1095 While the track-by-track asymmetries are found to differ significantly depending on  
1096 the exact detector segments a track intersects, the average asymmetry is seen to  
1097 evolve smoothly as a function of decay time, and in reasonable agreement with the  
1098 asymmetry value that is calculated using the average  $\Delta\chi$  values estimated above.

1099 The LHCb detector is undergoing a significant upgrade prior to the start of  
1100 the LHC Run 3. However, the material budget and geometry of the relevant sub-  
1101 detectors will be similar to the sub-detectors used during Run 1 and 2 [94, 95].  
1102 Hence the results of this study will be valid for measurements during the upgrade  
1103 phases of LHCb, even though the detector parameters presented in this section  
1104 relate to the original LHCb detector.

**3.3.5 Calculation procedure**

The main idea in the bias study is to calculate the BPGBSZ bin yields including the full effect of neutral kaon  $CP$  violation and material, fit them using the default equations of Chapter 1, and obtain the bias  $\Delta\gamma = \gamma - \gamma^0$  due to the kaon effects not being considered in the parameter extraction. For the purpose of Ref. [2], a simple fit setup of a single  $B^\pm \rightarrow Dh^\pm$  mode is investigated, where the  $K_i$  parameters are determined in a control channel with the relevant experimental acceptance. This setup is modified in the study used to assign a systematic uncertainty on the LHCb measurement of Chapter 4, as described in Section 3.3.7 below.

In practice, the amplitude model for  $D^0 \rightarrow K_S^0 \pi^+ \pi^-$  decays in Ref. [51] is taken to represent the  $A_1(s_{+-})$  amplitude. Then  $A_2(s_{+-})$  is obtained as described in Section 3.2.2. In terms of  $A_1$  and  $A_2$ , the amplitudes  $A_{S(L)}^{(\bar{D})}(s_{+-})$  can be expressed and related via Eqs. (3.25) and (3.26), and the full signal decay amplitudes as a function of phase-space coordinates, time, and the material interaction parameter  $\Delta\chi$  can be calculated for a given set of input parameters  $(\gamma^0, r_B^0, \delta_B^0)$ . The squared decay amplitudes are then integrated over phase space and the kaon decay times to obtain the binned signal yield.

The signal yields depend on the momentum via the time-acceptance parameters  $\tau_1$  and  $\tau_2$ , and because the material interaction parameter  $\Delta\chi$  is momentum dependent. Therefore, the yields are averaged over the  $K_S^0$  momentum distributions of LHCb and Belle II.

The parameters  $x_\pm$  and  $y_\pm$  are determined by a maximum likelihood fit to the calculated yields, after which the fit result and covariance matrix are interpreted in terms of the physics parameters  $(\gamma, r_B, \delta_B)$  using another maximum likelihood fit [96]. In the fits, the  $K_i$  are obtained using the definition  $K_i = K_i^{\text{meas}} = (N_i^D + N_{-i}^{\bar{D}})/(\sum_j N_j^D + N_{-j}^{\bar{D}})$ , in terms of the expected yields  $N_i^D$  ( $N_i^{\bar{D}}$ ) of a flavour-tagged  $D^0$  ( $\bar{D}^0$ ) decays in bin  $i$  of the  $D$  decay phase space, calculated as described above for  $r_B^0 = 0$ . This corresponds to experimentally measuring the  $K_i$  in a control channel, and takes the effect of neutral kaon  $CP$  violation and material interaction on  $K_i$  measurements into account, as well the experimental time acceptance. The  $(c_i, s_i)$  are calculated using  $A_1(s_{+-})$  and the experimental time acceptance is taken into account in this calculation as well.

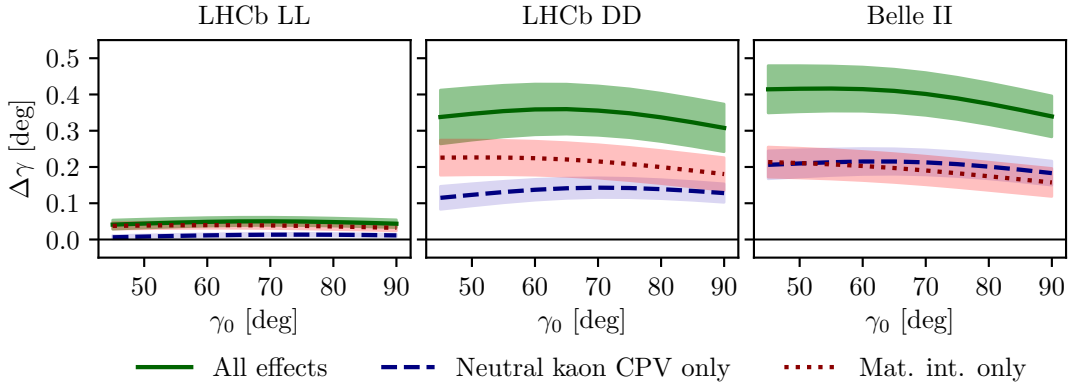


**Figure 3.6:** The bias  $\Delta\gamma$  as a function of input  $\gamma_0$  for (left) the LL LHCb category, (centre) the DD LHCb category, and (right) Belle II. The bias is calculated due to (blue, dashed line) neutral kaon  $CP$  violation alone, (red, dotted line) material interaction alone, and (green line) both effects. The shaded region shows the estimated  $1\sigma$  uncertainty band.

### 3.3.6 Results

The obtained bias  $\Delta\gamma$  is shown as a function of input  $\gamma^0$  for the various experimental conditions in Fig. 3.6. The calculations are made using  $(r_B^0, \delta_B^0) = (0.1, 130^\circ)$ , approximately equal to the physics parameters relevant for  $B^\pm \rightarrow DK^\pm$  decays [27, 39]. The bias does not vary significantly with  $\gamma^0$  in the plotted range, which includes the world average value of direct  $\gamma$  measurements as well as the values obtained in full unitarity-triangle fits [27, 38, 39], and for all cases, the bias is found to be below  $0.5^\circ$ , corresponding to relative biases of about half a percent. Thus the biases are of  $O(r\epsilon/r_B)$  as expected, given the arguments of Section 3.2.3. The contributions from the individual  $K_S^0$  CPV and material interaction effects are also shown. It is seen that the neutral kaon  $CP$  violation and material interaction effects leads to approximately equal biases in all three cases.

Given the decay-time acceptance and momentum distribution for each experimental category, the mean life time,  $\langle\tau\rangle$ , of the reconstructed kaons can be calculated. In terms of the  $K_S^0$  lifetime  $\tau_{K_S^0} = (0.895 \pm 0.004) \times 10^{-11}$  s [76],  $\langle\tau_{LL}\rangle \simeq 0.1\tau_{K_S^0}$  for the LHCb LL category,  $\langle\tau_{DD}\rangle \simeq 0.8\tau_{K_S^0}$  for the LHCb DD category, and at Belle II  $\langle\tau_{Belle\,II}\rangle \simeq \tau_{K_S^0}$ . The difference in average kaon lifetime is reflected in the observed biases, which are found to be larger in the samples with longer lived kaons. The very small effect in the LL category is to be expected because the  $CP$ -violation effect due to  $K_S^0$  not being  $CP$ -even is approximately cancelled by the  $CP$ -violation effect arising from  $K_S^0 - K_L^0$  interference for kaons with decay times much smaller than  $\tau_{K_S^0}$  [84].

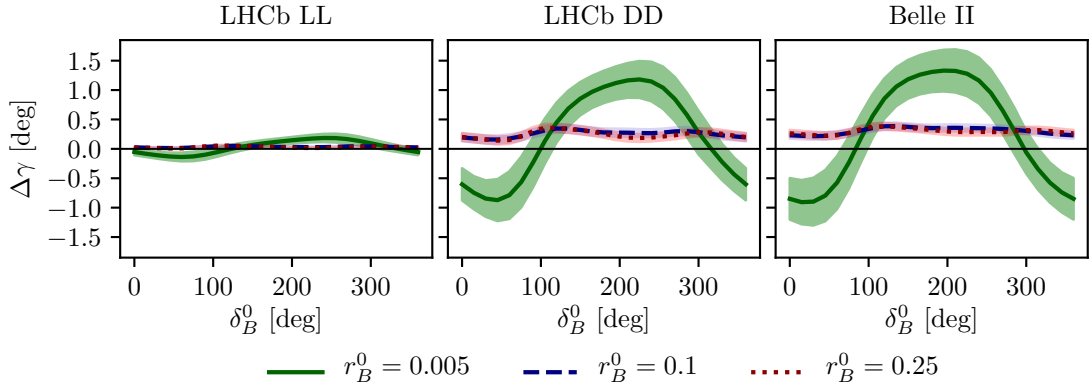


**Figure 3.7:** The bias  $\Delta\gamma$  as a function of input  $\delta_B$  for (left) the LL LHCb category, (centre) the DD LHCb category, and (right) Belle II. The bias is calculated for  $\gamma = 75^\circ$  and (green line)  $r_B = 0.005$ , (blue, dashed line)  $r_B = 0.1$ , and (red, dotted line)  $r_B = 0.25$ . The shaded region shows the estimated  $1\sigma$  uncertainty band.

1159     The uncertainty bands in Fig. 3.6 are calculated by repeating the study while  
1160     varying some of the inputs. The model dependence of the predicted biases is  
1161     probed by repeating the study using two other amplitude models as input for  
1162      $A_1(s_{+-})$  and  $A_2(s_{+-})$ : the model published in Ref. [61] and the model included in  
1163     EVTGEN [97]. When defining  $A_2(s_{+-})$  in terms of  $A_1(s_{+-})$ , there is an uncertainty  
1164     due to the unknown  $(r_k, \delta_k)$  parameters used to describe the  $\pi\pi$  resonance terms.  
1165     This uncertainty is assessed by making the study with several different random  
1166     realisations of the parameter set. The studies are repeated while varying the time  
1167     acceptances and material densities with  $\pm 10\%$ . There is an additional uncertainty  
1168     due to the use of simulation samples generated with `RapidSim` to describe the kaon  
1169     momentum distribution, in lieu of full detector simulations.

1170     There is also an uncertainty from the use of  $(c_i, s_i)$  as calculated using  $A_1(s_{+-})$ .  
1171     It is to be expected that the measured values  $(\hat{c}_i, \hat{s}_i)$  from the CLEO collaboration  
1172     differ by those calculated using  $A_1^D(s_-, s_+)$  by terms of  $O(\epsilon)$  due to neutral kaon  
1173      $CP$  violation, which is not taken into account in the measurement [69]. These  
1174     corrections can be calculated via a procedure analogous to the one used to estimate  
1175     the corrections on measurements of  $\gamma$  in this paper. However, as these corrections  
1176     are much smaller than the experimental uncertainties in the measurement, they  
1177     have not been studied further.

1178     For the purpose of this thesis, it is important to consider the bias in measurements  
1179     that use  $B^\pm \rightarrow D\pi^\pm$  decays as well, and other  $B$  decay modes can also be used in  
1180     BPFGSZ measurements, such as  $B^\pm \rightarrow D^*K^\pm$ ,  $B^\pm \rightarrow DK^{*\pm}$ , and  $B^0 \rightarrow DK^{*0}$ .  
1181     For the purpose of the study presented here, the main difference between the decay

channels is that they have different values of  $r_B$  and  $\delta_B$ . Figure 3.7 shows  $\Delta\gamma$  as a function of input  $\delta_B^0$ , for  $\gamma^0 = 75^\circ$  and three different values of  $r_B^0$ . Aside from  $r_B^0 = 0.1$ , the results are shown for  $r_B^0 = 0.005$ , which corresponds to the expectation in  $B^\pm \rightarrow D\pi^\pm$  decays [47] and  $r_B^0 = 0.25$ , which corresponds to  $B^0 \rightarrow DK^{*0}$  decays [96, 98]. The most notable feature is that the biases are significantly larger in the  $B^\pm \rightarrow D\pi^\pm$  case. This is expected: the  $r_B^0$  dependent behaviour is governed by the relative importance of different  $O(r\epsilon)$  correction terms to the phase-space distribution. There are terms of both  $O(r_A\epsilon)$  and  $O(r_B\epsilon)^3$ , which lead to expected biases of size  $O(r_A\epsilon/r_B)$  and  $O(r_B\epsilon/r_B) = O(\epsilon)$ , respectively, cf. the discussion of Section 3.2.3. In the  $B^\pm \rightarrow D\pi^\pm$  case, the  $O(r_A\epsilon)$  correction terms dominate because  $r_A/r_B \simeq (0.05/0.005) = 10$ . This explains the relatively large bias, as  $|r_A\epsilon/r_B^{D\pi}| \simeq 4\%$ . The bias is seen to be up to  $\pm 1.5^\circ$ , but only about  $+0.2^\circ$  with the expected value of  $\delta_B^{D\pi} \simeq 300^\circ$  [47, 96]. These biases are *much smaller* than the precision on  $\gamma$  that is obtainable in a  $B^\pm \rightarrow D\pi^\pm$  analysis with current experimental yields, and do thus not pose a problem. In the  $r_B^0 = 0.1$  and  $r_B^0 = 0.25$  cases the  $O(r_B\epsilon)$  correction terms dominate, and the biases are of  $O(\epsilon)$ , independent of the  $r_B^0$  value. Therefore both cases have biases of similar size.

Further, it is clear that the biases depend on  $\delta_B^0$  and that the oscillation period of the  $\delta_B$  dependence is different between the  $r_B^0 = 0.005$  case and the  $r_B^0 \in \{0.1, 0.25\}$  cases. It is to be expected that  $\Delta\gamma$  oscillates as a function of  $\delta_B^0$ , because  $\delta_B^0$  enters the yield equations via  $\cos(\delta_B^0 \pm \gamma)$  and  $\sin(\delta_B^0 \pm \gamma)$  terms. As explained above, the  $O(r_A\epsilon)$  terms dominate the  $B^\pm \rightarrow D\pi^\pm$  bias, and these are independent of  $\delta_B^0$ . The  $O(r_B\epsilon)$  terms, however, are important for the bias corrections for larger  $r_B$  values, and the terms include factors of  $\cos(\delta_B^0 \pm \gamma)$  and  $\sin(\delta_B^0 \pm \gamma)$ . This explains the different bias dependence on  $\delta_B^0$ .

While the input value of  $\gamma^0 = 75^\circ$  was chosen for these studies, there is minimal variation in the results if another value of  $\gamma^0$  in the range  $[60^\circ, 85^\circ]$  is used.

### 3.3.7 Coupled $B^\pm \rightarrow DK^\pm$ and $B^\pm \rightarrow D\pi^\pm$ measurements

The studies presented above have been extended on two accounts in order to assign a systematic uncertainty to the LHCb measurement presented in Chapter 4. Firstly, full LHCb simulation has been used to obtain the momentum distributions, as well as to fit a better description of the time acceptance and the reconstruction efficiency profile over the  $D$ -decay phase space. Secondly, the fit setup is modified

---

<sup>3</sup>There are similar terms of  $O(r_A r_\chi)$  and  $O(r_B r_\chi)$ , but as  $\epsilon$  and  $r_\chi$  are of the same order of magnitude, these terms can be treated completely analogously to the  $O(r_A\epsilon)$  and  $O(r_B\epsilon)$  terms, and have been left out of the discussion for brevity.

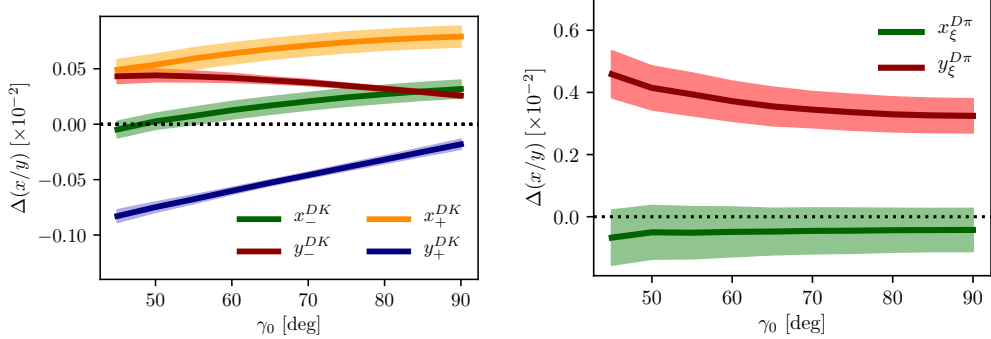


**Figure 3.8:** The bias on (left) the  $B^\pm \rightarrow DK^\pm$  and (right)  $B^\pm \rightarrow D\pi^\pm$   $CP$ -violation observables in the LHCb DD category, evaluated in bias studies with inputs based on full LHCb simulation, calculated as a function of input  $\gamma_0$ .

to correspond to the experimental approach described in Section 1.4 and Chapter 4: the signal yields are calculated for both the  $B^\pm \rightarrow DK^\pm$  and  $B^\pm \rightarrow D\pi^\pm$  channels, and fitted in a combined fit to obtain  $(x_\pm^{DK}, y_\pm^{DK}, x_\xi^{D\pi}, y_\xi^{D\pi})$ , where the  $F_i$  parameters are allowed to float in the fit. The biases obtained for each observable are shown in Fig. 3.8, evaluated using the time-acceptance, momentum distribution, and material budget relevant for the DD category (since the effect in the LL category is much smaller). As will be clear in Chapter 4, these biases are all significantly smaller than the corresponding statistical uncertainties. Thus, the effects of neutral kaon  $CP$  violation and material interactions contribute a manageable systematic uncertainty in current BPGGSZ measurements, even if the  $B^\pm \rightarrow D\pi^\pm$  channel is promoted to a signal channel.

As the statistical uncertainty becomes comparable with the bias effects described in this chapter, the systematic uncertainty should be assigned by a more accurate study, incorporating the traversed material on a track-by-track basis in full detector simulation. Such a detailed calculations can also be used to apply a bias correction if desired.

### 3.4 Concluding remarks

The analysis presented in this chapter has shown the expected impact of neutral kaon  $CP$  violation and material interaction on current BPGGSZ measurements to be small compared to the statistical uncertainties; first by simple order-of-magnitude estimates and then by a detailed calculation of the expected effect in LHCb and Belle II.

While the calculations were made for the case of  $D \rightarrow K_S^0 \pi^+ \pi^-$  decays, the BPGGSZ approach can of course also be applied in other  $D$ -decay final states,

such as  $D \rightarrow K_S^0 K^+ K^-$  and  $D \rightarrow K_S^0 \pi^+ \pi^- \pi^0$ . The biases on measurements of  $\gamma$  based the  $D$  decay phase-space distributions should be of similar size in these decay channels. The impact on  $\gamma$  measurements based on the phase-space-integrated yield asymmetry can be expected to be tens of degrees for the  $D \rightarrow K_S^0 K^+ K^-$  channel, where the yield asymmetry is expected to be around 2 %, for the reasons explained in Section 3.2.3. The  $D \rightarrow K_S^0 \pi^+ \pi^- \pi^0$  decay, however, is dominantly  $CP$ -odd [99], and the bias in measurements based on the total asymmetry is therefore expected to be  $O(\epsilon/r_B)$ , ie. a few degrees [74]. More precise calculations of the biases would require a repeat of the study included here, with relevant amplitude models and binning schemes in place.

The chapter focuses on the model-independent, binned approach that is the subject of the thesis. However, the underlying mechanism that determines the scale of the bias, namely that the phase-space *distribution* of signal decays is unaffected at  $\mathcal{O}(\epsilon)$  and  $\mathcal{O}(r_\chi)$ , is independent on the exact measurement approach. Therefore it is expected that amplitude-model-based measurements and measurements made with new unbinned methods such as those in Ref [68] will be similarly biased if kaon  $CP$  violation and regeneration are not accounted for.

# 4

1256

1257

## A BPGBGSZ measurement with $B^\pm \rightarrow Dh^\pm$ decays

1258

This chapter describes a model-independent BPGBGSZ measurement of  $\gamma$  with  $B^\pm \rightarrow DK^\pm$  and  $B^\pm \rightarrow D\pi^\pm$  decays where  $D \rightarrow K_S^0\pi^+\pi^-$  and  $D \rightarrow K_S^0K^+K^-$ , commonly denoted  $B^\pm \rightarrow D(\rightarrow K_S^0h^+h^-)h'^\pm$  decays. The measurement is made with the full LHCb data set collected during Run 1 and 2 of the LHC, corresponding to an integrated luminosity of about  $9\text{ fb}^{-1}$ . The analysis is under review for publication in the Journal of High Energy Physics at the time of writing [1] (one can hope).

1266

### 4.1 Candidate reconstruction and selection

1267

The  $B^\pm \rightarrow D(\rightarrow K_S^0h^+h^-)h'^\pm$  candidates are constructed during the offline *stripping* stage described in Section 2.3.3. The candidates are defined by first combining tracks to form a  $K_S^0 \rightarrow \pi^+\pi^-$  vertex, then a  $D \rightarrow K_S^0h^+h^-$  vertex, and finally the  $B^\pm \rightarrow Dh'^\pm$  candidate. Each final state track is required to satisfy certain momentum thresholds and track-quality requirements, and to be separated from all primary interaction vertices. Each decay vertex is required to satisfy a fit-quality threshold and to be separated from the primary vertex. Momentum thresholds are applied to the composite particles and they are required to have reconstructed invariant masses close to their known masses<sup>1</sup> except that the  $B$  candidate is required to have a reconstructed invariant mass in the interval  $4750\text{--}7000\text{ MeV}/c^2$ .

---

<sup>1</sup>The exact mass window depends on the particle type and reconstruction category; narrower mass windows are applied at a later stage, as described below.

1277 The  $B$  candidate is required to satisfy  $\chi^2_{\text{IP}} < 25$ , where  $\chi^2_{\text{IP}}$  is the difference in  $\chi^2$   
 1278 value of the primary vertex fit, when the vertex is formed with- and without the  $B$   
 1279 candidate. As the final *stripping* stage, a multivariate algorithm is applied to the  
 1280 formed  $B$  candidate to reduce the amount of random track combinations, denoted  
 1281 combinatorial background, even further than the aforementioned requirements.

1282 Two data categories are defined, depending the tracks used to form the  $K_S^0$   
 1283 candidate: the LL category where both pions are long tracks, and DD category where  
 1284 both pions are downstream tracks, using the track classifications of Section 2.2.

1285 Each candidate is re-analysed with the `DecayTreeFitter` (DTF) frame work [?],  
 1286 where a simultaneous fit of the full decay chain is made with a number of constraints  
 1287 applied: the momenta of the composite  $D$  and  $K_S^0$  particles are required to form  
 1288 invariant masses exactly equal to the known particle masses [76], and the momentum  
 1289 of the  $B$  candidate is required to point in the direction defined by the  $B$  decay  
 1290 vertex and the primary vertex. This refit results in improved resolution of the  
 1291 invariant masses of the composite particles and, very importantly, of the Dalitz  
 1292 coordinates in the  $D$ -decay phase space. It also ensures that all candidates fall in the  
 1293 kinematically allowed region of the  $D$ -decay phase space. Unless otherwise specified,  
 1294 all results in this chapter are based on the refitted track momenta; for reasons  
 1295 explained below, some studies have to be based on parameters that are obtained  
 1296 without the constraints described above, or with only a subset of them applied.

1297 Following the stripping stage, the further selection of signal candidates is  
 1298 performed in three steps: an initial set of requirements that remove a large fraction  
 1299 of candidates that are very likely to be background and veto a number of specific  
 1300 backgrounds, the application of a multivariate analysis algorithm designed to allow  
 1301 for filtering combinatorial background, and finally a set of particle-identification  
 1302 requirements. The requirements are summarised in Table 4.1, and each step is  
 1303 described in detail in the following sections.

### 1304 4.1.1 Initial requirements

1305 At the hardware trigger level, it is required that a particle associated with the signal  
 1306 decay triggered the hadronic level-0 trigger (Trigger on Signal, or TOS), or that  
 1307 the level-0 trigger decision was caused by a particle that is not associated with the  
 1308 signal decay (Trigger Independent of Signal, or TIS). The inclusion of the latter  
 1309 category increases the data sample about 50 %. At the software trigger level,

1310 Before any processing of the data, a loose preselection is applied to remove  
 1311 obvious background candidates. The reconstructed  $D$  ( $K_S^0$ ) mass is required to  
 1312 be within 25 (15) MeV/ $c^2$  of the known values [76]. The *companion* particle, the

**Table 4.1:** Summary of requirements applied to data. The base requirements are applied to all data samples before training or applying the BDT.

Base requirements		
Variable	Cut	Comment
Bachelor momentum, $p$	$< 100 \text{ GeV}/c$	
Bachelor has RICH	<i>true</i>	
$K^\pm$ in $D$ decay: momentum, $p$	$< 100 \text{ GeV}/c$	In $D \rightarrow K_S^0 K^+ K^-$
$K^\pm$ in $D$ decay: have RICH	<i>true</i>	In $D \rightarrow K_S^0 K^+ K^-$
DecayTreeFit converged	<i>true</i>	
$D$ mass	$m_{D^0} \in m_{D^0}^{PDG} \pm 25 \text{ MeV}/c^2$	From DTF with constrained $K_S^0$ mass
$K_S^0$ mass	$m_{K_S^0} \in m_{K_S^0}^{PDG} \pm 15 \text{ MeV}/c^2$	From DTF with constrained $D^0$ mass

Background suppressing requirements		
Variable	Cut	Comment
$K_S^0$ flight distance $\chi^2$	$> 49$	for LL only
$\Delta z_{\text{significance}}^{DB}$	$> 0.5$	for all candidates

PID requirements		
Channel	Cut	Comment
$B^\pm \rightarrow DK^\pm$	PIDK > 4	for bachelor
$B^\pm \rightarrow D\pi^\pm$	PIDK < 4	for bachelor
$B^\pm \rightarrow Dh^\pm$	IsMuon = 0	for bachelor
$B^\pm \rightarrow D(\rightarrow K_S^0 \pi^+ \pi^-)h^\pm$	PIDe < 0 & IsMuon = 0	for charged $D$ decay products
$B^\pm \rightarrow D(\rightarrow K_S^0 K^+ K^-)h^\pm$	PIDK > -5 & IsMuon = 0	for charged $D$ decay products

BDT requirements		
Channel	Cut	Comment
Run 1, DD	$> 0.6$	
Others	$> 0.8$	

1313 pion or kaon produced in the  $B^\pm \rightarrow Dh^\pm$  decay, is required to have associated  
1314 RICH information and a momentum less than  $100 \text{ GeV}/c$ ; this ensures good particle-  
1315 identification performance. Finally, all of the DTF fits of the full decay chain  
1316 are required to have converged properly.

1317 Two additional requirements are made at this stage in order to suppress specific  
1318 backgrounds. In order to suppress decays of the type  $B^\pm \rightarrow K_S^0 h^+ h^- h'^\pm$  with  
1319 no intermediate  $D$  meson, so called *charmless* decays, it is required that the  
1320 significance of the  $z$ -separation of the  $D^0$  decay vertex and the  $B^\pm$  decay vertex  
1321 is above 0.5. The significance of the  $z$ -separation of the  $D^0$  decay vertex and  
1322 the  $B^\pm$  decay vertex is defined as

$$\Delta z_{\text{significance}}^{D-B} = \frac{z_{vtx}^D - z_{vtx}^B}{\sqrt{\sigma^2(z_{vtx}^D) + \sigma^2(z_{vtx}^B)}}. \quad (4.1)$$

1323 This source of background described further in section 4.2.1. In order to suppress  
1324 a background from  $D \rightarrow 4\pi$  and  $D \rightarrow \pi\pi KK$  decays, it is required that the  $K_S^0$

1325 flight distance  $\chi_{\text{FD}}^2$  is greater than 49, where

$$\chi_{\text{FD}}^2 = \left( \frac{\Delta r}{\sigma(\Delta r)} \right)^2, \quad (4.2)$$

1326 and  $\Delta r$  is the measured flight distance of the  $K_S^0$  meson. This background is  
1327 described in further detail in section 4.2.2.

### 1328 4.1.2 Boosted decision tree

1329 A Gradient Boosted Decision Tree [100] (abbreviated BDT in the following) is  
1330 applied to classify each candidate on a scale from  $-1$  to  $+1$  as signal-like ( $+1$ )  
1331 or combinatorial-background-like ( $-1$ ), based on the values of a number of input  
1332 parameters for candidate in question. The BDT is implemented in the TMVA  
1333 frame work [101, 102].

1334 A boosted decision tree classifier consists of a number of sequentially trained  
1335 decision trees, each of which classify events as either signal or background. Each tree  
1336 bases the decision on an individual subset of variables, out of an overall set of input  
1337 variables. At each training step, the input events are weighted when training a new  
1338 tree, so that events that the already-trained trees classify incorrectly are given a  
1339 higher weight; this is denoted boosting. The term *gradient boosting* denotes a specific  
1340 weight calculation scheme [102]. The final score is the average over all decision trees.

1341 The full set of input variables are given in Table 4.2. It includes the momenta  
1342 of particles in the decay; a number of geometric parameters such a absolute and  
1343 relative vertex positions, and distances of closest approach between tracks;  $\chi_{\text{IP}}^2$   
1344 values for a number of particles in the decay chain; the  $\chi^2$  per degree of freedom  
1345 of the DTF refit; DIRA values, which denote the angle between the fitted particle  
1346 momenta and the vector spanned by it's production ad decay vertices; and finally  
1347 an isolation variable, defined as

$$A_{pt} = \frac{p_T(B) - \sum p_T(\text{other})}{p_T(B) + \sum p_T(\text{other})} \quad (4.3)$$

1348 where the sum is over all other tracks in a cone around the  $B$ -candidate. The cone  
1349 is defined as being within a circle with a radius of 1.5 units around the  $B$  candidate  
1350 in the  $(\eta, \phi_{\text{azim}})$ -plane. This variable is highly efficient in rejecting combinatorial  
1351 background. Two algorithms are trained, one for the LL category of  $K_S^0$  mesons and  
1352 one for the DD category, because some input parameters relate to the  $K_S^0$  meson  
1353 and have very different distributions between the two categories.

**Table 4.2:** Input parameter set used in BDTG trained to separate signal and combinatorial background, sorted according to importance in LL BDT.

Variable name	Importance LL/DD (Rank in DD)	Description
$\log(1-K_s_{DIRA\_BPV})$	7.2 % / 3.5 % (16)	$\log \cos \theta_{DIRA}$ for $K_S^0$
$\log(B_u_{RHO\_BPV})$	5.7 % / 5.5 % (5)	Radial distance of $B$ vertex to beam line
$\log(Bach\_PT)$	5.2 % / 6.9 % (1)	$p_T$ of the bachelor particle
$\log(1-D0_{DIRA\_BPV})$	4.9 % / 5.8 % (4)	$\log \cos \theta_{DIRA}$ for $D$
$\log(1-Bu_{DIRA\_BPV})$	4.9 % / 6.4 % (3)	$\log \cos \theta_{DIRA}$ for $B^\pm$
$\log(D0_{RHO\_BPV})$	4.8 % / 5.3 % (6)	Radial distance of $D$ vertex to beam line
$Bu\_PTASY\_1.5$	4.7 % / 4.9 % (7)	Asymmetry parameters of $B^\pm$
$\log(D0\_PT)$	4.7 % / 6.6 % (2)	$p_T$ of the $D$ meson
$\log(Bu_{constDOKSPV\_CHI2NDOF})$	4.2 % / 4.5 % (9)	$\chi^2/\text{d.o.f}$ of kinematical refit with DecayTreeFitter
$\log(Bu_{FDCHI2\_OWNPV})$	3.9 % / 4.1 % (11)	Flight distance $\chi^2$ of the $B^\pm$
$\log(\max_{Ksh1h2\_IPCHI2\_OWNPV})$	3.9 % / 3.0 % (20)	Largest $\chi^2_{IP}$ of the $K_S^0$ decay products
$\log(D0_{IPCHI2\_OWNPV})$	3.8 % / 3.3 % (17)	$\chi^2_{IP}$ of the $D$
$\log(\min_{Ksh1h2\_IPCHI2\_OWNPV})$	3.7 % / 0.9 % (26)	Smallest $\chi^2_{IP}$ of the $K_S^0$ decay products
$\log(Bu_P)$	3.7 % / 3.9 % (12)	$p$ of the $B^\pm$ meson
$\log(Bu_{IPCHI2\_OWNPV})$	3.6 % / 4.6 % (8)	$\chi^2_{IP}$ of the $B^\pm$
$Bu_{MAXDOCA}$	3.6 % / 3.3 % (18)	"Distance of closest approach" for $B^\pm$ vertex
$\log(Bach_{IPCHI2\_OWNPV})$	3.3 % / 4.3 % (10)	$\chi^2_{IP}$ of the bachelor particle
$\log(Bu_{PT})$	3.3 % / 3.7 % (14)	$p_T$ of the $B^\pm$ meson
$\log(\max_{h1h2\_IPCHI2\_OWNPV})$	3.1 % / 3.8 % (13)	Largest $\chi^2_{IP}$ of the $D$ decay products
$\log(\min_{h1h2\_IPCHI2\_OWNPV})$	3.0 % / 3.4 % (19)	Smallest $\chi^2_{IP}$ of the $D$ decay products
$\log(Ks_{VTXCHI2DOF})$	2.9 % / 2.3 % (21)	$\chi^2$ of vertex fit for $K_S^0$
$D0_{MAXDOCA}$	2.9 % / 1.0 % (25)	"Distance of closest approach" for $D$ vertex
$\log(D0_{VTXCHI2DOF})$	2.7 % / 1.6 % (24)	$\chi^2$ of vertex fit for $D$
$\log(D0_P)$	2.7 % / 1.8 % (22)	$p$ of the $D$ meson
$\log(Bach_P)$	2.2 % / 3.6 % (15)	$p$ of the bachelor particle
$\log(Bu_{VTXCHI2DOF})$	1.8 % / 1.7 % (23)	$\chi^2$ of vertex fit for $B^\pm$

1354        The BDTs are trained and tested with input samples representing typical signal  
 1355        and background decay candidates: a signal sample that consists of simulated  
 1356         $B^\pm \rightarrow D(\rightarrow K_S^0\pi^+\pi^-)\pi^\pm$  decays corresponding to the LHCb running conditions for  
 1357        the years 2012–2018, and a sample of combinatorial background candidates from  
 1358        real data, where the reconstructed invariant mass of the  $B$  meson is larger than  
 1359         $5800\text{ MeV}/c^2$ . The candidates in both samples were required to have passed the initial  
 1360        requirements described in the preceding section. The input-parameter distributions  
 1361        in the signal and background training samples are shown in Figs. 4.1 and 4.2. The  
 1362        signal and background samples are each split into two before the training stage: one  
 1363        sub sample, the training sample, is used to train the BDT, after which the trained  
 1364        algorithm is applied to the other sub sample, the test sample. The classifier is found  
 1365        to perform well on the test sample, not just the training sample, which ensures that  
 1366        it does not suffer significant overtraining. The BDT output distribution are shown  
 1367        for both test and training samples in Fig. 4.3, where it is clear that the classifier  
 1368        very effectively separates signal and background candidates.

1369        Each candidate in data is classified using the BDT, and candidates that are  
 1370        assigned a score below some threshold value are discarded. The threshold values  
 1371        are chosen in a set of pseudo experiments, such that the expected sensitivity to  $\gamma$  is  
 1372        maximised. This is done by performing preliminary fits to the data set for a range  
 1373        of different BDT threshold values, then generating many pseudo data sets with the  
 1374        obtained yields, and applying the full fit and interpretation procedure described in  
 1375        Sections 4.3–4.6 to each data set. Thus, the expected uncertainty on  $\gamma$  is obtained  
 1376        for for a range of threshold values. The procedure is applied independently for  
 1377        the LL and DD categories, as well as for the Run 1 and Run 2 data sets, because  
 1378        some parameter distributions differ slightly between the two runs. The optimal  
 1379        threshold values are found to be 0.8 in all situations, except for LL candidates  
 1380        in Run 1 where it is 0.6. This is illustrated in Fig. 4.4 where the results of the  
 1381        threshold scans are shown. The same classifier is applied to both  $B^\pm \rightarrow D\pi^\pm$  and  
 1382         $B^\pm \rightarrow DK^\pm$  candidates, and both  $D$  final state categories. While the classifiers were  
 1383        trained using samples of  $B^\pm \rightarrow D(\rightarrow K_S^0\pi^+\pi^-)\pi^\pm$  simulation and data, the decays  
 1384        are similar enough that no significant improvement in performance was obtained  
 1385        when considering a more elaborate setup. Across all categories, the requirement  
 1386        on the BDT output is found to remove approximately 98 % of the combinatorial  
 1387        background, while being approximately 93 % efficient on signal.

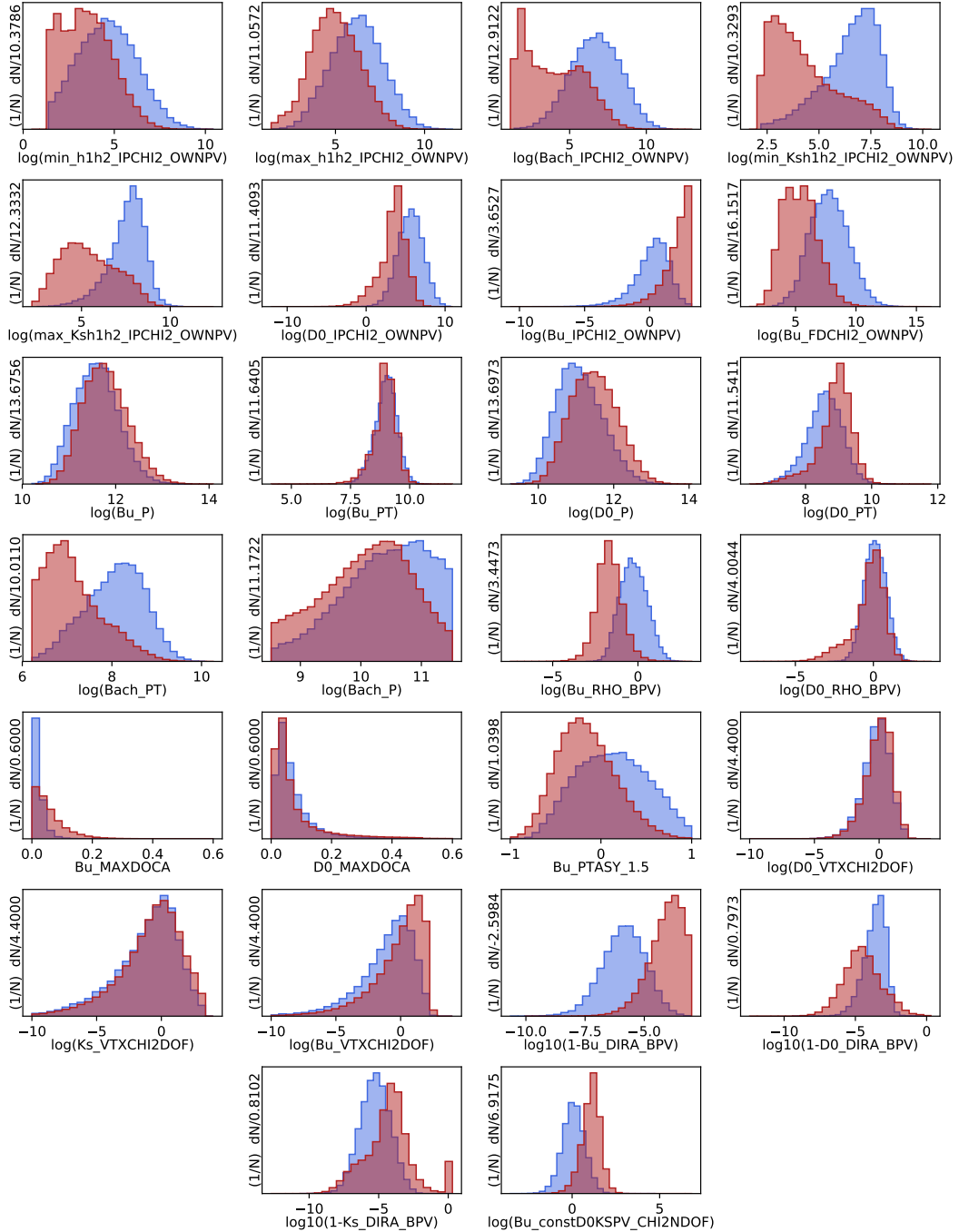


**Figure 4.1:** Distribution of input parameters in the LL training samples of (blue) signal decays from simulation and (red) background decays from the upper  $B$  sideband.

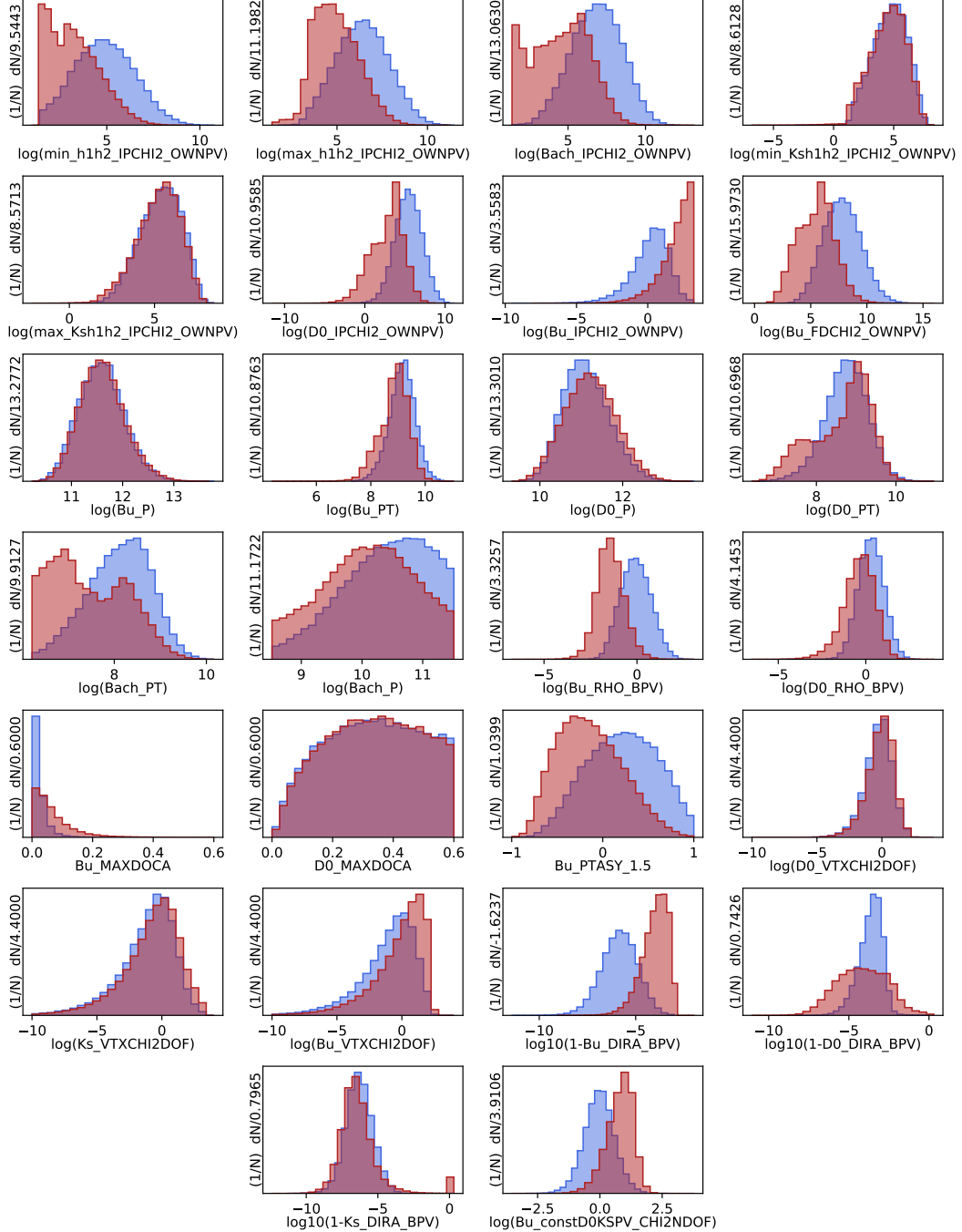


**Figure 4.2:** Distribution of input parameters in the DD training samples of (blue) signal decays from simulation and (red) background decays from the upper  $B$  sideband.

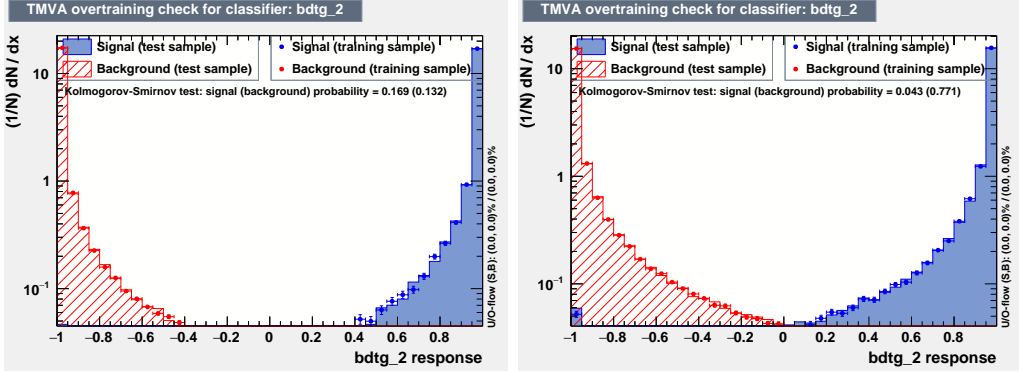


**Figure 4.3:** Distribution of BDT variable on test and training samples for (left) the LL and (right) the DD category, with logarithmic  $y$ -scale.

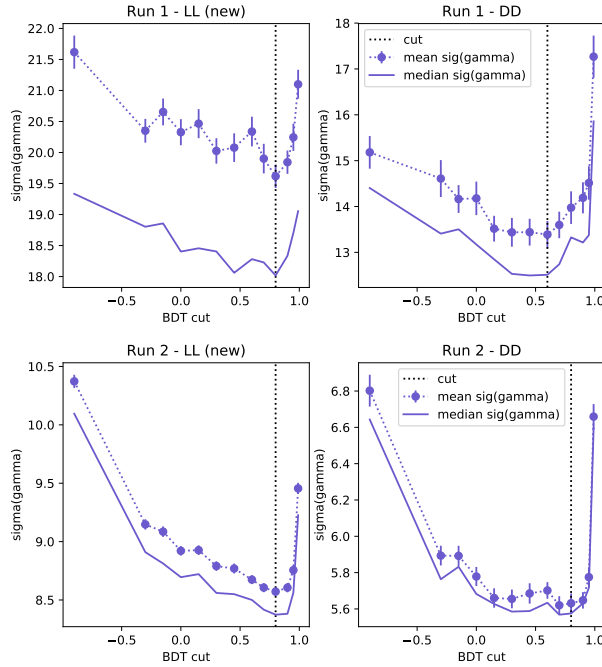


**Figure 4.4:** The mean uncertainty on  $\gamma$  in toy studies, performed with the signal and background yields corresponding to a given BDT requirement, using (top) the Run 1 and (bottom) Run 2 datasets, using only candidates in (left) the LL category and (right) the DD category. The median uncertainty across the toy studies is also shown.

### 1388 4.1.3 Particle-identification requirements

1389 A PID requirement is made to separate  $B^\pm \rightarrow DK^\pm$  and  $B^\pm \rightarrow D\pi^\pm$  candidates in  
 1390 the data sample, by requiring that the PIDK of the companion particle satisfies  
 1391  $\text{PIDK} < 4$  for  $B^\pm \rightarrow D\pi^\pm$  candidates and  $\text{PIDK} > 4$  for  $B^\pm \rightarrow DK^\pm$  candidates.  
 1392 The PIDK variable was defined in Section 2.1.3. This ensures that any given  
 1393 candidates is selected into only one of these samples.

1394 The efficiencies of the PID requirements on the companion enter the yield

**Table 4.3:** PID efficiencies obtained with the `PIDCalib` tool. The uncertainty incorporates statistical uncertainty due to the size of the reference sample, the systematic uncertainty due to the choice of binning scheme in `PIDCalib`, and a systematic uncertainty due to the `sWeight` calculation in `PIDCalib` of 0.1 %.

Efficiency	Particle	$D$ final state	$\varepsilon_{\text{PID}} (\%)$	
			LL	DD
Run I and II				
Correct ID	Kaon	$D \rightarrow K_S^0 \pi^+ \pi^-$	$86.74 \pm 0.13$	$86.90 \pm 0.22$
		$D \rightarrow K_S^0 K^+ K^-$	$86.22 \pm 0.26$	$86.56 \pm 0.30$
	Pion	$D \rightarrow K_S^0 \pi^+ \pi^-$	$97.11 \pm 0.11$	$97.17 \pm 0.13$
		$D \rightarrow K_S^0 K^+ K^-$	$97.07 \pm 0.11$	$97.16 \pm 0.14$

parameterisations of the mass fits in Section 4.3 and 4.4 and must therefore be known. They are determined using samples of calibration data selected without relying on PID variables, as implemented in the `PIDCalib` frame work [103]. Reasonably pure samples of pion and kaon tracks are obtained from  $D^0 \rightarrow K^- \pi^+$  decays, where the  $D$  meson originates in a  $D^{*+} \rightarrow D^0 \pi^+$  decay and can therefore be flavour tagged. The remaining background is subtracted via the *sPlot* [?] procedure, based on a two-dimensional fit of the  $m(K^- \pi^+)$  and  $m(D^0 \pi^+) - m(D^0)$  distributions. The obtained weights are employed to calculate the average efficiency of the requirement on PIDK for a number of bins in the momentum and pseudorapidity of the calibration tracks, and the number of charged tracks in the detector, thus constructing a three-dimensional efficiency lookup table. The procedure is carried out for each PID requirement, companion species, data-taking year, track charge, and magnet polarity. Based on these tables, expected PID efficiencies for the  $B^\pm \rightarrow D\pi^\pm$  and  $B^\pm \rightarrow DK^\pm$  signal decays are calculated that take the kinematical distribution and detector occupancy in the BPGBSZ data samples into account, by using the high-purity sample of  $B^\pm \rightarrow D\pi^\pm$  candidates in the signal region as a reference. The dominating uncertainty on the efficiencies is statistical in nature, due to the finite size of the reference sample. In addition, systematic uncertainties are included due to the *sPlot* procedure, estimated at 0.1 % [103], and due to the choice of binning scheme, estimated by repeating the procedure using a number of alternative binning schemes. The final efficiency estimates are shown in Table 4.3, including all sources of uncertainty.

Further to the requirement on the companion, PID requirements are made to suppress semi-leptonic backgrounds as well as decays where a final state particle decays in flight, and a loose PID requirement is made in the  $D \rightarrow K_S^0 K^+ K^-$  channels where it leads to a higher signal purity:

**Table 4.4:** Final candidate yield in each data category after the full selection has been applied, including removing candidates outside the region  $m_B \in [5080, 5800] \text{ MeV}/c^2$ .

$B$ Decay	$D$ final state	$K_S^0$ type	Run 1	Run 2	Total
$B^\pm \rightarrow DK^\pm$	$K_S^0\pi^+\pi^-$	LL	2275	10525	12800
		DD	5097	23508	28605
	$K_S^0K^+K^-$	LL	383	1610	1993
		DD	772	3397	4169
$B^\pm \rightarrow D\pi^\pm$	$K_S^0\pi^+\pi^-$	LL	18209	90509	108718
		DD	40167	205807	245974
	$K_S^0K^+K^-$	LL	2879	13757	16636
		DD	6033	29790	35823

- the companion particle is required to satisfy `IsMuon = 0`.
- For the  $B \rightarrow D(\rightarrow K_S^0\pi^+\pi^-)h^\pm$  samples it is required that the charged pion track from the  $D$  decay with opposite charge to the companion satisfies  $\text{PIDe} < 0 \& \text{IsMuon} = 0$ , and for the other charged pion that `IsMuon = 0`.
- For the  $B \rightarrow D(\rightarrow K_S^0K^+K^-)h^\pm$  samples it is required that the charged kaon tracks from the  $D$  decay have RICH information, a momentum less than 100  $\text{GeV}/c$  and  $\text{PIDK} > -5 \& \text{IsMuon} = 0$ .

These backgrounds are described in Section 4.2.3.

#### 4.1.4 Final requirements

For a small fraction of candidates in the final sample, it is the case that two or more candidates originate in the same  $pp$  collision. In order to make sure that all candidates are completely independent, a single, arbitrary candidate from each  $pp$  collision is kept for these collisions, and the other candidates discarded. This requirement results in the removal of less than 0.7% of candidates in each data category.

Furthermore, the  $D$  mass used to define the binning schemes described in Ref. [69] differs slightly from the mass used in the DTF refit. Therefore a few of the decays are reconstructed with Dalitz coordinates outside the allowed kinematic region. Because this problem only concerns a handful of candidates, they are simply discarded.

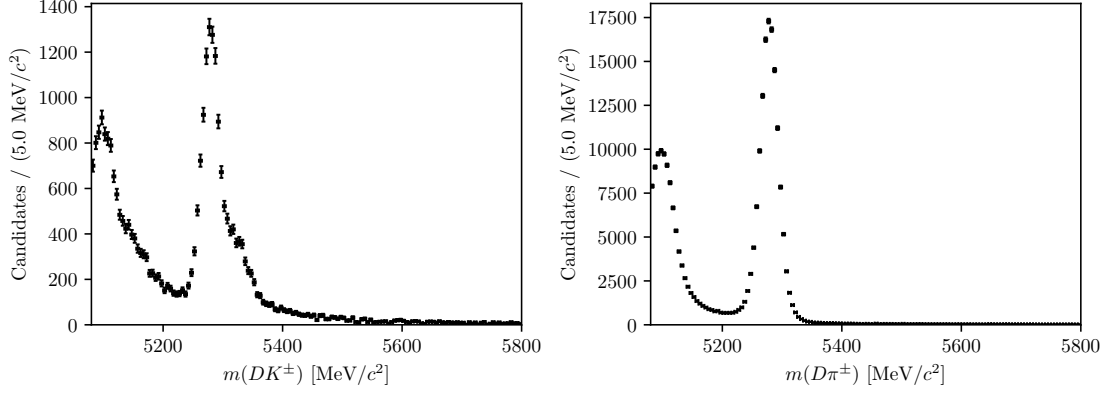


**Figure 4.5:** The spectrum of  $m_B$  in the (left)  $B^\pm \rightarrow DK^\pm$  and (right)  $B^\pm \rightarrow D\pi^\pm$  samples where  $D \rightarrow K_S^0\pi^+\pi^-$  and the  $K_S^0$  meson is reconstructed in the DD category, after the full selection has been applied.

#### 1440 4.1.5 Selected candidates

1441 In total, about 47,000  $B^\pm \rightarrow DK^\pm$  candidates and 400,000  $B^\pm \rightarrow D\pi^\pm$  candidates  
 1442 are selected, as summarised in Table 4.4. An example of the  $B$  mass distribution in  
 1443 one of the data categories is shown in Fig. 4.5; it is clear that a significant number  
 1444 of these candidates are background decays. The Dalitz plots for candidates in the  
 1445 signal region where  $m_B \in [5249, 5309] \text{ MeV}/c^2$  are shown in Fig. 4.6 and 4.7. Due to  
 1446 the large yields in the full Run 1 and 2 LHCb data set, the asymmetries between  
 1447 the  $B^+$  and  $B^-$  distributions are visible to the eye in the  $B^\pm \rightarrow DK^\pm$  plots.

## 1448 4.2 Background studies

1449 A wide range of backgrounds can potentially pollute the sample of signal candidates.  
 1450 The backgrounds group into three categories depending on how they are treated  
 1451 in the analysis:

- 1452 • Backgrounds that can be effectively removed in the selection
- 1453 • Backgrounds that are only present at a level where the impact on the  
 1454 measurement result is small, and which do therefore not have to be modelled
- 1455 • Backgrounds that are present at a level where they have to be modelled in  
 1456 the fit to data, and cannot effectively be rejected further in the selection

1457 The latter category comprises of combinatorial background, which remains present  
 1458 at a non-negligible level after the application of the BDT described in Section 4.1.2;  
 1459 contributions from a number of partly reconstructed  $B \rightarrow Dh^\pm X$  decays, where

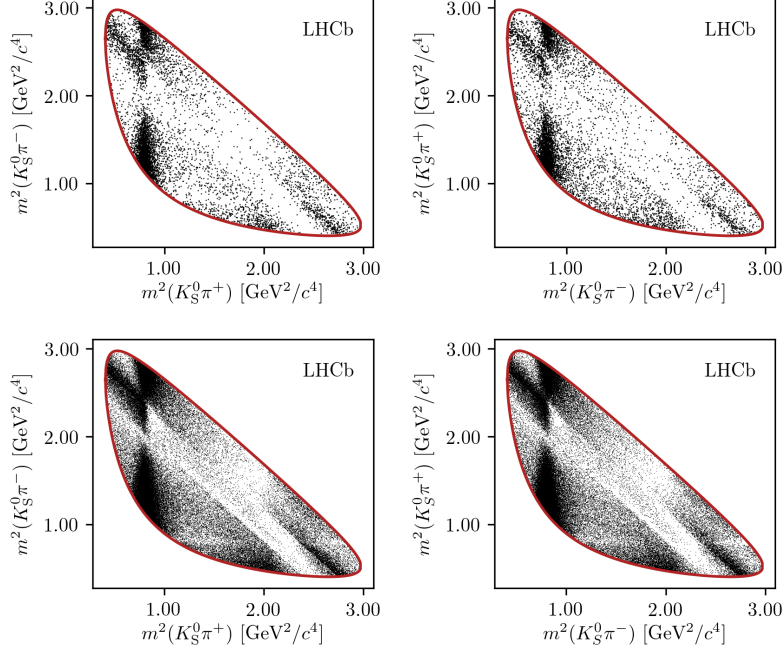


**Figure 4.6:** Dalitz plots of (left)  $B^+ \rightarrow Dh^+$  and (right)  $B^- \rightarrow Dh^-$  candidates in the signal region, in the (top)  $B^\pm \rightarrow DK^\pm$  and (bottom)  $B^\pm \rightarrow D\pi^\pm$  channels where  $D \rightarrow K_S^0 \pi^+ \pi^-$ . The LL and DD categories have been combined.

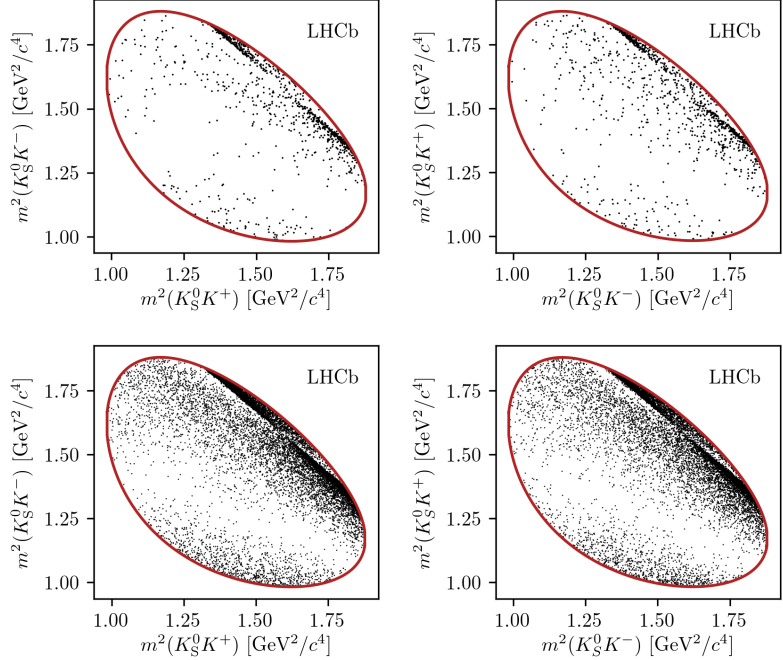


**Figure 4.7:** Dalitz plots of (left)  $B^+ \rightarrow Dh^+$  and (right)  $B^- \rightarrow Dh^-$  candidates in the signal region, in the (top)  $B^\pm \rightarrow DK^\pm$  and (bottom)  $B^\pm \rightarrow D\pi^\pm$  channels where  $D \rightarrow K_S^0 K^+ K^-$ . The LL and DD categories have been combined.

<sup>1460</sup>  $X$  denotes a pion or photon that is not included in the reconstructed decay, and  
<sup>1461</sup> which can only be separated from signal decays by their  $m(Dh)$  distribution; and  
<sup>1462</sup> finally  $B^\pm \rightarrow D\pi^\pm$  decays that are categorised as  $B^\pm \rightarrow DK^\pm$  decays in the particle-  
<sup>1463</sup> identification step and vice-versa. These background sources are described in detail  
<sup>1464</sup> in Section 4.3. This section focuses on backgrounds that led to specific requirements  
<sup>1465</sup> in the selection or proved to be small enough to not merit special treatment.

#### <sup>1466</sup> 4.2.1 Charmless decays

<sup>1467</sup> There is potentially a so-called *charmless* background present in data, consisting  
<sup>1468</sup> of  $B^\pm \rightarrow K_S^0 h^+ h^- h^\pm$  decays. These have the same final state as the signal decay,  
<sup>1469</sup> but no intermediate  $D$  meson. Because all final state particles are reconstructed,  
<sup>1470</sup> this background peaks in the  $B$  mass spectrum. This background is suppressed  
<sup>1471</sup> by requiring the reconstructed  $B$  and  $D$  decay vertices to be separated in the  
<sup>1472</sup>  $z$  direction; specifically by requiring that  $\Delta z_{\text{significance}}^{D-B} > 0.5$ , where  $\Delta z_{\text{significance}}^{D-B}$   
<sup>1473</sup> was defined in Eq. (4.1). The remaining background level can be investigated  
<sup>1474</sup> by investigating the  $D$  mass sidebands.

<sup>1475</sup> However, the use of the DecayTreeFitter  $\chi^2$  as an input variable in the BDT  
<sup>1476</sup> removes essentially all of the  $D$  (and  $K_S^0$ ) sideband, due to the mass constraints  
<sup>1477</sup> in the decay chain fit. Therefore separate BDT's are trained for LL and DD  
<sup>1478</sup> candidates without the  $\chi^2$  as an input variable, and used when selecting candidates  
<sup>1479</sup> for the background studies presented in this section, and the following. In a similar  
<sup>1480</sup> manner, all mass window requirements are made on the *default* reconstructed  
<sup>1481</sup> masses, obtained with no use of DecayTreeFitter. The overlap of the two sets of  
<sup>1482</sup> selected candidates in the signal  $B$ -mass window is above 95 %.

<sup>1483</sup> The reconstructed  $B$  mass spectrum is shown for  $B^\pm \rightarrow D\pi^\pm$  candidates in the  
<sup>1484</sup>  $D$  sidebands in Fig. 4.8, both before and after making a requirement on  $\Delta z_{\text{significance}}^{D-B}$ .  
<sup>1485</sup> A peak is clearly visible, the size of which is reduced by the requirement. This peak  
<sup>1486</sup> is partly due to a contribution from  $B^\pm \rightarrow K_S^0 \pi^+ \pi^- \pi^\pm$  decays ( $B^\pm \rightarrow K_S^0 K^+ K^- \pi^\pm$   
<sup>1487</sup> decays) in the  $D \rightarrow K_S^0 \pi^+ \pi^-$  ( $D \rightarrow K_S^0 K^+ K^-$ ) channel, and partly due to real  
<sup>1488</sup> signal decays that leak into the  $D$  sidebands. The number of real signal decays can  
<sup>1489</sup> be calculated from the yield obtained in the fit of Section 4.3, and the reconstructed  
<sup>1490</sup>  $m_D$  distribution in simulated signal decays. Subtracting this contribution, it is  
<sup>1491</sup> estimated that approximately 450 (200) charmless decays are present in the  $K_S^0 \pi^+ \pi^-$   
<sup>1492</sup> ( $K_S^0 K^+ K^-$ ) data samples. In similar fashion, Fig. 4.9 shows the  $m_B$  spectra for  
<sup>1493</sup>  $B^\pm \rightarrow DK^\pm$  candidates in the  $D$  sidebands. In these plots, the peaks are at  
<sup>1494</sup>  $m_B$  values that are lower (higher) than the  $B$  mass in the  $K_S^0 \pi^+ \pi^-$  ( $K_S^0 K^+ K^-$ )  
<sup>1495</sup> categories, because they stem from real  $B^\pm \rightarrow K_S^0 K^+ K^- \pi^\pm$  decays where a kaon is

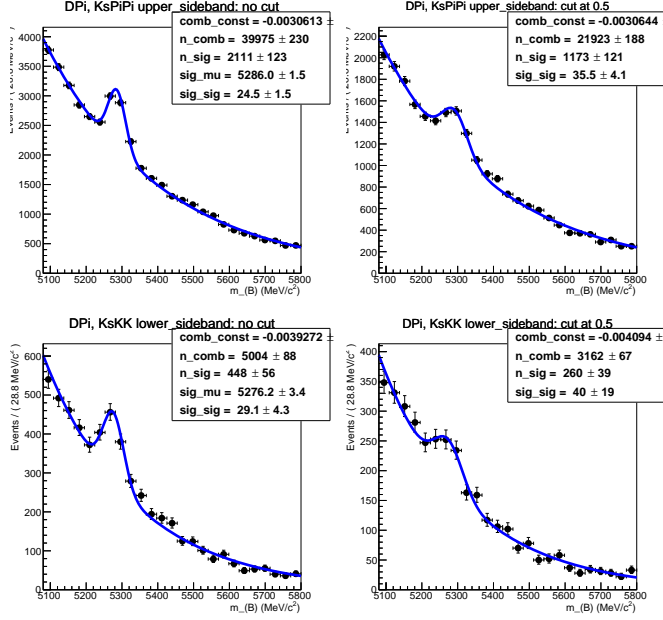


**Figure 4.8:** The  $B$  mass distribution of (top)  $B^\pm \rightarrow D(\rightarrow K_S^0 \pi^+ \pi^-) \pi^\pm$  and (bottom)  $B^\pm \rightarrow D(\rightarrow K_S^0 K^+ K^-) \pi^\pm$  candidates reconstructed in both the LL and DD categories, residing in the upper  $D$  mass sideband  $m_D \in [1910, 1960] \text{ MeV}/c^2$  for  $D \rightarrow K_S^0 \pi^+ \pi^-$  and in the lower sideband  $m_D \in [1910, 1960] \text{ MeV}/c^2$  for  $D \rightarrow K_S^0 K^+ K^-$ , with (left) no requirement on  $\Delta z_{\text{significance}}^{BD}$  and (right) after a requirement of  $\Delta z_{\text{significance}}^{BD} > 0.5$ .

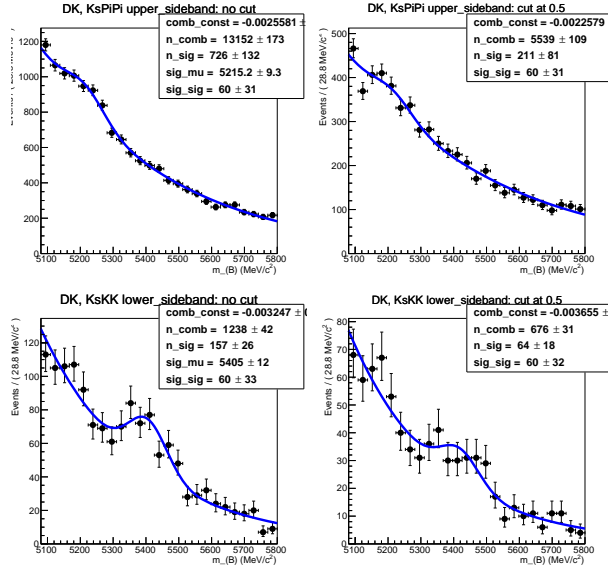


**Figure 4.9:** The  $B$  mass distribution of (top)  $B^\pm \rightarrow D(\rightarrow K_S^0 \pi^+ \pi^-) K^\pm$  and (bottom)  $B^\pm \rightarrow D(\rightarrow K_S^0 K^+ K^-) K^\pm$  candidates reconstructed in both the LL and DD categories, residing in the upper  $D$  mass sideband  $m_D \in [1910, 1960] \text{ MeV}/c^2$  for  $D \rightarrow K_S^0 \pi^+ \pi^-$  and in the lower sideband  $m_D \in [1910, 1960] \text{ MeV}/c^2$  for  $D \rightarrow K_S^0 K^+ K^-$ , with (left) no requirement on  $\Delta z_{\text{significance}}^{BD}$  and (right) after a requirement of  $\Delta z_{\text{significance}}^{BD} > 0.5$ .

1496 mis-reconstructed as a pion or a pion is misreconstructed as a kaon, respectively.  
1497 The total contribution of charmless decays in the  $B^\pm \rightarrow DK^\pm$  data samples is  
1498 estimated to be about 200 decays. As described further in Section 4.5.2, the  
1499 presence of a charmless background at these levels has a negligible impact on  
1500 the measurement results.

### 1501 4.2.2 Background from four-body $D$ decays

1502 A similar potential background is from real  $B^\pm \rightarrow Dh^\pm$  decays where the  $D$  meson  
1503 decays directly to the  $\pi^+\pi^-h^+h^-$  final state, without an intermediate  $K_S^0$  meson.  
1504 This background can be investigated by looking for a peak in the  $B$  mass spectrum  
1505 for candidates in the  $K_S^0$  sideband, as illustrated in Fig. 4.10. The figure shows  
1506 the spectrum in the final data sample, illustrating the significant effect of making  
1507 the requirement on the  $K_S^0$  flight distance that was discussed in Section 4.1.1. The  
1508 BDT that does *not* rely on the DTF  $\chi^2$  has been used to suppress combinatorial  
1509 background. The remaining peak after requiring  $\chi_{\text{FD}}^2 > 49$  is completely accounted  
1510 for by real signal decays that leak into the  $K_S^0$  sideband.

### 1511 4.2.3 Semi-leptonic backgrounds

1512 The data sample has a minor background from  $B \rightarrow D\mu\nu_\mu X$  decays, visible  
1513 in the  $B$  mass spectrum when the companion is required to satisfy `isMuon=1`.  
1514 This is shown in Fig. 4.11 for both the  $B^\pm \rightarrow DK^\pm$  and  $B^\pm \rightarrow D\pi^\pm$  channels  
1515 where  $D \rightarrow K_S^0\pi^+\pi^-$ . The  $B$  mass spectra for simulated  $B^\pm \rightarrow D\mu^\pm\nu_\mu$  decays  
1516 reconstructed in each category are also shown, from simulation samples produced via  
1517 RapidSim. The background is very efficiently vetoed by requiring `IsMuon=0` on the  
1518 companion. This requirement removes approximately 85 % of the background decays,  
1519 as estimated using the `PIDCalib` calibration samples and the  $(p, p_T)$  distribution  
1520 for the muon in the RapidSim samples. The fraction of signal candidates for  
1521 which the companion satisfies `IsMuon=1` in simulated signal samples is  $\leq 0.9\%$   
1522 so the impact on signal yield is small.

1523 The analogous  $B \rightarrow D e \nu_e X$  background is investigated by inspecting the  $B$   
1524 mass spectra after making requirements on `PIDE` for the companion candidate, but  
1525 a presence of the semi-leptonic background in data is not visible and no electron  
1526 veto is applied to the companion.

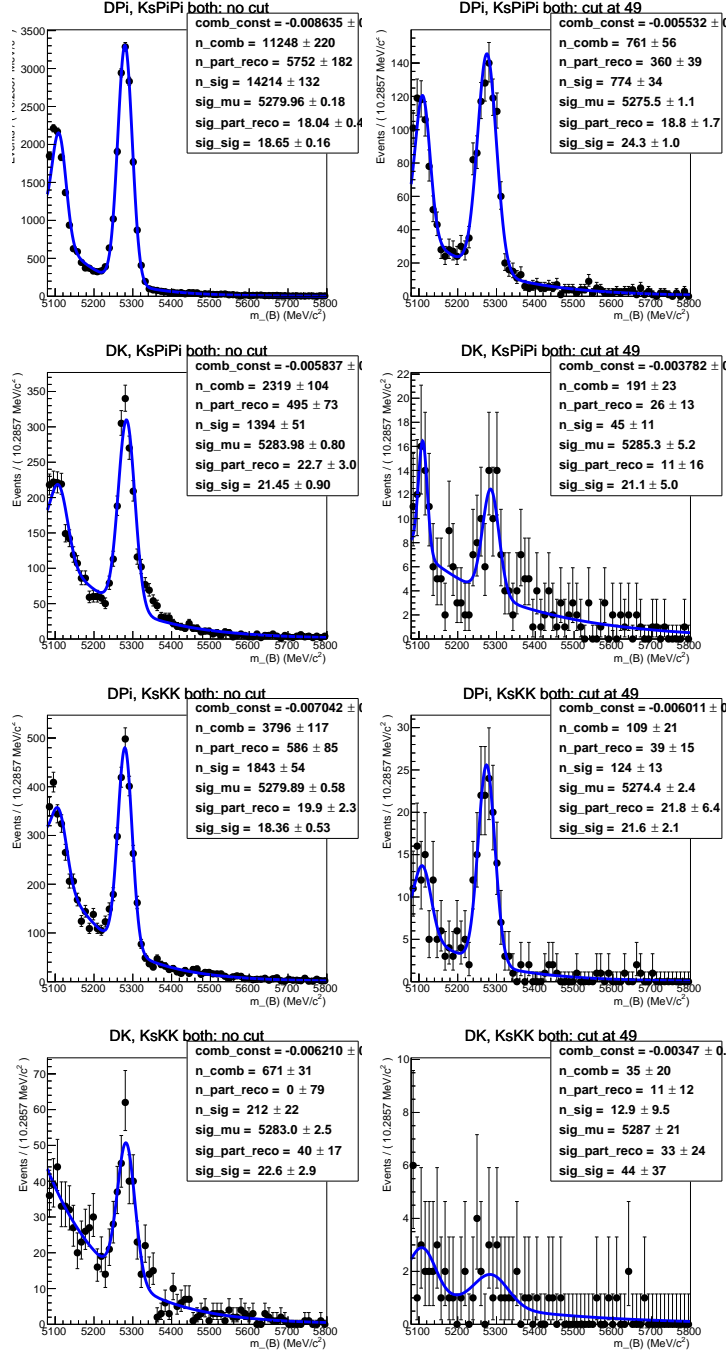


**Figure 4.10:** The  $B$  mass spectrum in the  $K_S^0$  sideband where  $m_{K_S^0} \in [467, 482] \text{ MeV}/c^2$  or  $m_{K_S^0} \in [512, 527] \text{ MeV}/c^2$  (left) without a requirement on the  $K_S^0$  flight distance significance, and (right) after the requirement implemented in the analysis.

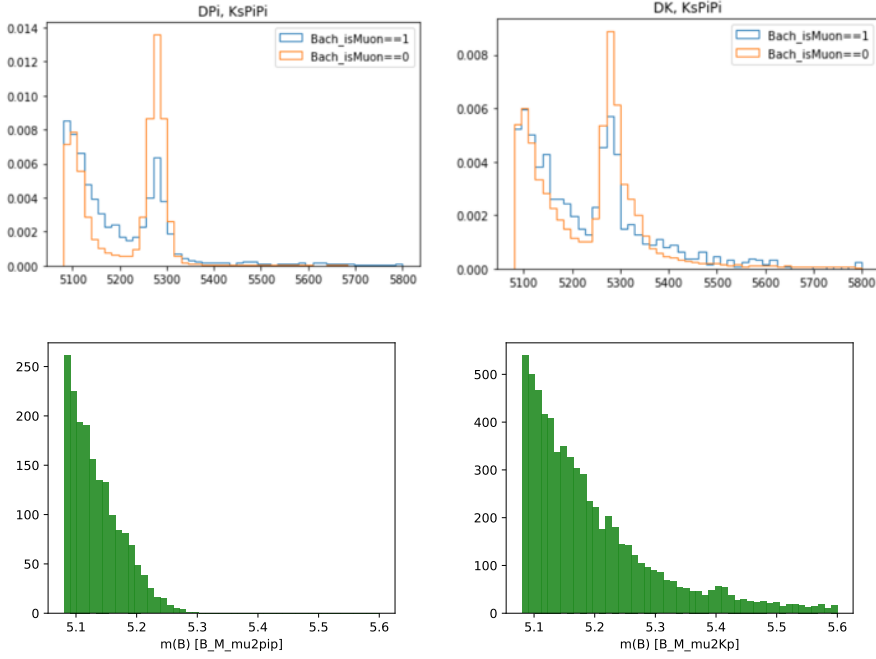


**Figure 4.11:** (Top) The  $m_B$  spectra in data split by the value of `Bach_isMuon` for (left) the  $D\pi^\pm$  and (right) the  $DK^\pm$  samples where  $D \rightarrow K_S^0\pi^+\pi^-$ . The two histograms are normalised independently, so that the distributions can be compared. The fractions candidates in data (with  $m_B \in [5080, 5800]$  MeV/c<sup>2</sup>) that satisfy `Bach_isMuon=1` are 1.6% and 1.8% for the  $D\pi^\pm$  and  $DK^\pm$  channels respectively. (Bottom) the RapidSim mass spectra for  $B^\pm \rightarrow D^0\mu^\pm\nu_\mu$  decays reconstructed in the (left)  $D\pi^\pm$  and (right)  $DK^\pm$  categories.

## 1527 Background from semi-leptonic D decays

1528 There is a potential background from real  $B^\pm \rightarrow Dh^\pm$  decays where the  $D$   
 1529 meson decays semi-leptonically:  $D^0 \rightarrow K_S^0\pi^-\ell^+\nu_\ell$ . This background is particularly  
 1530 dangerous because it peaks at the  $B$  mass, when the  $D$ -mass requirement is applied  
 1531 and it is reconstructed in the  $D \rightarrow K_S^0\pi^+\pi^-$  category. This is illustrated in Fig. 4.12  
 1532 using RapidSim samples of  $B^\pm \rightarrow D(\rightarrow K^{*-}(X)(\rightarrow K_S^0\pi^-)\ell^+\nu_\ell)h^\pm$  decays for  
 1533  $X = 892, 1430, 1680$ . The expected background yields relative to signal can be  
 1534 estimated by applying the  $B$  and  $D$  mass cuts to decays in the RapidSim samples,  
 1535 and using the relative branching ratios. Only the  $D^0 \rightarrow K^{*-}(892)\ell\nu_\ell$  branching  
 1536 fractions have been measured [76], but there is no reason to expect that higher  
 1537  $K^*$  resonances should not contribute. To estimate their potential contribution,  
 1538 the branching ratios are approximated by

$$\text{BR}[D^0 \rightarrow K^{*-}(X)(\rightarrow K_S^0\pi^-)\ell\nu_\ell] \simeq \frac{\text{BR}[D^0 \rightarrow K^{*-}(X)(\rightarrow K_S^0\pi^-)\pi^+]}{\text{BR}[D^0 \rightarrow K^{*-}(892)(\rightarrow K_S^0\pi^-)\pi^+]}\text{BR}[D^0 \rightarrow K^{*-}(892)(\rightarrow K_S^0\pi^-)\ell\nu_\ell]$$

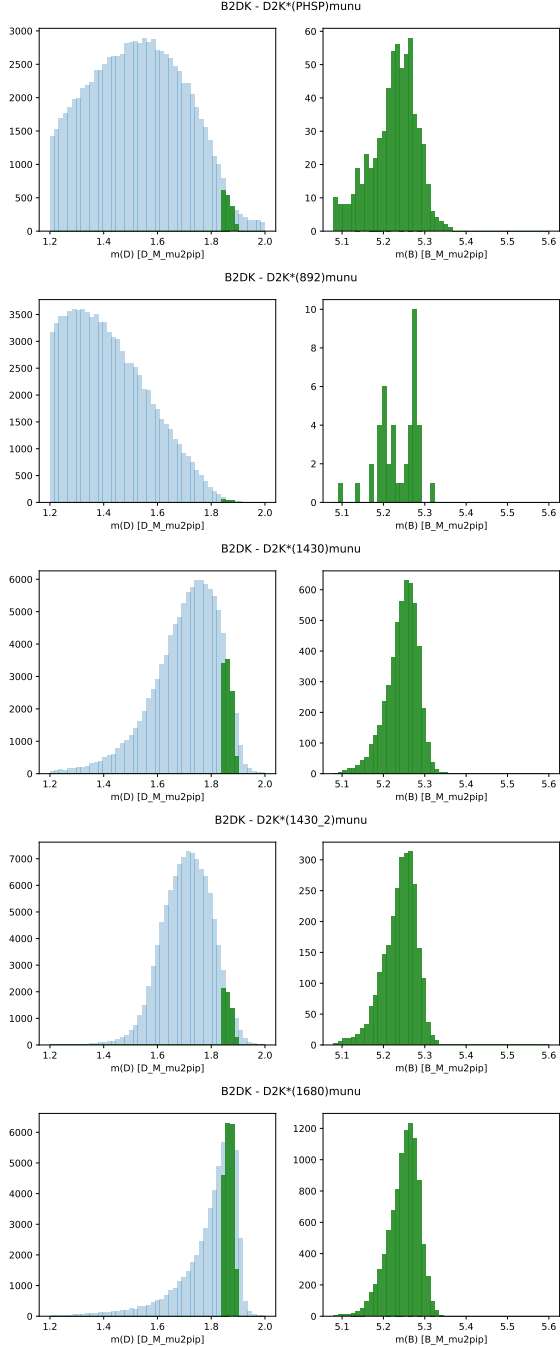


**Figure 4.12:** The reconstructed (left)  $m(K_S^0\pi^+\pi^-)$  and (right)  $m(Dh)$  distributions in RapidSim samples of  $B^\pm \rightarrow DK^\pm$  decays where  $D^0 \rightarrow K_S^0\pi^-\mu^+\nu_\mu$ . The top plot is for PHSP decays, and the following plots show the distribution where the  $K_S^0\pi^-$  originate in the resonances  $K^{*-}(892)$ ,  $K^{*-}_0(1430)$ ,  $K^{*-}_2(1430)$ , and  $K^{*-}(1680)$ . The shapes for the  $D^0 \rightarrow K_S^0\pi^-e^+\nu_e$  case are almost identical.

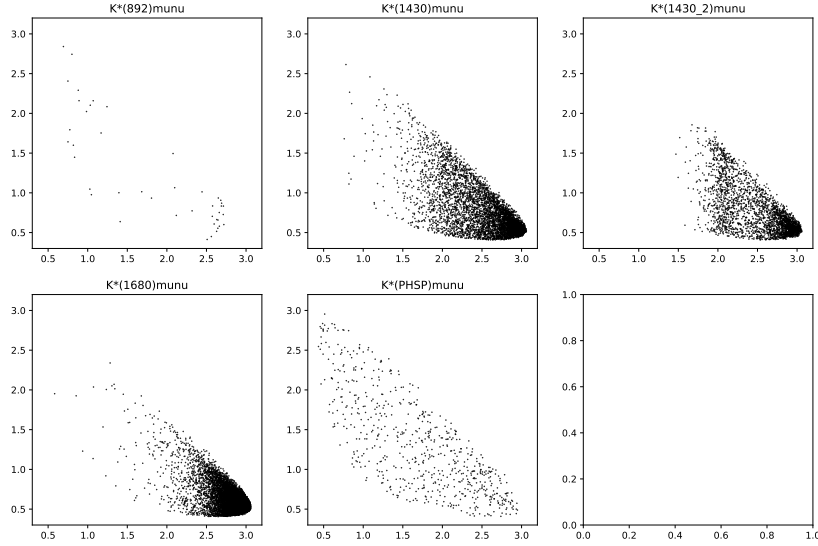


**Figure 4.13:** Dalitz distribution for  $D \rightarrow K_S^0 \pi^- \mu \nu_\mu$  decays in RapidSim, where the  $K_S^0 \pi^-$  originate in the resonances  $K^{*-}(892)$ ,  $K^{*-}_0(1430)$ ,  $K^{*-}_2(1430)$ , and  $K^{*-}(1680)$ , as well as for a flat PHSP distribution.

because all the relevant  $D^0 \rightarrow K^{*-}(\rightarrow K_S^0 \pi^-) \pi^+$  branching fractions are known [?].  
 The efficiencies and branching ratios relative to the signal channel are given in  
 Table 4.5. It is clear that the higher  $K^*$  resonances are important: the smaller  
 branching ratios are compensated for by a higher selection efficiency, due to the  
 smaller phase-space of the missed neutrino. The total background yield is 1.1 %  
 of the signal yield in both the  $B^\pm \rightarrow D\pi^\pm$  and  $B^\pm \rightarrow DK^\pm$  channels. However,  
 there will be an additional contribution in the  $B^\pm \rightarrow DK^\pm$  channel from real  
 $B^\pm \rightarrow D\pi^\pm$  decays with semi-leptonic  $D$  decays and a mis-identification of the  
 companion. This background also peaks, and the yield is approximately 0.4 %  
 of the  $B^\pm \rightarrow DK^\pm$  signal yield.

The potential impact from the presence of the background is estimated by

1. calculating the expected  $B^\pm \rightarrow D\pi^\pm$  and  $B^\pm \rightarrow DK^\pm$  yields in each bin for physics parameters similar to the world average values
2. then calculating the background bin yields in each bin, using the relative branching fractions and efficiencies described above and taking the bin-distribution from the RapidSim samples. The RapidSim samples are produced using the ISGW2 model in EvtGen [97], yielding the Dalitz distributions in Fig. 4.13.

**Table 4.5:** The selection efficiencies of  $B^\pm \rightarrow DK^\pm$  decays where  $D^0 \rightarrow K_S^0\pi^-\ell^+\nu_\ell$  when reconstructed in the  $D \rightarrow K_S^0\pi^+\pi^-$  mode in RapidSim relative to the signal selection efficiencies, for a number of decay modes: PHSP as well as resonant production where the  $K_S^0\pi^-$  pair originates in one of several  $K^*$  resonances. The relative branching ratios are also shown, calculated as explained in the main text, as well as the predicted relative yields.

Mode	$\epsilon_{bkg}/\epsilon_{signal}$ (%)	$\Gamma_{bkg}/\Gamma_{signal}$ (%)	$N_{bkg}/N_{signal}$ (%)
$D \rightarrow K_S^0\pi^-\mu^+\nu_\mu$ (PHSP)	$0.92 \pm 0.05$	$18.3 \pm 14.8$	$0.17 \pm 0.14$
$D \rightarrow (K_S^0\pi^-)_{K^{*-}(892)}\mu^+\nu_\mu$	$0.06 \pm 0.01$	$22.3 \pm 3.2$	$0.013 \pm 0.003$
$D \rightarrow (K_S^0\pi^-)_{K_0^{*-}(1430)}\mu^+\nu_\mu$	$7.3 \pm 0.1$	$3.7 \pm 0.8$	$0.27 \pm 0.06$
$D \rightarrow (K_S^0\pi^-)_{K_2^{*-}(1430)}\mu^+\nu_\mu$	$3.7 \pm 0.1$	$0.5 \pm 0.3$	$0.02 \pm 0.01$
$D \rightarrow (K_S^0\pi^-)_{K^{*-}(1680)}\mu^+\nu_\mu$	$24.4 \pm 0.3$	$0.6 \pm 0.5$	$0.15 \pm 0.12$
$D \rightarrow K_S^0\pi^-e^+\nu_e$ (PHSP)	$0.53 \pm 0.02$	$20.8 \pm 16.3$	$0.11 \pm 0.09$
$D \rightarrow (K_S^0\pi^-)_{K^{*-}(892)}e^+\nu_e$	$0.15 \pm 0.02$	$25.6 \pm 2.5$	$0.04 \pm 0.01$
$D \rightarrow (K_S^0\pi^-)_{K_0^{*-}(1430)}e^+\nu_e$	$6.3 \pm 0.1$	$4.2 \pm 0.8$	$0.26 \pm 0.05$
$D \rightarrow (K_S^0\pi^-)_{K_2^{*-}(1430)}e^+\nu_e$	$4.12 \pm 0.08$	$0.5 \pm 0.3$	$0.02 \pm 0.01$
$D \rightarrow (K_S^0\pi^-)_{K^{*-}(1680)}e^+\nu_e$	$10.0 \pm 0.2$	$0.7 \pm 0.5$	$0.07 \pm 0.05$
Total	-	-	$1.1 \pm 0.4$

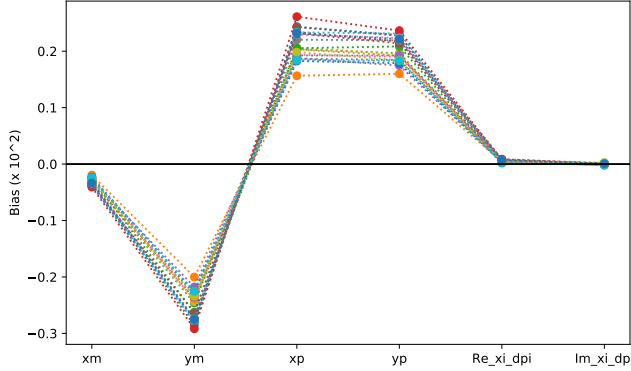


**Figure 4.14:** Estimated biases on the measured observables due to the presence of  $D \rightarrow K_S^0\pi\ell\nu_\ell$  backgrounds, calculated while varying efficiencies and branching ratios within uncertainties.

1557        3. adding the signal and background yields, and fitting the new  $B^\pm \rightarrow D\pi^\pm$  and  
 1558         $B^\pm \rightarrow DK^\pm$  yields back with the default signal-yield expressions (including a  
 1559        fit of the  $F_i$  parameters)

1560        The obtained biases are shown in Fig. 4.14, where they are calculated a number  
 1561        of times, each time varying the efficiencies within statistical uncertainties and the  
 1562        relevant branching fractions within the measurement uncertainties. The systematic

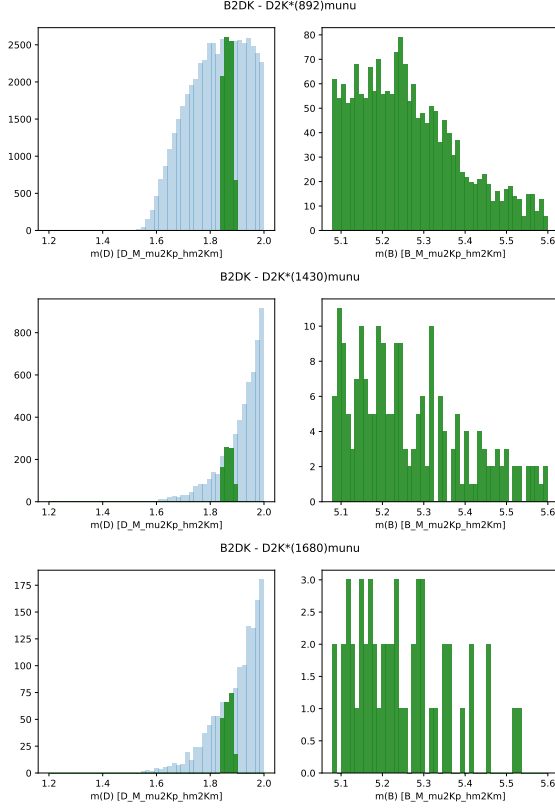


**Figure 4.15:** The reconstructed (left)  $m(K_S^0 K^+ K^-)$  and (right)  $m(Dh)$  distributions in RapidSim samples of  $B^\pm \rightarrow DK^\pm$  decays where  $D^0 \rightarrow K_S^0 \pi^- \mu^+ \nu_\mu$ , where the  $K_S^0 \pi^-$  originate in (top to bottom) the resonances  $K^{*-}(892)$ ,  $K^{*-}_0(1430)$ , and  $K^{*-}(1680)$ . The shapes for the  $D^0 \rightarrow K_S^0 \pi^- e^+ \nu_e$  case are almost identical.

uncertainty due to the unknown branching fractions and the use of RapidSim in lieu of full simulation is not included, but is of course significant. Nevertheless it is clear that the potential biases are significant compared to the size of the systematic uncertainties of the analysis presented in Section 4.5. Therefore the backgrounds are vetoed by requiring `IsMuon=0` and `PIDe < 0` on the pions from the  $D$ -decay with opposite charge to the bachelor in the  $D \rightarrow K_S^0 \pi^+ \pi^-$  channel. This requirement removes 88 % of the muonic background and 99 % of the electron background, according to PID efficiencies obtained via the `PIDCalib` package, using the  $(p, p_T)$  distribution for the muon/electron in the RapidSim samples. The survival rate for signal decays in full simulation is 94 %, so the impact on the obtainable precision is only about 3 %. A systematic uncertainty is assigned to account for the potential remaining background.

In the  $D \rightarrow K_S^0 K^+ K^-$  channel an analogous study shows the relative yields to be similar. The selection efficiencies are higher, as are the relative branching ratios due to the lower  $D \rightarrow K_S^0 K^+ K^-$  branching fraction, but in this mode the

1578 PIDK > -5 requirement placed on the pion and lepton remove approximately 90 %  
1579 of the background, leaving the relative rate similar to in  $D \rightarrow K_S^0\pi^+\pi^-$ . However,  
1580 importantly, *the background is not peaking*, as shown in Fig. 4.15. The presence  
1581 of a percent-level, *non-peaking* background in the  $D \rightarrow K_S^0K^+K^-$  channel is safe  
1582 to ignore and thus no veto is applied in the  $D \rightarrow K_S^0K^+K^-$  channel.

1583 The muon-veto for the semi-leptonic background does remove some signal  
1584 decays, where an original pion or kaon results in hits in the muon detectors. A  
1585 significant contribution is from particles that decay in flight. The track quality  
1586 of these decays is worse than for nominal decays, which affects the resolution on  
1587 the reconstructed Dalitz coordinates. In simulated signal decays the standard  
1588 deviation of  $\Delta m_\pm^2 = m_{reco}^2(K_S^0\pi^\pm) - m_{TRUE}^2(K_S^0\pi^\pm)$  is 50 % larger for decays where  
1589 one of the  $D$ -decay products has `IsMuon=1` than in decays where this is not the  
1590 case. This can lead to systematic biases on the observables, as described further in  
1591 Section ???. The overall effect is small, as evidenced by the systematic uncertainty  
1592 described in that section; nevertheless this fact motivates removing decay-in-flight  
1593 decays of the  $D$ -decay products. Therefore it is also required that `IsMuon=0` for  
1594 the  $D$ -decay pion with the same charge as the companion in the  $D \rightarrow K_S^0\pi^+\pi^-$   
1595 channels, and on the  $D$ -decay kaons in the  $D \rightarrow K_S^0K^+K^-$  channels. This veto  
1596 removes about 2 % of signal candidates in simulation that survive the lepton vetoes  
1597 described in the previous sections.

#### 1598 4.2.4 Cross-feed from other $D \rightarrow K_S^0h^+h^-$ decays

1599 Misidentification of a  $D$  decay product can lead to background from cross-feed  
1600 between the  $B^\pm \rightarrow D(\rightarrow K_S^0\pi^+\pi^-)h^\pm$  and  $B^\pm \rightarrow D(\rightarrow K_S^0K^+K^-)h^\pm$  signal chan-  
1601 nels, or cross-feed from  $B^\pm \rightarrow D(\rightarrow K_S^0K\pi)h^\pm$  decays into either of the signal  
1602 channels. However, this background is very highly suppressed by the employed  
1603 requirement on the  $D$  mass. This is illustrated in Figs. 4.16 and 4.17, where  
1604 the  $D$  mass distribution in samples of simulated  $B^\pm \rightarrow D(\rightarrow K_S^0K\pi)K^\pm$  and  
1605  $B^\pm \rightarrow D(\rightarrow K_S^0K\pi)\pi^\pm$  decays are shown, when reconstructed as  $D \rightarrow K_S^0\pi^+\pi^-$  and  
1606  $D \rightarrow K_S^0K^+K^-$ , respectively. Essentially no decays that fall in the selected  $D$  mass  
1607 window survive the full selection. Therefore this background is not considered further.  
1608 Neither is the background due to cross-feed between  $B^\pm \rightarrow D(\rightarrow K_S^0\pi^+\pi^-)h^\pm$   
1609 and  $B^\pm \rightarrow D(\rightarrow K_S^0K^+K^-)h^\pm$ , since it involves two misidentified particles, and  
1610 therefore will result in reconstructed  $D$  masses even further away from the selected  
1611 mass window. A very loose PID requirement on the charged  $D$  decay products  
1612 is nonetheless included in the  $D \rightarrow K_S^0K^+K^-$  channel, because it helps reduce  
1613 the level of combinatorial background.

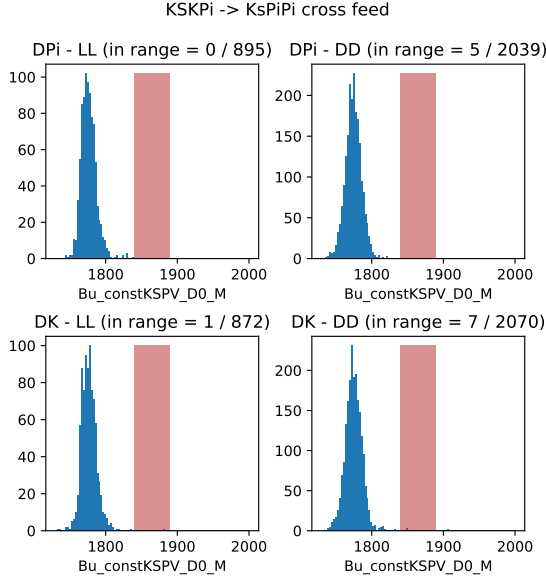


**Figure 4.16:** Simulated samples of (top)  $B^\pm \rightarrow D(\rightarrow K_S^0 K\pi)\pi^\pm$  and (bottom)  $B^\pm \rightarrow D(\rightarrow K_S^0 K\pi)K^\pm$  decays, reconstructed in the corresponding  $B^\pm \rightarrow D(\rightarrow K_S^0 \pi^+ \pi^-)h^\pm$  channel, for (left) the LL and (right) DD track-type categories. The  $D$ -mass region included in the selection of signal decays is illustrated with the red band.

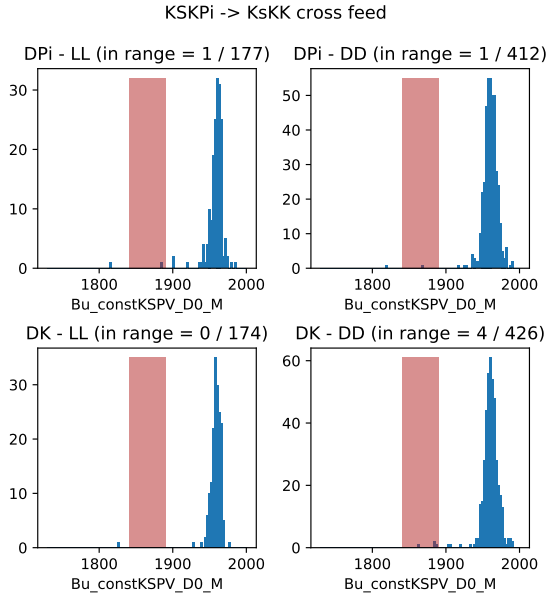


**Figure 4.17:** Simulated samples of (top)  $B^\pm \rightarrow D(\rightarrow K_S^0 K\pi)\pi^\pm$  and (bottom)  $B^\pm \rightarrow D(\rightarrow K_S^0 K\pi)K^\pm$  decays, reconstructed in the corresponding  $B^\pm \rightarrow D(\rightarrow K_S^0 K^+ K^-)h^\pm$  channel, for (left) the LL and (right) DD track-type categories. The  $D$ -mass region included in the selection of signal decays is illustrated with the red band.

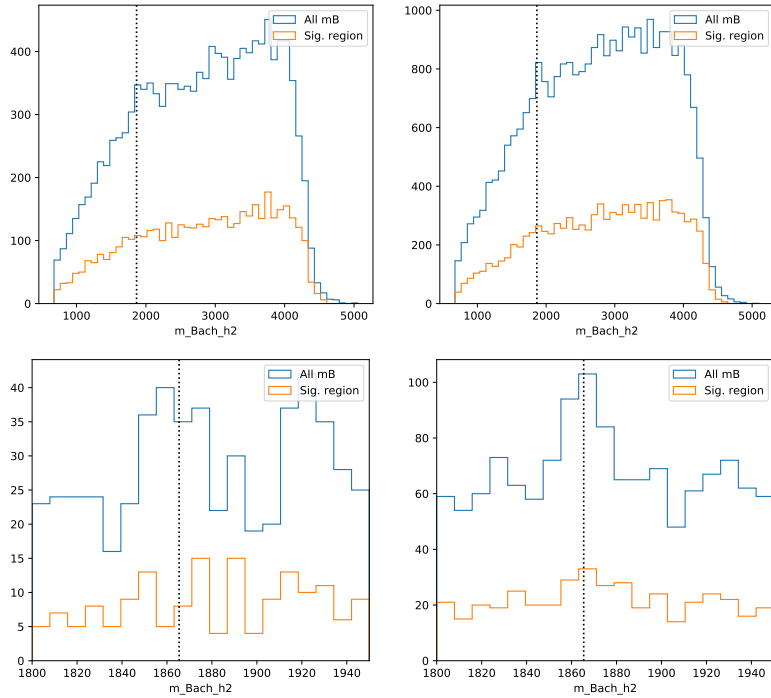


**Figure 4.18:** Invariant mass spectrum of the  $m^2(K^\pm\pi^\mp)$  combination in the  $B \rightarrow (K_S^0\pi^+\pi^-)K^\pm$  category for (blue) all candidate and (orange) candidates for which  $m_B \in m_B^{PDG} \pm 30 \text{ MeV}/c^2$ . The candidates are split into (left) the LL and (right) the DD candidates. The only difference between the top and bottom plots is the  $m(K\pi)$  mass range on the horizontal axis.

#### 1614 4.2.5 Swapped-track backgrounds

1615 A possible peaking background stems from real  $B \rightarrow DhX$  decays with the same  
 1616 final state tracks as in the signal case, but where some tracks are mis-assigned in the  
 1617 reconstruction. Examples are  $B^\pm \rightarrow (K_S^0 h'^+ h''^-)_D h^\pm$  decays where the companion  
 1618 and a  $D$ -decay product track are swapped, or  $B^\pm \rightarrow (K^\mp\pi^\pm)_D K_S^0 h^\pm$  decays, where  
 1619 the  $K_S^0$  is assigned to the  $D$  decay and the real companion is swapped with the  
 1620  $D$ -decay product of the same charge. The signature of this background type is  
 1621 a peak at the  $D$  mass, when the invariant mass corresponding to the companion  
 1622 track and some subset of the  $D$ -decay tracks is formed. The presence of the  
 1623 background has been investigated by forming all such combinations, for all data  
 1624 categories, after the full selection has been applied. Only in a single channel is a  
 1625 peak visible: the  $B^\pm \rightarrow (K_S^0\pi^+\pi^-)K^\pm$  channel, where  $m(K^\pm\pi^\pm)$  has a peak, as  
 1626 shown in Fig. 4.18. Thus, a background is present from the favoured two-body  
 1627  $D$  decay  $B^\pm \rightarrow (K^\pm\pi^\mp)_D K_S^0\pi^\pm$ , where the  $K^\mp$  is reconstructed as the companion,  
 1628 and the pions assigned to the  $D$  decay.

1629 Is is not favourable to veto this background, because a requirement on the  
 1630 invariant mass of a track combination that includes the companion track would

1631 impact the Dalitz-plot acceptance differently in the  $DK^\pm$  and  $D\pi^\pm$  channels. Thus  
 1632 it would break a fundamental underlying feature of the measurement: the identical  
 1633 selection efficiency profile between these modes. However, the yield excess in the  
 1634  $m(K^\pm_{Bach}\pi^\mp_D)$  range around  $m_D$ , attributed to the background, corresponds to  
 1635 only about 0.5 % of the signal yield. A background at this level does not lead to a  
 1636 limiting systematic uncertainty on the measurement, as described in Section ??.

### 1637 4.3 Signal and background mass shapes

1638 The measurement employs *extended maximum-likelihood fits* [?] to the  $m(Dh^\pm)$   
 1639 distribution of signal candidates to determine the observables of interest. The  
 1640 analysis implements a two-step fit procedure: first the data samples are analysed  
 1641 without separating the candidates by  $B$  charge or Dalitz bin, in order to determine  
 1642 appropriate parametrisations of the  $m(Dh^\pm)$  distribution of the signal and relevant  
 1643 background components. The parameterisations are then kept fixed in a subsequent  
 1644 fit of the observables of interest, where the candidates are split by  $B$  charge  
 1645 and Dalitz bin. This section describes the first step, whereas the latter fit is  
 1646 the subject of Section 4.4.

1647 In both steps, the candidates are split in 8 categories depending on whether  
 1648 the companion is categorised as a kaon or pion, whether the  $K_S^0$  meson is in the  
 1649 LL or DD category, and by whether the  $D$  meson is reconstructed in the  $K_S^0\pi^+\pi^-$   
 1650 or  $K_S^0K^+K^-$  final state. In the remained of this text, these categories are indexed  
 1651 with the letter  $c$ . For each category,  $c$ , the expected number of observed decays  
 1652 at a given  $B$  mass,  $F^c(m)$ , is given by the sum of a signal contribution and a  
 1653 number of background distributions

$$F^c(m|\theta) = N_s^c(\theta)f_s^c(m|\theta) + \sum_b N_b^c(\theta)f_b^c(m|\theta), \quad (4.4)$$

1654 where  $\theta$  denotes a set of parameters that describe the mass shapes and expected  
 1655 yields, in which some parameters are shared between categories. The distributions  
 1656  $f_{s/b}^c$  are normalised to integrate to unity, and the expected signal (background)  
 1657 yields are denoted  $N_s^c$  ( $N_b^c$ ). A total, normalised distribution can then be defined

$$f^c(m|\theta) = \frac{1}{N_{\text{tot}}^c(\theta)}F^c(m|\theta), \quad N_{\text{tot}}^c(\theta) = N_s^c(\theta) + \sum_b N_b^c(\theta). \quad (4.5)$$

1658 Given a set of  $N_{\text{observed}}^c$  measured  $B$  masses,  $\{m_i^c\}$ , in a given category, the extended  
 1659 log-likelihood function is defined

$$\ln \mathcal{L}_c(\theta|\{m_i^c\}) \equiv \sum_i \ln f^c(m_i^c|\theta) + \ln \text{Poisson}(N_{\text{tot}}^c(\theta), N_{\text{observed}}^c) \quad (4.6)$$

1660 In a simultaneous fit the total, negative log-likelihood is  $-\ln \mathcal{L} = -\sum_c \mathcal{L}_c$ , and  
1661 this function can be minimised to find the maximum-likelihood estimates of the  
1662 parameters in  $\theta$ , as well as their confidence regions and correlation coefficients.  
1663 This is handled with the `RooFit` package [104].

1664 Apart from signal decays, the fit includes components that describe combinatorial  
1665 background, backgrounds from decays where a companion pion is misidentified  
1666 as a kaon or vice versa, and partially reconstructed backgrounds. Each of these  
1667 components are described in detail in the following, before the results of the  
1668 first-stage fit are presented in Section 4.3.5.

### 1669 4.3.1 Signal decays

1670 The signal component is modelled with a sum of a Gaussian density function,  
1671  $f_G(m|m_B, \sigma)$ , and a modified Gaussian distribution with the parameterisation

$$f_C(m|m_B, \sigma, \alpha_L, \alpha_R, \beta) \propto \begin{cases} \exp\left[\frac{-\Delta m^2(1+\beta\Delta m^2)}{2\sigma^2+\alpha_L\Delta m^2}\right], & \Delta m = m - m_B < 0 \\ \exp\left[\frac{-\Delta m^2(1+\beta\Delta m^2)}{2\sigma^2+\alpha_R\Delta m^2}\right], & \Delta m = m - m_B > 0, \end{cases} \quad (4.7)$$

1672 which is Gaussian when  $\Delta m^2 \ll \sigma^2/\alpha_{L/R}$  or  $\Delta m^2 \gg \beta^{-1}$  (with widths of  $\sigma$  and  
1673  $\sqrt{\alpha_{L/R}/\beta}$  respectively), with an exponential-like transition that is able to model the  
1674 effect of the experimental resolution of LHCb very well. For the case  $\beta = 0$  the shape  
1675 is denoted the *Cruijff* shape; however, in this case it tends to a uniform distribution  
1676 for large  $\Delta m^2$  values, and cannot model the tails of the signal distribution well.  
1677 Thus, the full density function is

$$f_s(m|m_B, \sigma, \alpha_L, \alpha_R, \beta) = k_C f_C(m|m_B, \sigma, \alpha_L, \alpha_R, \beta) + (1 - k_C) f_G(m|m_B, \sigma). \quad (4.8)$$

1678 The tail parameters ( $\alpha_{L/R}, \beta$ ) and the constant  $k_C$  are determined in fits to simulated  
1679 signal decays that have passed the full selection. The parameters are shared  
1680 between the  $K_S^0\pi^+\pi^-$  and  $K_S^0K^+K^-$  channels, but otherwise independent in the  
1681 fit categories. An example of a fit to simulated  $B^\pm \rightarrow D(\rightarrow K_S^0\pi^+\pi^-)h^\pm$  decays  
1682 is given in Fig. 4.19. The resolution parameters  $\sigma$  are determined in the fit to  
1683 actual data. Separate parameters are determined in the LL and DD categories,  
1684 because the LL category has a better resolution on the  $K_S^0$  momentum, and  
1685 therefore a narrow peak in reconstructed  $B$  mass. Likewise, separate resolution  
1686 parameters are used for  $B^\pm \rightarrow D\pi^\pm$  and  $B^\pm \rightarrow DK^\pm$  decays, because the smaller  
1687  $Q$  value in the latter case leads to smaller momenta of the decay products, and  
1688 a correspondingly better resolution.

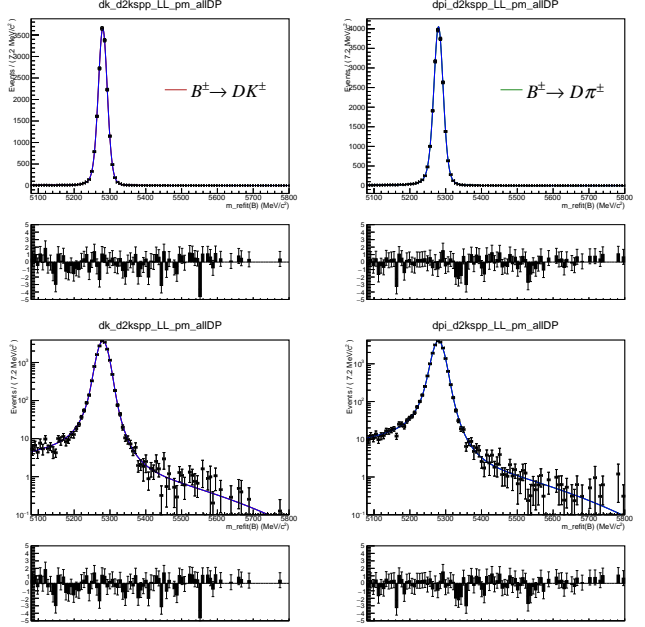


**Figure 4.19:** Fit projection of the signal shape to simulated  $B^\pm \rightarrow D(\rightarrow K_S^0 \pi^+ \pi^-) h^\pm$  samples reconstructed in the LL category. (Left) shows  $DK$  shapes, and (right) shows  $D\pi$  shapes. The shapes are shown with both linear and logarithmic  $y$ -axis scales.

The signal yields are determined independently in each  $B^\pm \rightarrow D\pi^\pm$  category. The yields in the  $B^\pm \rightarrow DK^\pm$  categories are then parameterised in terms of a single yield-ratio  $\mathcal{R}$ , and  $\epsilon^c$ , the corresponding selection efficiency for a given category

$$N_{DK^\pm}^c = \mathcal{R} \times N_{D\pi^\pm}^c \times \frac{\epsilon_{DK^\pm}^c}{\epsilon_{D\pi^\pm}^c}. \quad (4.9)$$

The selection efficiency is obtained in simulation, except for the PID efficiencies which are obtained in calibration data as described in Section 4.1.3. The parameter  $\mathcal{R}$  is shared between all categories, and corresponds to the branching ratio between  $B^\pm \rightarrow DK^\pm$  and  $B^\pm \rightarrow D\pi^\pm$  decays. Therefore, it can be compared to the branching ratio ratio measured in dedication measurements, which serves as an important cross check of the efficiency determination.

### 4.3.2 Cross-feed between $B^\pm \rightarrow Dh^\pm$ channels

There is a cross-feed between the  $B^\pm \rightarrow D\pi^\pm$  and  $B^\pm \rightarrow DK^\pm$  channels, where real  $B^\pm \rightarrow D\pi^\pm$  decays are reconstructed as  $B^\pm \rightarrow DK^\pm$  decays, or where  $B^\pm \rightarrow DK^\pm$  decays are reconstructed as  $B^\pm \rightarrow D\pi^\pm$  decays. Due to relative branching fractions the former contribution is by far the most important, but both are modelled.

The cross-feed shapes are obtained in a data-driven manner using the sPlot method [?], and fixed in the fit to data. Separate shapes are determined for each category, using the following steps:

- The procedure is based on the reasonably pure  $B^\pm \rightarrow D\pi^\pm$  sample obtained when the full selection is applied. A simple mass fit is performed to the invariant mass spectrum and the sPlot method [?] is used to obtain the sWeights,  $w_s$ , for the signal component. The mass fit uses the same components for signal, low mass shape, and combinatorial background as described in this section.
- A set of weights are defined, based on the candidate-by-candidate PID efficiencies obtained as described in Section 4.1.3:
  - The extracted PID efficiencies of the  $\text{PIDK} < 4$  cut  $\epsilon_{D\pi \rightarrow D\pi}(p, \eta, n_{\text{tracks}})$  are used to reverse-weight the  $B^\pm \rightarrow D\pi^\pm$  sample, in order to obtain the bachelor kinematic distributions before the  $\text{PIDK} < 4$  cut is applied.
  - The extracted PID efficiencies of the  $\text{PIDK} > 4$  cut  $\epsilon_{D\pi \rightarrow DK}(p, \eta, n_{\text{tracks}})$  are used to obtain the bachelor kinematic distribution of the  $B^\pm \rightarrow D\pi^\pm$  candidates mis-identified as  $B^\pm \rightarrow DK^\pm$ .
- The raw distribution of the invariant mass of  $B^\pm$  particles with a misidentified bachelor,  $m_B^{\text{mis-ID}}$ , is produced by also doing the DecayTreeFit kinematic refit while swapping the companion mass hypothesis of each  $B^\pm \rightarrow D\pi^\pm$  candidate to a kaon hypothesis.
- Each candidate is reweighted by the overall weight  $w = w_s^{\text{cand.}} / \epsilon_{D\pi \rightarrow D\pi}^{\text{cand.}} \cdot \epsilon_{D\pi \rightarrow DK}^{\text{cand.}}$ , and the reweighed  $m_B^{\text{mis-ID}}$  distribution is fitted to obtain the cross-feed mass distribution function.

The distributions are modelled with a sum of two Crystal Ball density functions, each defined by the parameterisation [105]

$$f_{\text{CB}}(m, \mu, \sigma, \alpha, n) \propto \begin{cases} \exp\left[-\frac{1}{2}\left(\frac{m-\mu}{\sigma}\right)^2\right] & \text{if } (m-\mu)/\sigma > -\alpha \\ A\left(B - \frac{m-\mu}{\sigma}\right)^{-n} & \text{otherwise,} \end{cases} \quad (4.10)$$

where  $\alpha > 0$ , and

$$A = \left(\frac{n}{\alpha}\right)^n \exp[-\alpha^2/2], \quad B = \frac{n}{\alpha} - \alpha. \quad (4.11)$$

The obtained  $m_B^{\text{mis-ID}}$  spectrum and obtained mass shape is given in Fig. 4.20 for the  $D \rightarrow K_S^0 \pi^+ \pi^-$  category; the  $D \rightarrow K_S^0 K^+ K^-$  shapes are very similar. An analogous procedure is used to obtain the mass distribution of  $B^\pm \rightarrow DK^\pm$  decays reconstructed in the  $B^\pm \rightarrow D\pi^\pm$  category. In the first stage where sPlots are

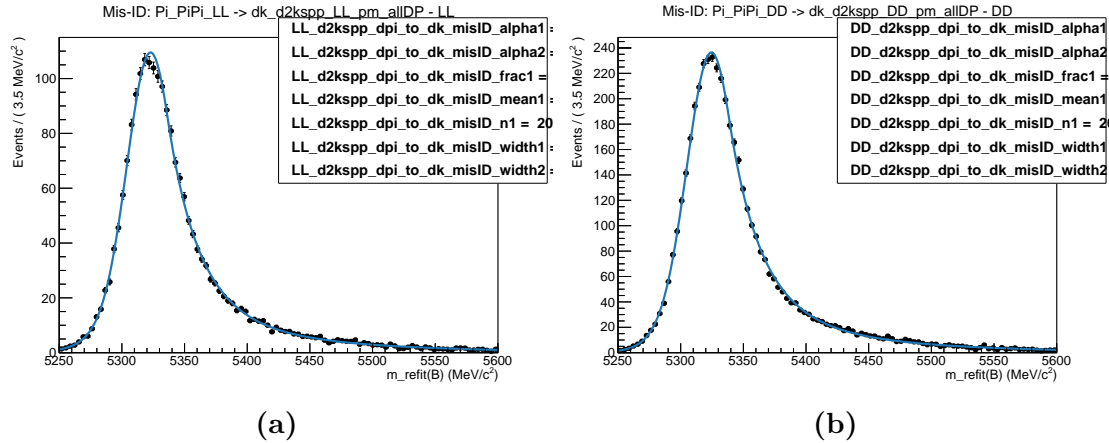


**Figure 4.20:** Fitted shape of  $B^\pm$  invariant mass spectrum for  $B^\pm \rightarrow D\pi^\pm$  events misidentified as  $B^\pm \rightarrow DK^\pm$  events for (a) LL and (b) DD candidates in the  $D \rightarrow K_S^0\pi^+\pi^-$  mode.

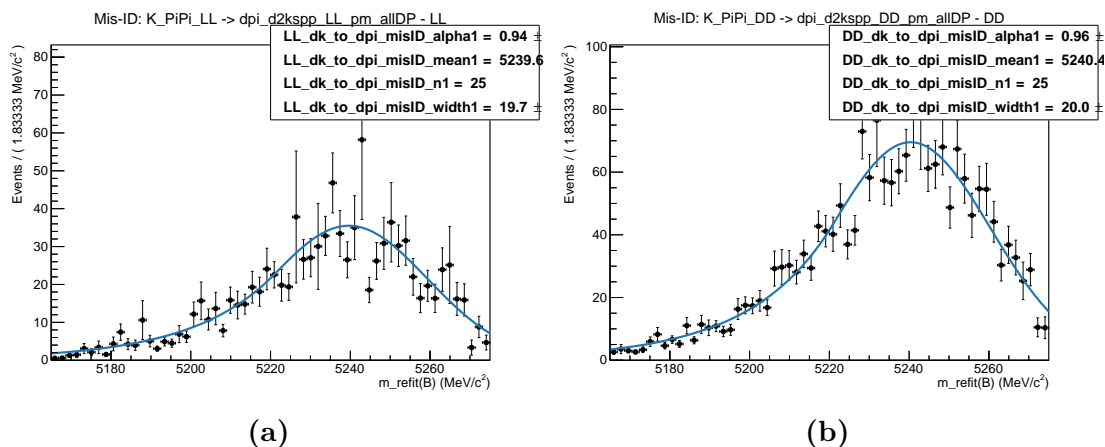


**Figure 4.21:** Fitted shape of  $B^\pm$  invariant mass spectrum for  $B^\pm \rightarrow DK^\pm$  events misidentified as  $B^\pm \rightarrow D\pi^\pm$  events for (a) LL and (b) DD candidates. The shape is obtained using  $D \rightarrow K_S^0\pi^+\pi^-$  decays, and used in the  $D \rightarrow K_S^0K^+K^-$  mode as well.

<sup>1734</sup> extracted by a fit to the  $B^\pm \rightarrow DK^\pm$  mass spectrum, the cross-feed component  
<sup>1735</sup> determined as described above is included. An example of one of the resulting  
<sup>1736</sup> shapes is given in Fig. 4.21

The yield of cross-feed from  $B^\pm \rightarrow D\pi^\pm$  decays in a given  $B^\pm \rightarrow DK^\pm$  category  
 is parameterised in terms of the yield of correctly identified  $B^\pm \rightarrow D\pi^\pm$  decays and  
 the mis-identification probability extracted from calibration samples as described  
 in Section 4.1.3. Denoting the rate at which a pion is reconstructed as a kaon  
 by  $\epsilon_{\pi \rightarrow K}^c$  in a given category,  $c$ , the yield is

$$N_{\pi \rightarrow K}^c = N_{D\pi^\pm}^c \frac{\epsilon_{\pi \rightarrow K}^c}{1 - \epsilon_{\pi \rightarrow K}^c}, \quad (4.12)$$

1742 with an analogous definition of the yield of the cross-feed component from  
1743  $B^\pm \rightarrow DK^\pm$  decays in the  $B^\pm \rightarrow D\pi^\pm$  spectrum.

### 1744 4.3.3 Partially reconstructed backgrounds

1745 A number of background candidates stem from partly reconstructed  $B$  decays of the  
1746 type  $B \rightarrow DhX$ , where  $X$  denotes a photon or a pion that is not reconstructed. It  
1747 is not possible to reject these decays in the selection, due to the similarity to signal  
1748 decays. However, the missing momentum results in reconstructed  $B$  masses below  
1749 the actual  $B$  mass, and the backgrounds are also denoted *lowmass* backgrounds.  
1750 These mass distributions are modelled with analytic shapes, derived based on two  
1751 principles. Firstly, the kinematic endpoints of the distributions are fully defined by  
1752 the particle masses in the decay. Secondly, the angular distribution of the missing  
1753 particle has a one-to-one relation to the missing momentum, and therefore to the  
1754 reconstructed  $B$  mass. Depending on the spin-parity of the particles and resonances  
1755 involved in the decay, two different mass distributions arise.

1756 In  $B$  decays where the missing particle is a scalar that is produced in the decay  
1757 of a vector resonance (eg.  $B^\pm \rightarrow D^{*0}(\rightarrow D^0\pi^0)\pi^\pm$  decays where the  $\pi^0$  is not  
1758 reconstructed), the  $m(D^0\pi^\pm)$  distribution has a double-peak structure. The  $D^{*0}$   
1759 helicity angle  $\theta$  is defined as the angle between the  $\pi^0$  momentum vector in the  $D^{*0}$   
1760 rest frame and the  $D^{*0}$  boost vector in the  $B$  rest frame. The helicity of  $D^{*0}$  means  
1761 that the  $\pi^0$  will travel predominantly in the direction where  $\theta = 0$  or  $\theta = \pi$ . When  
1762  $\theta = 0$  the fraction of momentum carried by the missing  $\pi^0$  is lower, leading to a higher  
1763 reconstructed  $m(D^0\pi^\pm)$ . When  $\theta = \pi$  the converse occurs. The resulting  $B$  mass  
1764 distribution is a parabola  $f_{\text{HORNS}}^0(m)$  peaking near both kinematic endpoints  $a$  and  $b$

$$f_{\text{HORNS}}^0(m) = \begin{cases} (m - \frac{a+b}{2})^2, & \text{if } a < m < b \\ 0, & \text{otherwise.} \end{cases} \quad (4.13)$$

1765 Due to the double-peaking structure, and the fact that was developed by Paolo  
1766 Gandini for the two-body ADS/GLW analyses [], this shape is denoted a *HORNSdini*  
1767 shape when convolved with a resolution function as described below.

1768 The second relevant decay situation is where the missing particle is a vector,  
1769 again produced via the intermediate decay of a vector resonance (eg.  $B^\pm \rightarrow$   
1770  $D^{*0}(\rightarrow D^0\gamma)\pi^\pm$  decays where the photon is not reconstructed). In this case, the  
1771 spin-parity of the photon ( $1^-$ ) means that it will decay preferentially in the  $\theta = \frac{\pi}{2}$   
1772 or  $\theta = \frac{3\pi}{2}$  directions, and so a double-peak structure is not seen. In this case

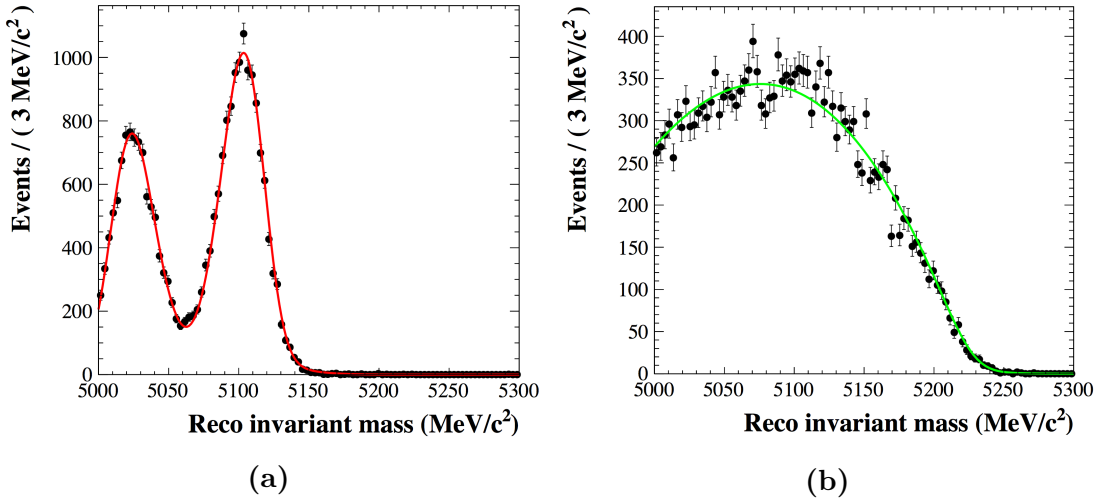


**Figure 4.22:** (a) The *HORNSdini* distribution (red) fit to  $B^\pm \rightarrow (D^{*0} \rightarrow D^0[\pi^0])\pi^\pm$  MC (black) after full event selection. (b) The *HILLSdini* distribution (green) fit to  $B^\pm \rightarrow (D^{*0} \rightarrow D^0[\gamma])\pi^\pm$  MC (black) after full event selection.

<sup>1773</sup> the parabolic distribution  $f_{\text{HILL}}^0(m)$  with kinematic endpoints  $a, b$  has negative  
<sup>1774</sup> curvature and can be described by

$$f_{\text{HILL}}^0(m) = \begin{cases} -(m-a)(m-b), & \text{if } a < x < b \\ 0, & \text{otherwise.} \end{cases} \quad (4.14)$$

1775 Resolution effects mean that the parabolic shapes must be convolved with a  
 1776 resolution function, chosen to be a sum of two Gaussians. For a single Gaussian  
 1777 shape  $f_G(x|\mu, \sigma)$  with mean  $\mu$  and width  $\sigma$ , the double Gaussian is expressed as

$$f_{DG}(x) = f_G(x|\mu, \sigma) + k_G f_G(x|\mu, R_\sigma \sigma). \quad (4.15)$$

where  $\sigma$  is the width of the first Gaussian, and  $k_G$  is the relative fractions between the two Gaussians and  $R_\sigma$  is their relative widths. Further, selection effects can distort the horns shape such that one of the peaks is higher than the other. This is taken into account by introducing a linear polynomial with slope parameter  $\xi$ . As  $\xi \rightarrow 0$ , the left hand peak decreases in size relative to the right hand peak. The resulting *HORN<sub>dini</sub>* and *HILL<sub>dini</sub>* distributions are therefore

$$f_{\text{HORNS/HILL}}(m) = \int_a^b dx f_{\text{HORNS/HILL}}^0(x) f_{DG}(m|x, \sigma, k_G, R_\sigma) \left( \frac{1-\xi}{b-a}x + \frac{b\xi - a}{b-a} \right). \quad (4.16)$$

<sup>1784</sup> Examples of the shapes are given in Fig. 4.22. A further term  $\delta m$  can be added  
<sup>1785</sup> to allow a translation of the full shape. These shapes are used to fit all partially  
<sup>1786</sup> reconstructed backgrounds, as described in the following section.

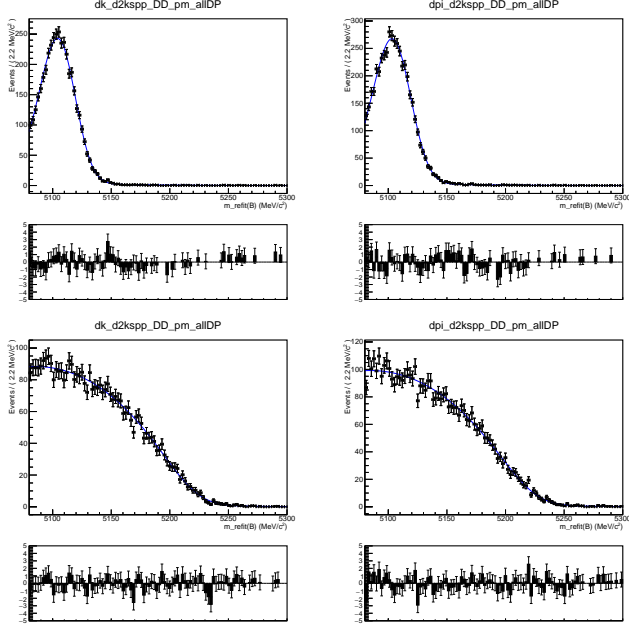


**Figure 4.23:** Fit projection of the fit to (top) simulated  $B^+ \rightarrow D^{*0}(\rightarrow D^0[\pi^0])h^\pm$  decays and (bottom) simulated  $B^+ \rightarrow D^{*0}(\rightarrow D^0[\gamma])h^\pm$  decays, all reconstructed in the DD category. Both the (left)  $DK$  shapes and (right) shows  $D\pi$  shapes are shown.

### 1787 Determination of the partially reconstructed background distributions

1788 In both the  $B^\pm \rightarrow DK^\pm$  and  $B^\pm \rightarrow D\pi^\pm$  categories, components are included to  
 1789 describe contributions from the partially reconstructed decays (where the particle  
 1790 in square brackets is not reconstructed)

- 1791     •  $B^\pm \rightarrow (D^{*0} \rightarrow D^0[\pi^0])h^\pm$ , described using a *HORNsdini* distribution
- 1792     •  $B^\pm \rightarrow (D^{*0} \rightarrow D^0[\gamma])h^\pm$ : described using a *HILLdini* distribution
- 1793     •  $B^0 \rightarrow (D^{*\pm} \rightarrow D^0[\pi^\pm])h^\mp$ : described using a *HORNsdini* distribution
- 1794     •  $B^{\pm(0)} \rightarrow D^0 h^\pm [\pi^{0(\mp)}]$ : described using a *HORNsdini* distribution

1795 The mass distributions of all the  $B \rightarrow D^*h^\pm$  contributions are obtained from  
 1796 fits to samples of full LHCb simulation. Examples of these fits are shown in  
 1797 Fig. 4.23. All shape parameters are kept fixed in the fit to data, except for the  
 1798 parameter  $\sigma$  of the resolution function in Eq. (4.15) which is allowed to obtain  
 1799 the value preferred by data.

1800 The mass distribution of  $B^{\pm(0)} \rightarrow D^0 h^\pm [\pi^{0(\mp)}]$  decays reconstructed in the  
 1801  $B^\pm \rightarrow D\pi^\pm$  categories is obtained from full LHCb simulation samples of  $B^\pm \rightarrow D^0\rho^\pm$   
 1802 and  $B^0 \rightarrow D^0\rho^0$  decays. The shapes were compared to those predicted by an  
 1803 amplitude model for  $B^0 \rightarrow D^0 \rightarrow \pi^\pm \pi^\mp$  decays developed by LHCb [106], but

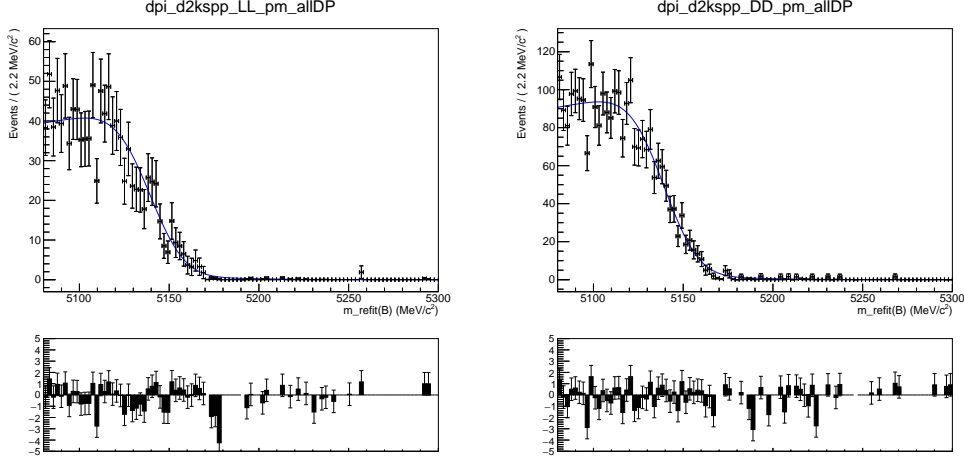


**Figure 4.24:** Projections of the fit to simulated  $B^\pm \rightarrow D\rho^\pm$  and  $B^0 \rightarrow D\rho^0$  samples reconstructed as  $B^\pm \rightarrow D\pi^\pm$  decays for (left) the LL and (right) the DD categories.

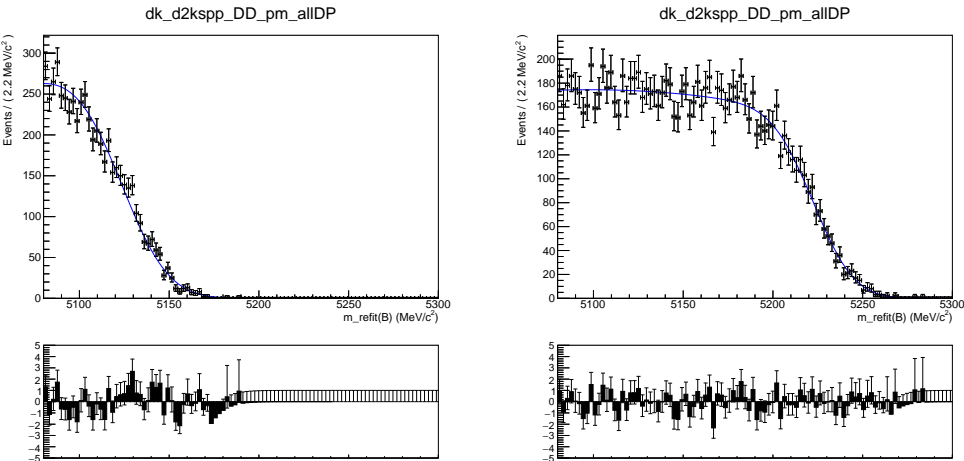


**Figure 4.25:** Fit projection for the fit used to obtain a shape for the partly reconstructed background from (left)  $B \rightarrow DK\pi$  decays and (right)  $B_s^0 \rightarrow DK^+\pi^-$  decays where a pion is not reconstructed.

1804 found to be very similar for the  $m(D\pi^\pm)$  range relevant to this analysis. The  
1805 obtained shapes are shown in Fig. 4.24.

1806 The mass distribution of  $B^{(0)} \rightarrow D^0 K^\pm [\pi^0(\mp)]$  decays reconstructed in the  
1807  $B^\pm \rightarrow DK^\pm$  categories, on the other hand, is obtained from a sample of signal  
1808 decays, generated via a amplitude model for  $B^0 \rightarrow D^0 \rightarrow K^\pm \pi^\mp$  decays developed  
1809 by LHCb [107] and smeared to take the LHCb resolution into account. This follows  
1810 an approach developed in the context of a GLW analysis based on partially recon-  
1811 structed decays made within LHCb [108]. The obtained shape is shown in Fig. 4.25.

1812 The background yields of these backgrounds are parameterised in terms of  
1813 one total yield parameter, accounting for all partially reconstructed  $B^\pm$  and

1814  $B^0$  decays, and a number of parameters that describe the relative rates of the  
1815 different contributions. In the  $B^\pm \rightarrow D\pi^\pm$  channels, the relative rates of the  
1816  $B^\pm \rightarrow (D^{*0} \rightarrow D^0[\pi^0])h^\pm$  and  $B^0 \rightarrow (D^{*\pm} \rightarrow D^0[\pi^\pm])h^\mp$  backgrounds are fixed  
1817 from the known branching fractions, and relative selection efficiencies in simulation.  
1818 These backgrounds have almost identical mass distributions and it is not possible to  
1819 determine the ratio in the fit to data. The relative yield of  $B^\pm \rightarrow D^*(\rightarrow D^0[\gamma])\pi^\pm$   
1820 compared to the  $B \rightarrow D^*(\rightarrow D^0[\pi])\pi^\pm$  is denoted  $f_{D^*\gamma}^{D\pi}$  and is floated in the fit to  
1821 data, as is the relative yield of  $B \rightarrow D^0\pi^\pm[\pi]$  decays compared to the  $B \rightarrow D^*\pi$   
1822 modes, denoted  $f_{D\pi\pi}^{D\pi}$ . In the  $B^\pm \rightarrow DK^\pm$  channels, all the relative background  
1823 rates are fixed via known branching fractions and relative selection efficiencies; this  
1824 is necessary to obtain a stable fit, due to the lower yields.

1825 In the  $B^\pm \rightarrow DK^\pm$  categories, an additional partially reconstructed background  
1826 is considered from  $B_s^0 \rightarrow \bar{D}^0[\pi^+]K^-$  (an conjugate) decays. The mass shape is  
1827 obtained from simulated decays, generated using an amplitude model published by  
1828 LHCb [109] and smeared to account for the experimental resolution. The obtained  
1829 shape is shown in Fig. 4.25. The yield of this background component is fixed relative  
1830 to the signal yields in the corresponding  $B^\pm \rightarrow D\pi^\pm$  category, taking the relative  
1831 branching ratios and hadronisation factors into account.

1832 In the  $B^\pm \rightarrow DK^\pm$  channels there is a contribution from partially reconstructed  
1833  $B \rightarrow D^*\pi^\pm X$  decays where the companion pion is misidentified as a kaon. The  
1834 reverse contribution is negligible due to the relative branching fractions, and the  
1835 fact that it is mostly shifted below the mass range of the fit. These are modelled  
1836 using analytic, empirical mass distributions (essentially sums of a number of regular  
1837 *HORN/HILLdini* distributions), with parameters that are determined in fits to  
1838 simulated  $B \rightarrow D^*\pi^\pm$  and  $B \rightarrow D\rho$  decays where the pion is reconstructed with  
1839 the kaon mass hypothesis. The shapes are fixed in the fit to data.

1840

#### 1841 Partially reconstructed backgrounds that are not modelled

1842 It was considered whether a background from  $\Lambda_b^0 \rightarrow D^0 p\pi^-$  decays where a pion  
1843 is not reconstructed, and the proton is misidentified as the companion, can be  
1844 expected to contribute significantly. This has been investigated in full LHCb  
1845 simulation samples, for the  $D$  final state  $K_S^0\pi^+\pi^-$ . Taking into account the selection  
1846 efficiencies, branching fractions, and hadronisation fraction of this background, the  
1847 expected relative yield of the  $\Lambda_b^0$  background compared to signal of 0.03 % in the  
1848  $B^\pm \rightarrow D\pi^\pm$  channel, which is completely negligible. In the  $B^\pm \rightarrow DK^\pm$  channel,  
1849 total of about 200 decays are expected, combined for the LL and DD categories.

1850 However, most of these lie at  $B$  masses smaller than the signal peak, and their impact  
 1851 is small. Therefore it is not necessary to model the background in the nominal fit;  
 1852 a systematic uncertainty is assigned that accounts for the small potential impact.

1853 In the analogous case of  $\Lambda_b^0 \rightarrow D^0 p K^-$  decays, the missing energy of the non-  
 1854 reconstructed kaon results in a reconstructed  $B$  mass below the fit range.

1855 It has also been investigated whether a background from  $\Lambda_b^0 \rightarrow \Lambda_c^+ \pi^-$  or  $\Lambda_b^0 \rightarrow$   
 1856  $\Lambda_c^+ K^-$  decays can be expected, where  $\Lambda_c^+ \rightarrow p K_S^0 \pi^+ \pi^-$ , a pion is missed and the  
 1857 proton is misidentified as a pion or kaon from the  $D$  decay. Since no PID requirement  
 1858 is made on the  $D$  decay products in the  $D \rightarrow K_S^0 \pi^+ \pi^-$  channels, and only a loose  
 1859 one for  $D \rightarrow K_S^0 K^+ K^-$ , this is possible in principle. In practice, the background is  
 1860 sufficiently suppressed from the applied  $D$  mass requirement to have no significant  
 1861 impact, and is therefore not modelled. A systematic uncertainty is assigned that  
 1862 accounts for any potential impact on the measurement due to this choice.

#### 1863 4.3.4 Combinatorial background

1864 The combinatorial background is modelled with an exponentially falling density  
 1865 function, where both the yield and exponential slope are determined independently  
 1866 for each category. This shape is found to model the combinatorial well in all  
 1867 categories, most evident in the high- $m_B$  regions where this background dominates.

#### 1868 4.3.5 Fit results

1869 The fit range is chosen to be  $m_B \in [5080, 5800] \text{ MeV}/c^2$ . The low end of this  
 1870 interval includes the high-mass peak of the double-peak structure in the partially  
 1871 reconstructed background, which helps the fit constrain the relative contributions of  
 1872 backgrounds in the lowmass regions. A number of additional backgrounds exist at  
 1873 even lower  $m_B$  values, thus extending the fit range to lower masses would necessitates  
 1874 an extended model, but not benefit the description of the signal region. The high  
 1875 end of the interval includes enough combinatorial background to allow the fit to  
 1876 determine the exponential slope parameter accurately.

1877 A large number of pseudoexperiments are carried out to verify that the fit  
 1878 procedure is self-consistent, in which toy data sets are generated according to the  
 1879 expected  $B$  mass distributions, and then fitted. None of the parameters obtained  
 1880 in the fit exhibit a mean bias different from zero, and for most parameters the  
 1881 uncertainties are well estimated. This is the case for the signal yields, and the  
 1882  $DK^\pm - D\pi^\pm$  yield ratio  $\mathcal{R}$ , as evidenced by the pull plots in Fig. 4.26. The fit  
 1883 underestimates the uncertainty by 10-20 % for some of the parameters related to

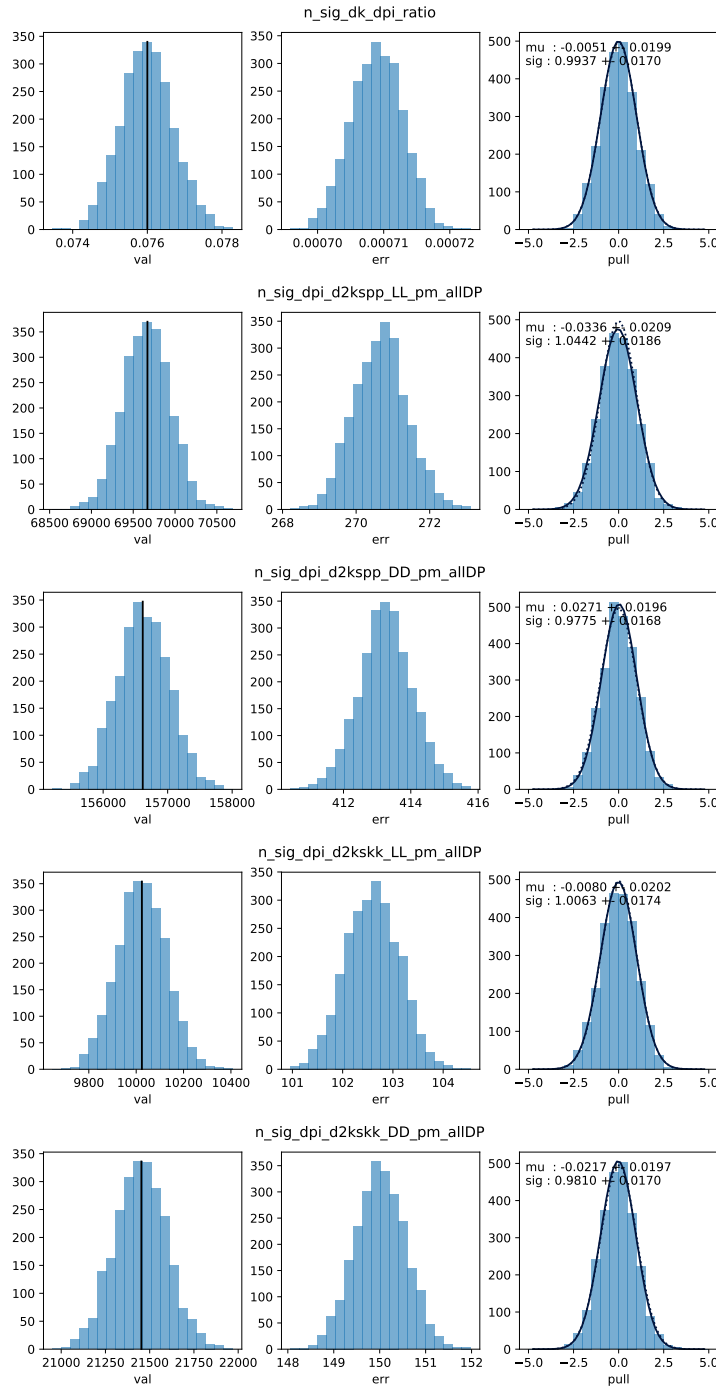


**Figure 4.26:** Pull plots for the signal yield parameters in global fits to toy datasets for (top) the  $D\pi^\pm$ - $DK^\pm$  yield ratio, and then the  $D\pi^\pm$  yield in the LL and DD  $D \rightarrow K_S^0\pi^+\pi^-$  modes, and the LL and DD  $D \rightarrow K_S^0K^+K^-$  modes.

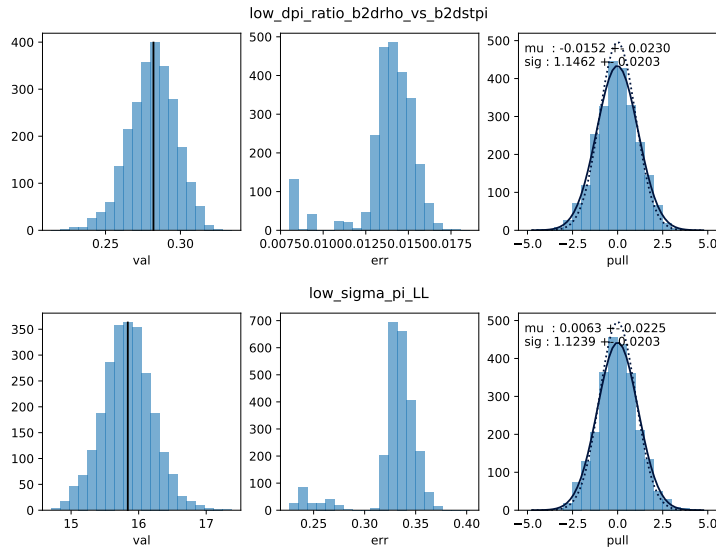


**Figure 4.27:** Examples of lowmass related parameters where the uncertainties are underestimated in some toy fits. This is taken into account when propagating the fit uncertainties to the systematic uncertainties on the final results.

the partly reconstructed backgrounds, as shown in Fig. 4.27, but this is taken into account when the uncertainties are propagated to the observables in the second-stage fit, as described in Section 4.5.1.

The projections of the fit to data are shown in Figs. 4.28 and 4.29, for the  $D \rightarrow K_S^0 \pi^+ \pi^-$  and  $D \rightarrow K_S^0 K^+ K^-$  data sets, respectively. The obtained yields for each fit component are given in Table 4.6. The total yield of  $B^\pm \rightarrow D\pi^\pm$  decays is approximately 230,000 across all channels. The obtained value of the yield ratio is  $\mathcal{R} = (7.7 \pm 0.1) \%$ , corresponding to a total  $B^\pm \rightarrow DK^\pm$  yield of 16,500, of which about 14,300 pass the PID requirement and are reconstructed in the  $B^\pm \rightarrow DK^\pm$  category. This value of  $\mathcal{R}$  is in excellent agreement with expectation from the known branching fractions [76], which predict  $\mathcal{R}_{\text{PDG}} = (7.8 \pm 0.3) \%$ . The shape parameters determined in the fit to data are summarised in Table 4.7.

## 4.4 Measurement of the CP-violation observables

The section describes the second fit stage, in which the  $CP$ -violation observables of interest are determined. Compared to the first fit stage, the candidates are further split by  $B$  charge, and by the assigned Dalitz bin number, making for a total of 160 categories. Another extended maximum-likelihood fit is carried out, in which shape parameters of all signal and background components are fixed to those determined in the first fit stage, and thus all floating parameters relate to

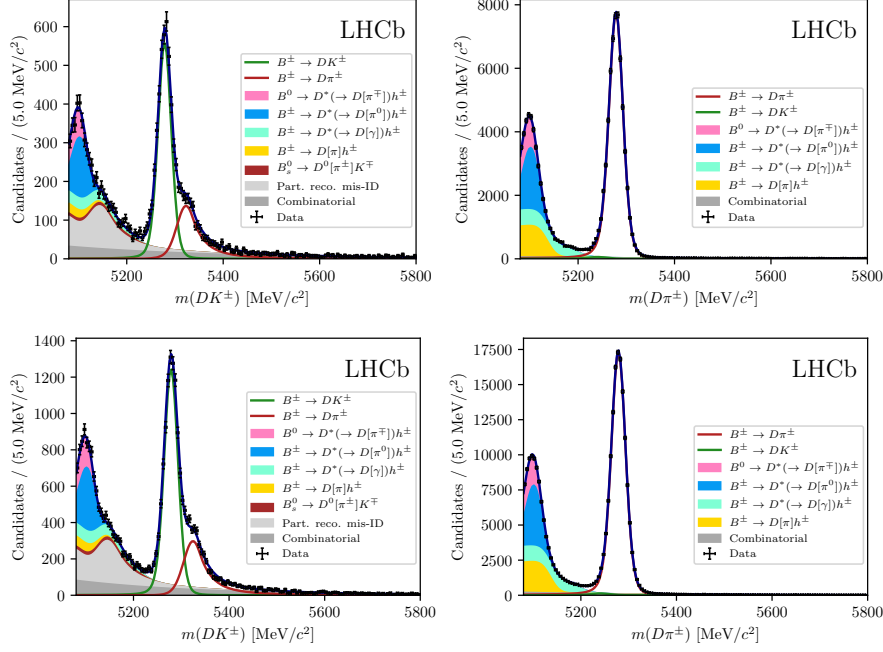


**Figure 4.28:** The invariant mass distribution for the (left)  $B^\pm \rightarrow DK^\pm$  channel and (right)  $B^\pm \rightarrow D\pi^\pm$  channel, where  $D \rightarrow K_S^0 \pi^+ \pi^-$  and the  $K_S^0$  is in the (top) LL and (bottom) the DD categories. The particle within square brackets in the legend denotes the particle that has not been reconstructed.

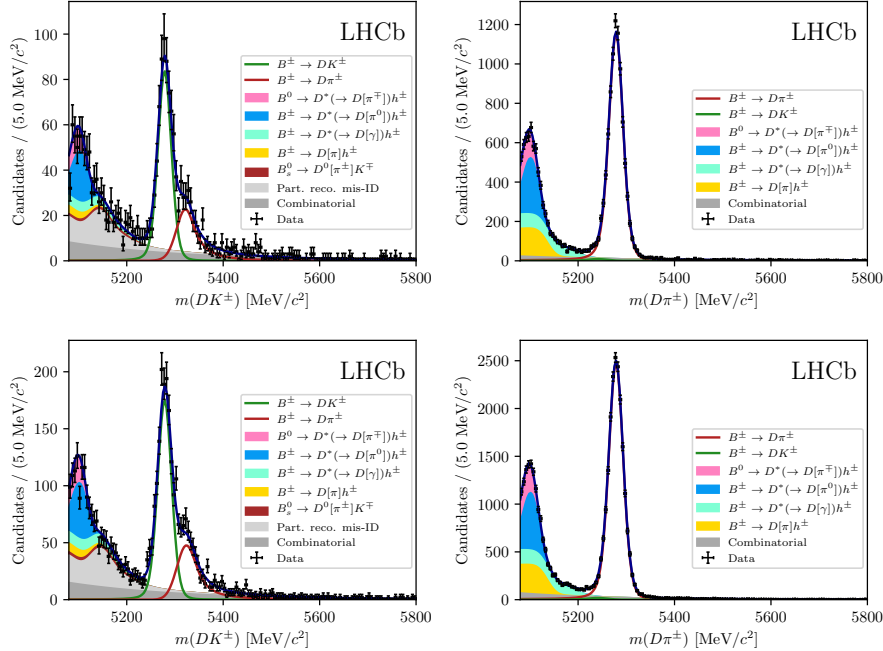


**Figure 4.29:** The invariant mass distribution for the (left)  $B^\pm \rightarrow DK^\pm$  channel and (right)  $B^\pm \rightarrow D\pi^\pm$  channel, where  $D \rightarrow K_S^0 K^+ K^-$  and the  $K_S^0$  is in the (top) LL and (bottom) the DD categories. The particle within square brackets in the legend denotes the particle that has not been reconstructed.

**Table 4.6:** Fitted total candidate yields. The quoted signal yields are for the number of candidates that survive the respective PID cut, whereas the  $DK^\pm$ - $D\pi^\pm$  ratio is corrected for PID and selection efficiencies so that it corresponds to the branching ratio.

Component	LL	DD
Signal		
$B^\pm \rightarrow D(\rightarrow K_S^0\pi^+\pi^-)\pi^\pm$	$61,573 \pm 254$	$139,080 \pm 389$
$B^\pm \rightarrow D(\rightarrow K_S^0K^+K^-)\pi^\pm$	$9,160 \pm 98$	$19,910 \pm 144$
$R_{DK/D\pi} = n(DK)/n(D\pi)$ (%)		$7.72 \pm 0.08$
Combinatorial		
$B^\pm \rightarrow D(\rightarrow K_S^0\pi^+\pi^-)\pi^\pm$	$3,479 \pm 198$	$9,928 \pm 376$
$B^\pm \rightarrow D(\rightarrow K_S^0K^+K^-)\pi^\pm$	$1,103 \pm 94$	$2,545 \pm 155$
$B^\pm \rightarrow D(\rightarrow K_S^0\pi^+\pi^-)K^\pm$	$1,826 \pm 107$	$3,987 \pm 177$
$B^\pm \rightarrow D(\rightarrow K_S^0K^+K^-)K^\pm$	$380 \pm 39$	$655 \pm 58$
Part. Reco.		
$B^\pm \rightarrow D(\rightarrow K_S^0\pi^+\pi^-)\pi^\pm$	$43,004 \pm 242$	$95,452 \pm 403$
$B^\pm \rightarrow D(\rightarrow K_S^0K^+K^-)\pi^\pm$	$6,247 \pm 99$	$13,241 \pm 157$
$R_{DK/D\pi}^{low} = n_{low}(DK)/n_{low}(D\pi)$ (%)		$6.65 \pm 0.12$

the signal and background yields. The signal yields are expressed in terms of the observables of interest,  $(x_\pm^{DK}, y_\pm^{DK}, x_\xi^{D\pi}, y_\xi^{D\pi})$ , allowing the fit to determine their optimal values. The details of the fit setup are summarised in the following section, before the results are presented in Section 4.4.2, and a wide range of consistency checks are described in Section 4.4.3.

#### 4.4.1 Fit setup

The signal yields in each bin (in a given category) are defined using the equations of Chapter 1, in order to allow for the determination of the  $(x_\pm^{DK}, y_\pm^{DK}, x_\xi^{D\pi}, y_\xi^{D\pi})$  observables. In practice, a set of variables are defined

$$Y_{c,i}^- = F_{c,-i} + [(x_-^c)^2 + (y_-^c)^2]F_{c,-i} + 2\sqrt{F_{c,i}F_{c,-i}}(c_i^cx_-^c + s_i^cy_-^c), \quad (4.17)$$

$$Y_{c,i}^+ = F_{c,-i} + [(x_+^c)^2 + (y_+^c)^2]F_{c,-i} + 2\sqrt{F_{c,i}F_{c,-i}}(c_i^cx_+^c - s_i^cy_+^c), \quad (4.18)$$

for each data category,  $c$ , in terms of which the bin yields that enter the likelihood are given by

$$N_{c,i}^\pm = \frac{Y_{c,i}^\pm}{\sum_j Y_{c,j}^\pm} \times N_{c,\text{total}}^\pm. \quad (4.19)$$

**Table 4.7:** Fitted parameter values.

	LL	DD
$\sigma_{D\pi}$ (MeV/c <sup>2</sup> )	$14.27 \pm 0.05$	$14.58 \pm 0.04$
$\sigma_{DK}$ (MeV/c <sup>2</sup> )	$13.61 \pm 0.24$	$14.19 \pm 0.17$
$\mu$ (MeV/c <sup>2</sup> )	$5278.60 \pm 0.04$	
Combinatorial Slopes		
Decay mode	Slope ( $10 \times 10^{-3} GeV^{-1}c^2$ )	
$B^\pm \rightarrow D(\rightarrow K_S^0\pi^+\pi^-)\pi^\pm$	$-3.1 \pm 0.2$	$-4.0 \pm 0.1$
$B^\pm \rightarrow D(\rightarrow K_S^0K^+K^-)\pi^\pm$	$-4.1 \pm 0.4$	$-5.5 \pm 0.3$
$B^\pm \rightarrow D(\rightarrow K_S^0\pi^+\pi^-)K^\pm$	$-3.2 \pm 0.2$	$-3.9 \pm 0.2$
$B^\pm \rightarrow D(\rightarrow K_S^0K^+K^-)K^\pm$	$-4.2 \pm 0.4$	$-4.3 \pm 0.4$
Part. Reco.		
$\sigma_{D\pi}^{low}$ (MeV/c <sup>2</sup> )	$13.73 \pm 0.33$	$13.78 \pm 0.28$
$f_{D\pi\pi}^{D\pi}$	$0.268 \pm 0.013$	
$f_{D^*\gamma}^{D\pi}$	$0.317 \pm 0.005$	

1914 This parameterisation is essentially identical to the expressions in Section 1.4,  
 1915 slightly modified so that the phase-space-integrated yields of  $B^+$  and  $B^-$  decays  
 1916 in a given category are determined directly, in lieu of the normalisation constants  
 1917  $h^\pm$  of that section. A single set of four parameters,  $(x_-^{DK}, y_-^{DK}, x_+^{DK}, y_+^{DK})$ , are  
 1918 shared between *all*  $B^\pm \rightarrow DK^\pm$  categories; they enter the expressions of Eq. (4.17)  
 1919 directly, and are thus determined in the fit. In the  $B^\pm \rightarrow D\pi^\pm$  categories, the  
 1920 four corresponding parameters,  $(x_-^{D\pi}, y_-^{D\pi}, x_+^{D\pi}, y_+^{D\pi})$ , are parameterised in terms of  
 1921  $(x_\pm^{DK}, y_\pm^{DK})$  and the addition two observables  $(x_\xi^{D\pi}, y_\xi^{D\pi})$ , as detailed in Section 1.4.  
 1922

1923 The strong-phase parameters  $(c_i, s_i)$  are fixed in the fit to data. In the  $D \rightarrow$   
 1924  $K_S^0\pi^+\pi^-$  categories, the combined CLEO [69] and BESIII [70] measurement results  
 1925 are used, as reported in Ref. [70]. In the  $D \rightarrow K_S^0K^+K^-$  categories, the results  
 1926 reported by the CLEO collaboration in Ref. [69] are used. The experimental  
 1927 uncertainty on these measurements is propagated to the measured  $CP$ -violation  
 1928 observables as part of the systematic uncertainties in Section ??.

1929 The  $F_i$  parameters are determined in the fit. Separate parameter sets are  
 1930 determined for the LL and DD categories because the acceptance profile over  
 1931 the Dalitz plot differs between them. The  $F_i$  are, however, shared between the  
 1932  $B^\pm \rightarrow DK^\pm$  and  $B^\pm \rightarrow D\pi^\pm$  categories; the small difference in the  $D$  momentum  
 spectrum between the channels does not lead to a detectable difference in the

acceptance profiles. This is a crucial assumption of the method, shown to be true using large samples of simulated decays in Section ???. Because the  $F_i$  are subject to the constraint that  $\sum_{i=-\mathcal{N}}^{\mathcal{N}} F_i^c = 1$ , it is beneficial to introduce a reparameterisation in the likelihood function. The  $F_i$  are re-expressed in terms of a set of recursive fractions

$$\mathcal{R}_i = \begin{cases} F_i & , \quad i = -\mathcal{N} \\ F_i / (\sum_{j \geq i} F_j) & , \quad -\mathcal{N} < i < +\mathcal{N} \end{cases} , \quad (4.20)$$

for which the constraint is much simpler, namely that each  $\mathcal{R}_i$  lies in the interval  $[0, 1]$ . This results in much better convergence behaviour in the minimisation of the negative log likelihood.

The yield of combinatorial background decays is determined independently in each bin. A single, overall bin yield of partially reconstructed background from  $B^\pm$  and  $B^0$  decays is determined in each of the 160 categories; the relative contribution from each individual background is fixed from the results of the first-stage fit, corrected for the different fit region (a systematic uncertainty is assigned due to this choice). In the  $B^\pm \rightarrow DK^\pm$  channels, the bin yields of the partially reconstructed background from  $B_s^0 \rightarrow \bar{D}^0[\pi^+]K^-$  decays are expressed via the  $F_i$ , exploiting that a positive companion particle is always produced along with a  $\bar{D}^0$  meson (and vice versa). The overall yield is fixed from the results of the first stage fit. Finally, the yield of the  $D\pi^\pm \leftrightarrow DK^\pm$  cross-feed components in each bin are determined via the obtained yield of correctly identified decays in the corresponding bin, and the known PID efficiencies. This is true for both fully and partially reconstructed decays, although only a  $D\pi^\pm \rightarrow DK^\pm$  component is included in the latter case.

The fit range is decreased to  $m_B \in [5150, 5800] \text{ MeV}/c^2$ . The information from candidates with lower reconstructed  $B$  masses was useful in determining the relative rates and free mass shape parameters of the partially reconstructed background components in the first-stage fit; however, with these fixed in the second-stage fit, this is no longer the case. Furthermore, the setup assumes that the shape of the partially reconstructed background is identical across the Dalitz bins. This assumption is not perfectly true, but the impact is minimal when the lower limit of the fit range is taken to be  $5150 \text{ MeV}/c^2$ .

## 1962 Self-consistency check

1963 In order to establish the fit stability and investigate a potential bias, a series of  
 1964 pseudoexperiments are run, in which toy datasets are generated using the model,  
 1965 and then fitted back. The total yields are taken from the first-stage fit. The signal

**Table 4.8:** Mean biases and pulls for the observables of interest in the final, binned fit, obtained in a large number of pseudoexperiments.

Parameter	Name in code	Mean bias ( $\times 10^{-2}$ )	Mean pull	Pull width
$x_-^{DK}$	A_xm_dk	$-0.018 \pm 0.022$	$-0.01 \pm 0.02$	$1.01 \pm 0.02$
$y_-^{DK}$	A_ym_dk	$-0.014 \pm 0.026$	$-0.00 \pm 0.02$	$0.99 \pm 0.02$
$x_+^{DK}$	A_xp_dk	$-0.018 \pm 0.022$	$-0.01 \pm 0.02$	$1.00 \pm 0.02$
$y_+^{DK}$	A_yp_dk	$-0.016 \pm 0.028$	$0.01 \pm 0.02$	$1.00 \pm 0.02$
$x_\xi^{D\pi}$	A_Re_xi_dpi	$0.029 \pm 0.052$	$0.06 \pm 0.02$	$1.00 \pm 0.02$
$y_\xi^{D\pi}$	A_Im_xi_dpi	$0.000 \pm 0.060$	$0.01 \pm 0.02$	$1.00 \pm 0.02$

1966 yields are distributed between Dalitz bins using input physics parameters that  
 1967 approximately equal the values obtained in Section 4.4.2 from the results of the fit  
 1968 to data. The  $F_i$  parameters are taken from a fit to data. The partly reconstructed  
 1969 background is distributed as " $D^0$ -like", ie. in the  $B^\pm$  channels  $N_i^\pm \propto F_{\mp i}$ , except for  
 1970 the  $B_s^0$  background, which is " $\bar{D}^0$ -like" ( $N_i^\pm \propto F_{\pm i}$ ). The combinatorial background  
 1971 includes real  $D$  mesons paired with a random bachelor, as well as fake  $D$  mesons  
 1972 that are themselves made up of random tracks. The former is distributed as 50/50  
 1973  $D^0$ -like and  $\bar{D}^0$ -like in the toy generation, whereas the latter is assumed to be evenly  
 1974 distributed over the Dalitz plot (ie. the bin yield is proportional to the bin area).

1975 A set of 2000 pseudoexperiments has been run, out of which 98.8 % converged  
 1976 properly. The pull plots for the observables of interest are shown in Fig. 4.30 and  
 1977 the mean biases and pulls are summarised in Table 4.8. No biases are statistically  
 1978 significant, and the uncertainties are seen to be well estimated.

#### 4.4.2 Main results

1980 The values and statistical uncertainties of observables obtained in the fit are

$$\begin{aligned} x_-^{DK} &= (-5.59 \pm 0.96) \times 10^{-2}, & y_-^{DK} &= (-6.45 \pm 1.14) \times 10^{-2}, \\ x_+^{DK} &= (-9.21 \pm 0.96) \times 10^{-2}, & y_+^{DK} &= (-1.21 \pm 1.20) \times 10^{-2}, \\ x_\xi^{D\pi} &= (-5.30 \pm 1.99) \times 10^{-2}, & y_\xi^{D\pi} &= (-1.03 \pm 2.34) \times 10^{-2}. \end{aligned} \quad (4.21)$$

1981 The statistical correlation matrix for the observables is given in Table 4.9. The  
 1982 2D log-likelihood profile for the observables is shown in Fig. 4.31.

1983 The full set of fit projections in all 160 categories is included in Appendix A.  
 1984 While the  $CP$  asymmetry of the phase-space integrated yield is small, this is not the  
 1985 case for all individual bin-pairs. This is shown in Fig. 4.32 where, as an example,  
 1986 the fit projections for the  $B^+ \rightarrow DK^+$  decays in bin +2 and the  $B^- \rightarrow DK^-$

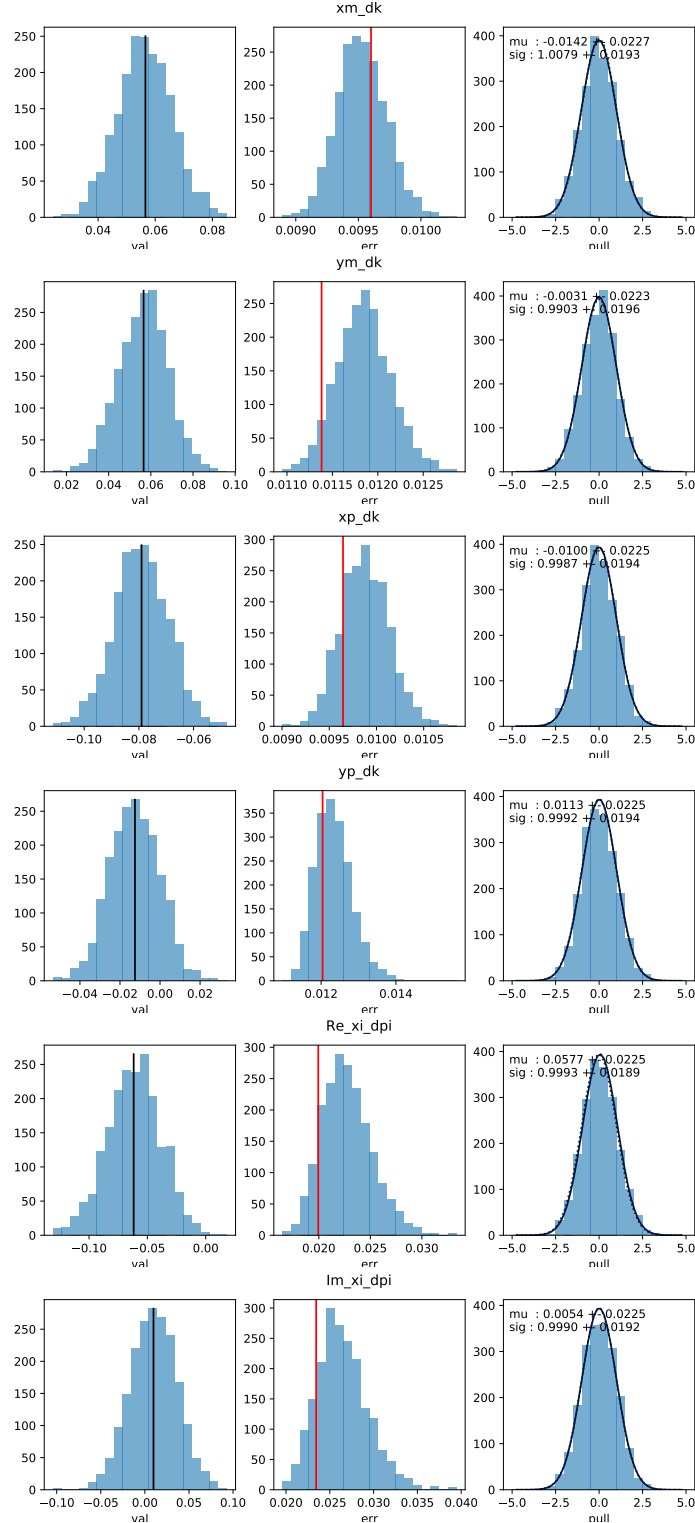


**Figure 4.30:** Pull plots for (from the top)  $x_{-}^{DK}$ ,  $y_{-}^{DK}$ ,  $x_{+}^{DK}$ ,  $y_{+}^{DK}$ ,  $x_{\xi}^{D\pi}$ , and  $y_{\xi}^{D\pi}$  from pseudoexperiments. The input values are shown with black lines in the left column. The uncertainty estimates in the fit to real data are shown with red lines in the central column.

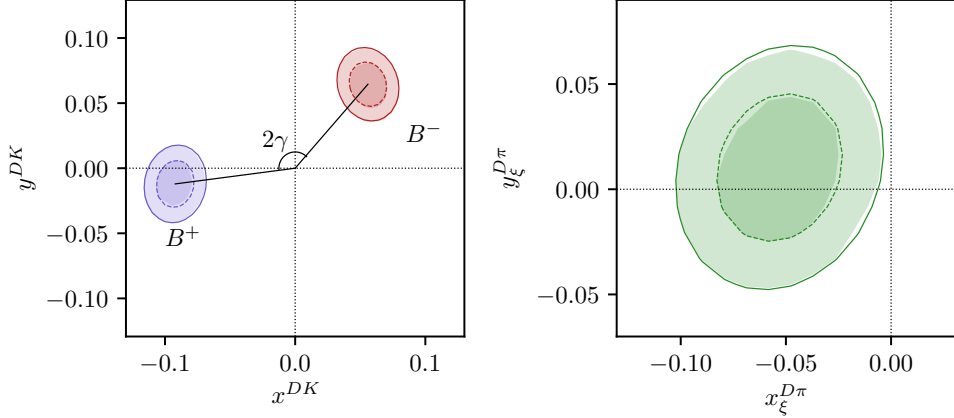


**Figure 4.31:** The 68 % and 95 % confidence regions for the fitted observables. The lines show the regions estimated from the covariance matrix returned by the default fit. The shaded areas are obtained in a likelihood scan, where the binned fit is run many times with all observables held at fixed values, scanning pairs of observables over the relevant ranges. The scan is made separately for the three pairs  $(x_-^{DK}, y_-^{DK})$ ,  $(x_+^{DK}, y_+^{DK})$ , and  $(x_\xi^{D\pi}, y_\xi^{D\pi})$ , holding the four other parameters fixed at their default-fit central values during a given scan. Then the minimum log-likelihood is related to a  $\chi^2$  via  $\mathcal{L}_{\min} = \frac{1}{2}\chi^2$  (discarding an irrelevant constant), and the confidence region limits placed at  $\chi^2 = 2.30$  and  $\chi^2 = 6.18$ , yielding the relevant percentiles for a  $\chi^2$  distribution with 2 degrees of freedom.

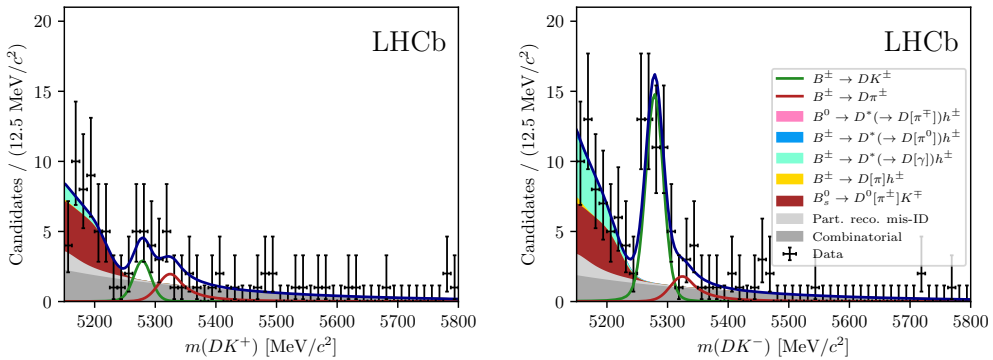


**Figure 4.32:** The invariant mass distribution for the (left)  $B^+ \rightarrow DK^+$  candidates in bin -2 and (right) the  $B^- \rightarrow DK^-$  candidates in bin +2, where  $D \rightarrow K_S^0\pi^+\pi^-$  and the  $K_S^0$  is reconstructed in the DD category.

1987 decays in bin  $-2$  of the  $D \rightarrow K_S^0\pi^+\pi^-$  Dalitz plot are compared. The presence  
1988 of  $CP$  violation is clearly visible.

1989 The obtained  $F_i$  parameter values are shown in Table 4.10. These parameters can  
1990 be useful in other BPGBS measurements made within the LHCb collaboration: it  
1991 is expected that the systematic uncertainty due to differences between the Dalitz-plot  
1992 acceptance profile in  $B^\pm \rightarrow Dh^\pm$  decays and, say,  $B \rightarrow D^*K$  or  $B \rightarrow DK^*$  decays  
1993 is smaller than the systematic arising from extracting the efficiency profile from

**Table 4.9:** Statistical uncertainties and correlation matrix for the fit to data.

Uncertainty ( $\times 10^{-2}$ )						
	$x_-^{DK^\pm}$	$y_-^{DK^\pm}$	$x_+^{DK^\pm}$	$y_+^{DK^\pm}$	$x_\xi^{D\pi^\pm}$	$y_\xi^{D\pi^\pm}$
$\sigma$	0.96	1.14	0.96	1.20	1.99	2.34

Correlations						
	$x_-^{DK^\pm}$	$y_-^{DK^\pm}$	$x_+^{DK^\pm}$	$y_+^{DK^\pm}$	$x_\xi^{D\pi^\pm}$	$y_\xi^{D\pi^\pm}$
$x_-^{DK^\pm}$	1.000	-0.125	-0.013	0.019	0.028	-0.165
$y_-^{DK^\pm}$		1.000	-0.011	-0.009	0.105	0.030
$x_+^{DK^\pm}$			1.000	0.088	-0.099	0.038
$y_+^{DK^\pm}$				1.000	-0.076	-0.141
$x_\xi^{D\pi^\pm}$					1.000	0.146
$y_\xi^{D\pi^\pm}$						1.000

<sup>1994</sup> simulated decays. Therefore, the obtain central values and uncertainties have been  
<sup>1995</sup> made public [1], including a set of systematic uncertainties discussed in Section ??.<sup>2</sup>

#### <sup>1996</sup> 4.4.3 Cross checks

<sup>1997</sup> A series of cross checks are performed to verify that the fit to data is behav-  
<sup>1998</sup> ing as expected.

#### <sup>1999</sup> Comparison to results of earlier analyses

<sup>2000</sup> It is confirmed that the results obtained in fits of the Run 1 or 2015+16 data  
<sup>2001</sup> sets in isolation are compatible with the results obtained in the original LHCb  
<sup>2002</sup> analyses of those data sets [3, 73]. In order to do so, the whole analysis procedure  
<sup>2003</sup> is carried out using only the relevant subset of data, and the strong-phase inputs  
<sup>2004</sup> from the CLEO collaboration are used in the fit. Two effects need to be taken  
<sup>2005</sup> into account when comparing the central values.

<sup>2006</sup> The overlap between the samples need to be taken into account. The overlap  
<sup>2007</sup> is not 100 % due to changes in the candidate selection. The overlap between the  
<sup>2008</sup> new selection and the data set of the original analysis of Run 1 data is about  
<sup>2009</sup> 70 %, whereas is it about 90 % for the 2015+16 data set. In order to determine the  
<sup>2010</sup> expected difference between the observables fitted from data sets with significant  
<sup>2011</sup> overlap, a large number of toy data sets were generated in sets of two, where  
<sup>2012</sup> 70 (90) % of decays were shared between the data sets. Both data sets were

---

<sup>2</sup>In practice, it is the obtained  $\mathcal{R}_i$  values that are made public.

**Table 4.10:** The fitted  $F_i$  values including statistical uncertainties. The underlying  $\mathcal{R}_i$  values are given with both statistical and systematic uncertainties in Section ??.

$F_i$ values: $D \rightarrow K_S^0 \pi^+ \pi^-$		
bin	LL	DD
-8	$0.024 \pm 0.001$	$0.024 \pm 0.000$
-7	$0.127 \pm 0.001$	$0.133 \pm 0.001$
-6	$0.062 \pm 0.001$	$0.056 \pm 0.001$
-5	$0.046 \pm 0.001$	$0.042 \pm 0.001$
-4	$0.095 \pm 0.001$	$0.095 \pm 0.001$
-3	$0.160 \pm 0.001$	$0.160 \pm 0.001$
-2	$0.153 \pm 0.001$	$0.153 \pm 0.001$
-1	$0.095 \pm 0.001$	$0.097 \pm 0.001$
1	$0.022 \pm 0.001$	$0.020 \pm 0.000$
2	$0.005 \pm 0.000$	$0.005 \pm 0.000$
3	$0.004 \pm 0.000$	$0.004 \pm 0.000$
4	$0.055 \pm 0.001$	$0.056 \pm 0.001$
5	$0.027 \pm 0.001$	$0.022 \pm 0.000$
6	$0.004 \pm 0.000$	$0.003 \pm 0.000$
7	$0.055 \pm 0.001$	$0.057 \pm 0.001$
8	$0.067 \pm 0.001$	$0.072 \pm 0.001$

$F_i$ values: $D \rightarrow K_S^0 K^+ K^-$		
bin	LL	DD
-2	$0.207 \pm 0.004$	$0.202 \pm 0.003$
-1	$0.222 \pm 0.004$	$0.230 \pm 0.003$
1	$0.290 \pm 0.005$	$0.296 \pm 0.003$
2	$0.281 \pm 0.005$	$0.271 \pm 0.003$

2013 fitted and the difference between the obtained central values for each observable  
2014 tabulated; the standard deviation of these distributions are used to calculate the  
2015 pulls between the old analysis results and the new fits to data. This check does  
2016 not take into account that the semi-leptonic PID cuts were introduced to remove a  
2017 potential peaking background, which may have had a small systematic effect on  
2018 the earlier measurement results. Thus the expected differences are likely to be  
2019 slightly underestimated and the check conservative.

2020 Furthermore, the  $F_i$  parameters were determined in a semi-leptonic control  
2021 channel in the earlier analyses. Therefore, the expected difference obtained above is  
2022 adjusted by adding the  $F_i$ -related systematic uncertainty of the original analysis  
2023 in quadrature, when comparing the old results to those in new fits to the Run 1  
2024 and 15+16 data sets. No further corrections have been made to the expected

**Table 4.11:** Comparison between the results on the Run 1 analysis [73] and the central values obtained when fitting the Run 1 dataset with the selection and fit setup described in this note. The pull is calculated using the  $1\sigma$  expected difference, which takes the sample overlap and the systematic uncertainty on the  $F_i$  parameters in the previous analysis into account, but assumes all other systematic uncertainties to be perfectly correlated. The new fits are performed using the CLEO strong-phase inputs.

Observable	Run 1 result [73]	New Fit (central value $\times 10^{-2}$ )	Pull
$x_-^{DK}$	2.50	4.04	0.85
$y_-^{DK}$	7.50	9.14	1.02
$x_+^{DK}$	-7.70	-9.40	-0.91
$y_+^{DK}$	-2.20	0.80	1.77
<i>p</i> -value: 0.057			

**Table 4.12:** Comparison between the results on the 2015+16 analysis [3] and the central values obtained when fitting the 2015+16 dataset with the selection and fit setup described in this note. The pull is calculated using the  $1\sigma$  expected difference, which takes the sample overlap and the systematic uncertainty on the  $F_i$  parameters in the previous analysis into account, but assumes all other systematic uncertainties to be perfectly correlated. The new fits are performed using the CLEO strong-phase inputs.

Observable	15+16 result [3]	New Fit (central value $\times 10^{-2}$ )	Pull
$x_-^{DK}$	9.00	8.36	-0.50
$y_-^{DK}$	2.10	1.16	-0.62
$x_+^{DK}$	-7.70	-8.58	-0.56
$y_+^{DK}$	-1.00	-2.82	-1.39
<i>p</i> -value: 0.239			

2025 differences, which effectively assumes all other systematic uncertainties to be 100 %  
 2026 correlated. Also for this reason can the check be considered conservative. As can  
 2027 be seen in Tables 4.11 and 4.12, neither the Run 1 and 2015+16 comparisons show  
 2028 unreasonable differences in central values.

### 2029 Directly fitting the signal yields

2030 As a cross-check, the fit is run in an alternative mode, in which the signal yields of  
 2031 each bin are independent parameters. The obtained yields are compared to those  
 2032 predicted from the results of the default fit in Fig. 4.33. The yields are shown for  
 2033 each "effective bin", where effective bin  $i$  is defined as bin  $+i$  for  $B^+$  decays and bin  
 2034  $-i$  for  $B^-$  decays; in the  $CP$  symmetric case, these bins are expected to have equal

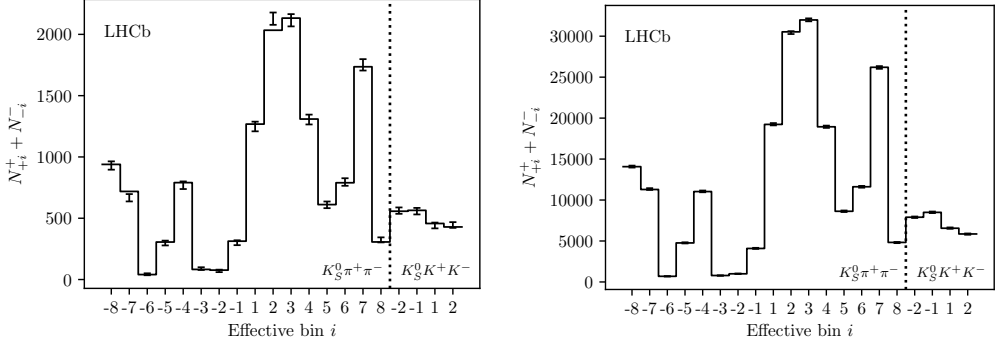


**Figure 4.33:** Comparison of (lines) the predicted yield given the determined  $CP$  observables and (error bars) the yield obtained in fits to data where each yield is an independent parameter. The yields are shown for (left)  $B^\pm \rightarrow DK^\pm$  decays and (right)  $B^\pm \rightarrow D\pi^\pm$  decays. The LL and DD categories have been combined, as has the  $B^+$  and  $B^-$  yields for each effective Dalitz bin, defined as bin  $+i$  for  $B^+$  decays and bin  $-i$  for  $B^-$  decays.

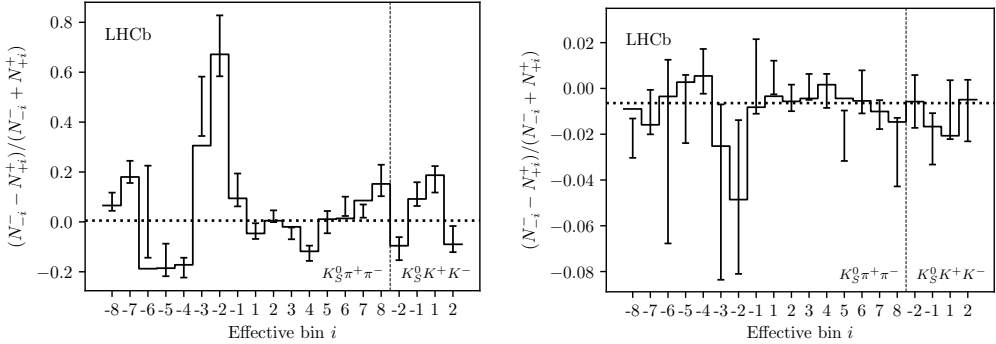


**Figure 4.34:** The bin-by-bin asymmetries  $(N_{-i}^- - N_{+i}^+)/N_{-i}^- + N_{+i}^+$  for each Dalitz-plot bin number for (left)  $B^\pm \rightarrow DK^\pm$  decays and (right)  $B^\pm \rightarrow D\pi^\pm$  decays. The prediction from the central values of the  $CP$ -violation observables is shown with a solid line and the asymmetries obtained in fits with independent bin yields are shown with the error bars. The predicted asymmetries in a fit that does not allow for  $CP$  violation are shown with a dotted line.

2035 yields (modulo production and detection asymmetries). The agreement between the  
2036 two fit set-ups is seen to be excellent. The normalised yield asymmetries, defined as

$$A^i \equiv \frac{N_{-i}^- - N_{+i}^+}{N_{-i}^- + N_{+i}^+} \quad (4.22)$$

2037 are shown in Fig. 4.34 for all decay channels. Again, the agreement between  
2038 the nominal fit, and the alternative fit with independent yields is found to be  
2039 excellent. It is also clear how, in the case of  $B^\pm \rightarrow DK^\pm$  decays, the asymmetry  
2040 is significantly different from zero for a number of bin pairs.

2041 **Fitting subsets of the data separately**

2042 One cross check is carrying out, by determining the  $CP$  observables using a number  
2043 of independent sub samples of the data set separately. This is done for the  
2044 following following data splits

- 2045 • Fig. 4.35a shows the two dimensional log likelihood contours for the observables  
2046 for fits to the Run 1, 2015+16, 2017 and 2018 datasets separately
- 2047 • Fig. 4.35b shows the same plots, comparing the fits to the data set split by  
2048  $K_S^0$  track type.
- 2049 • Fig. 4.35c shows the same plots, comparing the fits to the data set split by  
2050 whether the candidate event was triggered by one of the signal particles at the  
2051 hardware level (TOS), or by another particle in the underlying event (TIS).
- 2052 • Fig. 4.35d shows the same plots, comparing the fits to the data set split the  
2053 magnet polarity during data taking.
- 2054 • Fig. 4.35e shows the same plots, comparing the fits to the data set split by  
2055 whether the  $D$  meson decays to the  $K_S^0\pi^+\pi^-$  or  $K_S^0K^+K^-$  final state.

2056 All figures show the Gaussian likelihood contours corresponding to the statistical  
2057 uncertainties. There is good agreement between the results in all cases, given  
2058 that in each cases the sub datasets are independent and therefore the statistical  
2059 errors are uncorrelated.

2060 **Significantly tightening the companion PID requirement**

2061 One of the dominant backgrounds in the signal region of the  $B^\pm \rightarrow DK^\pm$  channel is  
2062 from partly reconstructed  $B \rightarrow D\pi X$  decays where the bachelor pion is misidentified  
2063 as a kaon. The background mode is well described by the included shape component,  
2064 and included in all relevant systematic studies. Nevertheless, an additional cross  
2065 check is carried out to ensure that it is not having a significant effect on the fit: the  
2066 analysis is repeated with PID requirement of  $\text{PID}_K > 12$  required to place a candidate  
2067 in the  $B^\pm \rightarrow DK^\pm$  category, instead of  $\text{PID}_K > 4$ . With this requirement 99.7 %  
2068 of  $B^\pm \rightarrow D\pi^\pm$  decays are correctly identified, making the cross-feed component  
2069 in the  $B^\pm \rightarrow DK^\pm$  channels significantly smaller than in the default fit. This  
2070 is clearly visible in Fig. 4.36, where the fit projections for the global fit of the  
2071  $D \rightarrow K_S^0\pi^+\pi^-$  modes are shown. In return, the probability of correctly identifying a  
2072 kaon companion drops to about 68–69 %, resulting in a smaller effective signal yield.

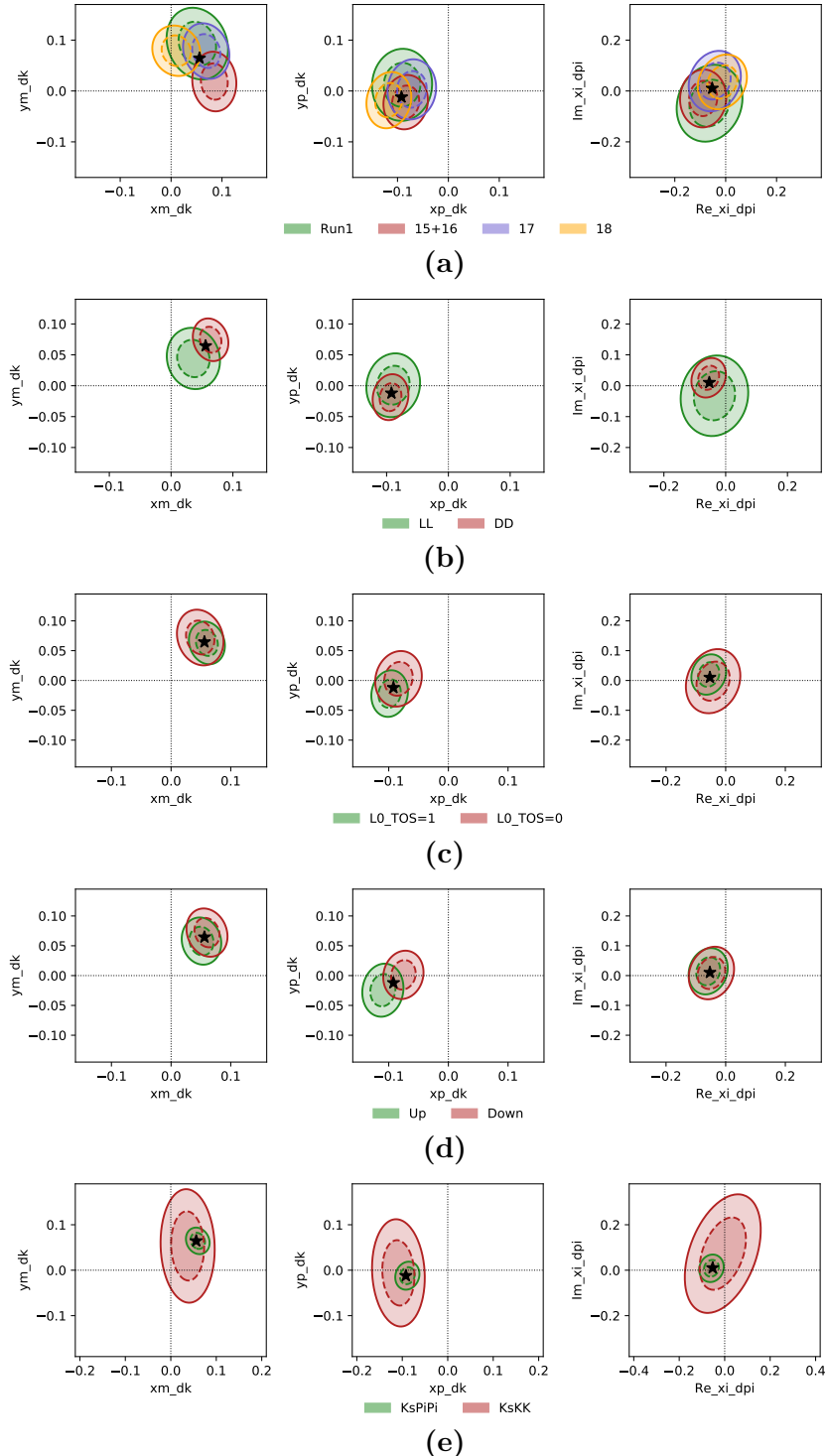


**Figure 4.35:** Comparison of the 68 % and 95 % confidence regions for (left)  $(x_{-}^{DK}, y_{-}^{DK})$ , (centre)  $(x_{+}^{DK}, y_{+}^{DK})$ , and (right)  $(x_{\xi}^{D\pi}, y_{\xi}^{D\pi})$  obtained from fits to sub sets of the data set. The uncertainties are statistical only. The central values of the default fit are shown with a black star. The dataset is split by (a) data taking year, (b) LL and DD  $K_S^0$  types, (c) trigger category, (d) magnet polarity, and (e)  $D$  decay mode.

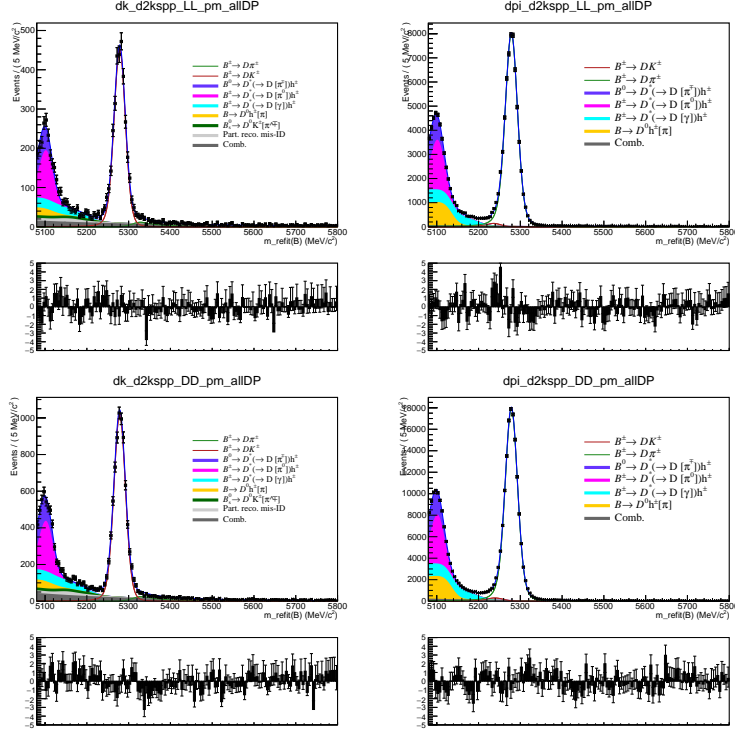


**Figure 4.36:** Fit projections for fits to the  $D \rightarrow K_S^0 \pi^+ \pi^-$  candidates with a bachelor PIDK cut at 12 instead of 4 used to split into (left)  $B^\pm \rightarrow DK^\pm$  and (right)  $B^\pm \rightarrow D\pi^\pm$  candidates, for (top) the LL and (bottom) DD categories.

The measurement results are compared in Table 4.13, where the differences in central value are seen to be reasonably small. It is not trivial to determine whether the difference is statistically significant or not: the same candidates are analysed in both cases, the difference being that a number of candidates that are placed in the  $B^\pm \rightarrow DK^\pm$  category in the nominal fit are placed in the  $B^\pm \rightarrow D\pi^\pm$  category in the alternative fit. The uncertainty will not be 100 % correlated because signal events that move from the  $DK$  to  $D\pi$  category are placed in a region with high background; however, this is somewhat compensated for by candidates that remain in the  $DK$  category gaining statistical power due to the increased purity. An estimate of the expected statistical fluctuation can be determined by taking the difference of the statistical uncertainties in quadrature. Using this estimate, the observed shifts are found to be consistent with statistical fluctuation, and thus there is no sign of the background from  $D\pi^\pm \rightarrow DK^\pm$  cross-feed causing issues.

#### Compare results obtained with different strong-phase inputs

It is interesting to compare the results obtained with different strong-phase inputs. This is done in Fig. 4.37, where the default fit results are compared to those

**Table 4.13:** Results of running the measurement with the default PIDK cut at 4 used to separate  $B^\pm \rightarrow DK^\pm$  and  $B^\pm \rightarrow D\pi^\pm$  candidates, as well as with an alternative PIK cut at 12, resulting in much lower cross-feed from misidentified  $B^\pm \rightarrow D\pi^\pm$  decays. We also show the pulls, defined as  $\Delta x / \sqrt{|\sigma_{PIDK>12}^2 - \sigma_{PIDK>4}^2|}$  as described in the main text body.

Parameter	PIDK > 4	PIDK > 12	$\sigma = \sqrt{\sigma_{PIDK>12}^2 - \sigma_{PIDK>4}^2}$	Pull
$x_-^{DK}$	$5.59 \pm 0.96$	$5.82 \pm 1.01$	0.30	0.77
$y_-^{DK}$	$6.45 \pm 1.14$	$6.86 \pm 1.19$	0.36	1.13
$x_+^{DK}$	$-9.21 \pm 0.96$	$-8.94 \pm 1.01$	0.30	0.93
$y_+^{DK}$	$-1.21 \pm 1.20$	$-0.94 \pm 1.26$	0.37	0.71
$x_\xi^{D\pi}$	$-5.30 \pm 1.99$	$-5.13 \pm 2.02$	0.32	0.52
$y_\xi^{D\pi}$	$1.03 \pm 2.34$	$1.71 \pm 2.33$	0.28	2.40

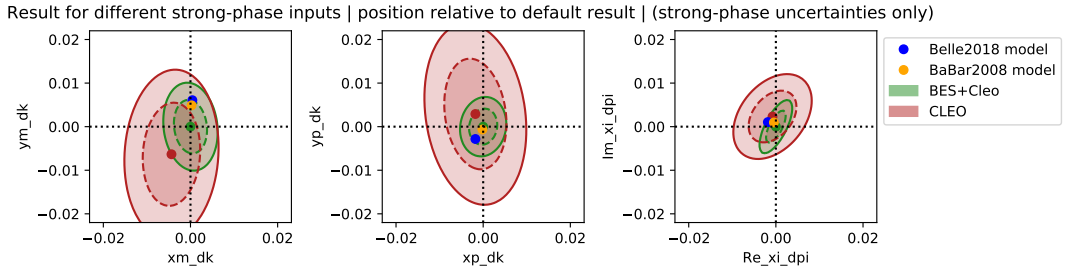


**Figure 4.37:** Fit results for (left)  $(x_-^{DK}, y_-^{DK})$ , (centre)  $(x_+^{DK}, y_+^{DK})$ , and (right)  $(x_\xi^{D\pi}, y_\xi^{D\pi})$  depending on strong-phase inputs, shown relative to the default fit results. The included results are based on (green) the BESIII-CLEO combination, which is the default, (red) the CLEO-only results, (blue dot) the 2018 Belle model [?] and (orange dot) the 2008 BaBar model [57]. For the measurements, only strong-phase related uncertainties are included in the plotted confidence regions.

obtained if the  $CP$  fit is done with the CLEO-only inputs [69], and with the model predictions from the 2018 Belle model [?] and the 2008 BaBar model [57]. For the measurements, only the strong-phase-related uncertainties are included in the plot, since the statistical uncertainties are correlated. All results are found to agree well.

## 4.5 Systematic uncertainties

### 4.5.1 Mass shapes

### 4.5.2 Charmless backgrounds

## 4.6 Obtained constraints on $\gamma$

# Appendices

A

2098

2099

Projections of main fit to data

## Bibliography

2100

- 2101 [1] LHCb collaboration, R. Aaij *et al.*, *Measurement of the CKM angle  $\gamma$  using*  
2102  $B^\pm \rightarrow [K_S^0 h^+ h^-]_{Dh^\pm}$  *decays*, Submitted to JHEP (2020).
- 2103 [2] M. Bjørn and S. Malde, *CP violation and material interaction of neutral*  
2104 *kaons in measurements of the CKM angle  $\gamma$  using  $B^\pm \rightarrow DK^\pm$  decays where*  
2105  $D \rightarrow K_S^0 \pi^+ \pi^-$ , JHEP **19** (2020) 106, arXiv:1904.01129.
- 2106 [3] LHCb collaboration, R. Aaij *et al.*, *Measurement of the CKM angle  $\gamma$  using*  
2107  $B^\pm \rightarrow DK^\pm$  *with  $D \rightarrow K_S^0 \pi^+ \pi^-$ ,  $K_S^0 K^+ K^-$  decays*, JHEP **08** (2018) 176,  
2108 Erratum ibid. **10** (2018) 107, arXiv:1806.01202.
- 2109 [4] E. Noether, *Invariante Variationsprobleme*, Nachrichten von der Gesellschaft  
2110 der Wissenschaften zu Göttingen, Mathematisch-Physikalische Klasse **1918**  
2111 (1918) 235.
- 2112 [5] J. F. Donoghue, E. Golowich, and B. R. Holstein, *Dynamics of the Standard*  
2113 *Model*, Cambridge University Press, Cambridge, 2014.
- 2114 [6] A. D. Sakarov, *Violation of CP Invariance, C Asymmetry, and Baryon*  
2115 *Asymmetry of the Universe*, JETP Letters **5** (1966) 24.
- 2116 [7] G. Luders, *On the Equivalence of Invariance under Time Reversal and under*  
2117 *Particle-Antiparticle Conjugation for Relativistic Field Theories*, Kong. Dan.  
2118 Vid. Sel. Mat. Fys. Medd. **28N5** (1954) 1.
- 2119 [8] C. S. Wu *et al.*, *Experimental Test of Parity Conservation in Beta Decay*,  
2120 Physical Review **105** (1957) 1413.
- 2121 [9] T. D. Lee and C. N. Yang, *Question of Parity Conservation in Weak*  
2122 *Interactions*, Physical Review **104** (1956) 254.
- 2123 [10] J. H. Christenson, J. W. Cronin, V. L. Fitch, and R. Turlay, *Evidence for the*  
2124  $2\pi$  *Decay of the  $K_2^0$  Meson*, Physical Review Letters **13** (1964) 138.

- [11] BABAR Collaboration *et al.*, *Observation of  $\mathcal{CP}$  Violation in the  $B\bar{B}^0$  Meson System*, Physical Review Letters **87** (2001) 091801.
- [12] Belle Collaboration *et al.*, *Observation of Large  $\mathcal{CP}$  Violation in the Neutral  $B$  Meson System*, Physical Review Letters **87** (2001) 091802.
- [13] K. Abe, *Study of  $B^{+-} \rightarrow D_{CP} K^{+-}$  and  $D^*_{CP} K^{+-}$  decays*, Physical Review D **73** (2006) 051106, [arXiv:hep-ex/0601032](https://arxiv.org/abs/hep-ex/0601032).
- [14] B. Collaboration *et al.*, *Evidence for the Suppressed Decay  $B^- \rightarrow DK^-$ ,  $D \rightarrow K+\pi^-$* , Physical Review Letters **106** (2011) 231803, [arXiv:1103.5951](https://arxiv.org/abs/1103.5951).
- [15] T. B. Collaboration and P. d. A. Sanchez, *Measurement of  $CP$  observables in  $B^{+-} \rightarrow D_{CP} K^{+-}$  decays and constraints on the CKM angle gamma*, Physical Review D **82** (2010) 072004, [arXiv:1007.0504](https://arxiv.org/abs/1007.0504).
- [16] The BABAR Collaboration *et al.*, *Search for  $b \rightarrow u$  transitions in  $B \hat{\rightarrow} D(K)\hat{\rightarrow} \ell\bar{\nu}$  and  $D^*\hat{\rightarrow} K\ell\bar{\nu}$  decays*, Physical Review D **82** (2010) 072006.
- [17] C. Collaboration, *Measurements of branching fraction ratios and  $CP$  asymmetries in  $B^{+/-} \rightarrow D_{CP} K^{+/-}$  decays in hadron collisions*, Physical Review D **81** (2010) 031105, [arXiv:0911.0425](https://arxiv.org/abs/0911.0425).
- [18] C. Collaboration, *Measurements of branching fraction ratios and  $CP$ -asymmetries in suppressed  $B^\pm \rightarrow D(\rightarrow K\pi)K^\pm$  and  $B^\pm \rightarrow D(\rightarrow K\pi)\pi^\pm$  decays*, Physical Review D **84** (2011) 091504, [arXiv:1108.5765](https://arxiv.org/abs/1108.5765).
- [19] LHCb collaboration, R. Aaij *et al.*, *Observation of  $CP$  violation in  $B^\pm \rightarrow DK^\pm$  decays*, Phys. Lett. **B712** (2012) 203, Erratum ibid. **B713** (2012) 351, [arXiv:1203.3662](https://arxiv.org/abs/1203.3662).
- [20] LHCb collaboration, R. Aaij *et al.*, *First observation of  $CP$  violation in the decays of  $B_s^0$  mesons*, Phys. Rev. Lett. **110** (2013) 221601, [arXiv:1304.6173](https://arxiv.org/abs/1304.6173).
- [21] LHCb collaboration, R. Aaij *et al.*, *Observation of  $CP$  violation in neutral  $D$ -meson decays*, LHCb-PAPER-2019-006, in preparation.

- 2156 [22] K. Abe *et al.*, *Constraint on the matter–antimatter symmetry-violating phase*  
2157 *in neutrino oscillations*, Nature **580** (2020) 339.
- 2158 [23] L. K. Gibbons *et al.*, *Measurement of the CP-violation parameter*  
2159  $Re(\mathcal{V}_{e\mu})'/\mathcal{V}_{e\mu}$ ), Physical Review  
2160 Letters **70** (1993) 1203.
- 2161 [24] G. D. Barr *et al.*, *A new measurement of direct CP violation in the neutral*  
2162 *kaon system*, Physics Letters B **317** (1993) 233.
- 2163 [25] J. R. Batley *et al.*, *A precision measurement of direct CP violation in the*  
2164 *decay of neutral kaons into two pions*, Physics Letters B **544** (2002) 97.
- 2165 [26] KTeV Collaboration *et al.*, *Measurements of direct CP violation,*  
2166 *CPT symmetry, and other parameters in the neutral kaon system*,  
2167 Physical Review D **67** (2003) 012005.
- 2168 [27] HFLAV, Y. S. Amhis *et al.*, *Averages of b-hadron, c-hadron, and  $\tau$ -lepton*  
2169 *properties as of 2018*, arXiv:1909.12524, updated results and plots available  
2170 at <https://hflav.web.cern.ch/>.
- 2171 [28] M. Kobayashi and T. Maskawa, *CP-Violation in the Renormalizable Theory*  
2172 *of Weak Interaction*, Progress of Theoretical Physics **49** (1973) 652.
- 2173 [29] N. Cabibbo, *Unitary Symmetry and Leptonic Decays*, Physical Review Letters  
2174 **10** (1963) 531.
- 2175 [30] L.-L. Chau and W.-Y. Keung, *Comments on the Parametrization of the*  
2176 *Kobayashi-Maskawa Matrix*, Physical Review Letters **53** (1984) 1802.
- 2177 [31] Particle Data Group, M. Tanabashi *et al.*, *Review of particle physics*, Phys.  
2178 Rev. **D98** (2018) 030001, and 2019 update.
- 2179 [32] L. Wolfenstein, *Parametrization of the Kobayashi-Maskawa Matrix*, Physical  
2180 Review Letters **51** (1983) 1945.
- 2181 [33] Y. H. Ahn, H.-Y. Cheng, and S. Oh, *Wolfenstein parametrization at higher*  
2182 *order: Seeming discrepancies and their resolution*, Physics Letters B **703**  
2183 (2011) 571.

- 2184 [34] A. J. Buras, M. E. Lautenbacher, and G. Os-  
 2185 termaier, *Waiting for the top quark mass,*  
 2186  $\hat{\{K\}}_+ \rightarrow \hat{\{K\}}_0 - \hat{\{K\}}_0$ -mixing, and CP asymmetries in B decays, Physical Review D **50** (1994) 3433.
- 2189 [35] J. Charles *et al.*, *CP violation and the CKM matrix: Assessing the impact of*  
 2190 *the asymmetric B factories*, The European Physical Journal C - Particles and  
 2191 Fields **41** (2005) 1.
- 2192 [36] J. Brod and J. Zupan, *The ultimate theoretical error on  $\gamma$  from  $B \rightarrow DK$*   
 2193 *decays*, Journal of High Energy Physics **2014** (2014) 51.
- 2194 [37] M. Blanke and A. J. Buras, *Emerging  $\Delta M_d$ -anomaly from*  
 2195 *tree-level determinations of  $V_{cb}$  and the angle  $\gamma$ ,* The European Physical Journal C **79** (2019) 159.
- 2197 [38] CKMfitter group, J. Charles *et al.*, *Current status of the Standard*  
 2198 *Model CKM fit and constraints on  $\Delta F = 2$  new physics*, Phys. Rev. **D91**  
 2199 (2015) 073007, arXiv:1501.05013, updated results and plots available at  
 2200 <http://ckmfitter.in2p3.fr/>.
- 2201 [39] UTfit collaboration, M. Bona *et al.*, *The unitarity triangle fit in the*  
 2202 *standard model and hadronic parameters from lattice QCD: A reap-*  
 2203 *praisal after the measurements of  $\Delta m_s$  and  $BR(B \rightarrow \tau\nu_\tau)$* , JHEP **10**  
 2204 (2006) 081, arXiv:hep-ph/0606167, updated results and plots available at  
 2205 <http://www.utfit.org/>.
- 2206 [40] E. Kou *et al.*, *The Belle II Physics Book*, Progress of Theoretical and  
 2207 Experimental Physics **2019** (2019) 123C01, arXiv:1808.10567.
- 2208 [41] LHCb collaboration *et al.*, *Physics case for an LHCb Upgrade II - Opportuni-*  
 2209 *ties in flavour physics, and beyond, in the HL-LHC era*, arXiv:1808.08865  
 2210 [hep-ex] (2019) arXiv:1808.08865.
- 2211 [42] Y. Grossman and M. Savastio, *Effects of  $K\bar{K}$ -mixing on determining  $\gamma$  from  $B^\pm \rightarrow DK^\pm$* , Journal of High Energy Physics **2014**  
 2212 (2014) 8.
- 2214 [43] M. Gronau and D. Wyler, *On determining a weak phase from charged B decay*  
 2215 *asymmetries*, Physics Letters B **265** (1991) 172.

- 2216 [44] M. Gronau and D. London, *How to determine all the angles of the unitarity*  
 2217 *triangle from  $Bd0 \rightarrow DKs$  and  $Bs0 \rightarrow D\phi$* , Physics Letters B **253** (1991)  
 2218 483.
- 2219 [45] D. Atwood, I. Dunietz, and A. Soni, *Enhanced CP Violation with*  
 2220  *$\mathcal{B} \rightarrow K\bar{D}$  Modes and Extraction of the Cabibbo-Kobayashi-Maskawa Angle*  
 2221  *$\gamma$* , Physical Review Letters **78** (1997) 3257.
- 2223 [46] D. Atwood, I. Dunietz, and A. Soni, *Improved*  
 2224 *methods for observing  $CP$  violation in*  
 2225  *$\mathcal{B} \rightarrow K\bar{D}$  and measuring the CKM phase  $\gamma$* , Physical Review D  
 2226 **63** (2001) 036005.
- 2228 [47] M. Kenzie, M. Martinelli, and N. Tuning, *Estimating*  
 2229  *$r_D$  as an input to the determination of*  
 2230 *the CKM angle  $\gamma$* , Physical Review D **94** (2016)  
 2231 054021.
- 2232 [48] T. Evans, J. Libby, S. Malde, and G. Wilkinson, *Improved sensitivity to the*  
 2233 *CKM phase  $\gamma$  through binning phase space in  $B^- \rightarrow D^- K^+$ ,  $D \rightarrow K^+ \pi^- \pi^- \pi^+$*   
 2234 *decays*, Physics Letters B **802** (2020) 135188.
- 2235 [49] S. Harnew *et al.*, *Model-independent determination of the strong phase*  
 2236 *difference between  $D0$  and  $D^- \rightarrow \pi^+ \pi^- \pi^+ \pi^-$  amplitudes*, Journal of High Energy  
 2237 *Physics* **2018** (2018) 144.
- 2239 [50] R. H. Dalitz, *CXII. On the analysis of  $\tau$ -meson data and the nature of the*  
 2240  *$\tau$ -meson*, The London, Edinburgh, and Dublin Philosophical Magazine and  
 2241 *Journal of Science* **44** (1953) 1068.
- 2242 [51] BaBar Collaboration *et al.*, *Measurement*  
 2243 *of  $\cos 2\beta$  in  $\mathcal{B}^0 \rightarrow D^0 \bar{D}^0$  decays by a combined time-dependent Dalitz plot analysis of BaBar and*  
 2244 *Belle data*, Physical Review D **98** (2018) 112012.

- 2248 [52] S. U. Chung *et al.*, *Partial wave analysis in K-matrix formalism*, Annalen der  
2249 Physik **507** (1995) 404.
- 2250 [53] D. Aston *et al.*, *A study of  $K\pi+$  scattering in the reaction  $K\text{-}p \rightarrow K\pi+n$  at*  
2251 *11 GeV/c*, Nuclear Physics B **296** (1988) 493.
- 2252 [54] A. Bondar, *Proceedings of BINP special analysis meeting on Dalitz analysis,*  
2253 *24-26 Sep. 2002, unpublished.*
- 2254 [55] A. Giri, Y. Grossman, A. Soffer, and J. Zupan,  
2255 *Determining  $\gamma$  using  $B$  with multibody  $D$  decays*, Physical Review D **68** (2003) 054018.
- 2256 [56] BaBar collaboration, B. Aubert *et al.*, *Measurement of the Cabibbo-Kobayashi-*  
2257 *Maskawa angle  $\gamma$  in  $B^\mp \rightarrow D^{(*)}K^\mp$  decays with a Dalitz analysis of  $D \rightarrow$*   
2258  *$K_S^0\pi^-\pi^+$* , Phys. Rev. Lett. **95** (2005) 121802, [arXiv:hep-ex/0504039](https://arxiv.org/abs/hep-ex/0504039).
- 2261 [57] BaBar collaboration, B. Aubert *et al.*, *Improved measurement of the CKM*  
2262 *angle  $\gamma$  in  $B^\mp \rightarrow D^{(*)}K^{(*)\mp}$  decays with a Dalitz plot analysis of  $D$  decays to*  
2263  *$K_S^0\pi^+\pi^-$  and  $K_S^0K^+K^-$* , Phys. Rev. D **78** (2008) 034023, [arXiv:0804.2089](https://arxiv.org/abs/0804.2089).
- 2264 [58] BaBar collaboration, P. del Amo Sanchez *et al.*, *Evidence for direct CP*  
2265 *violation in the measurement of the Cabibbo-Kobayashi-Maskawa angle*  
2266  *$\gamma$  with  $B^\mp \rightarrow D^{(*)}K^{(*)\mp}$  decays*, Phys. Rev. Lett. **105** (2010) 121801,  
2267 [arXiv:1005.1096](https://arxiv.org/abs/1005.1096).
- 2268 [59] Belle collaboration, A. Poluektov *et al.*, *Measurement of  $\phi_3$  with Dalitz*  
2269 *plot analysis of  $B^\pm \rightarrow D^{(*)}K^\pm$  decay*, Phys. Rev. D **70** (2004) 072003,  
2270 [arXiv:hep-ex/0406067](https://arxiv.org/abs/hep-ex/0406067).
- 2271 [60] Belle collaboration, A. Poluektov *et al.*, *Measurement of  $\phi_3$  with Dalitz*  
2272 *plot analysis of  $B^+ \rightarrow D^{(*)}K^{(*)+}$  decay*, Phys. Rev. D **73** (2006) 112009,  
2273 [arXiv:hep-ex/0604054](https://arxiv.org/abs/hep-ex/0604054).
- 2274 [61] Belle collaboration, A. Poluektov *et al.*, *Evidence for direct CP violation in*  
2275 *the decay  $B^\pm \rightarrow D^{(*)}K^\pm$ ,  $D \rightarrow K_S^0\pi^+\pi^-$  and measurement of the CKM phase*  
2276  *$\phi_3$* , Phys. Rev. D **81** (2010) 112002, [arXiv:1003.3360](https://arxiv.org/abs/1003.3360).
- 2277 [62] LHCb collaboration, R. Aaij *et al.*, *Measurement of CP violation and*  
2278 *constraints on the CKM angle  $\gamma$  in  $B^\pm \rightarrow DK^\pm$  with  $D \rightarrow K_S^0\pi^+\pi^-$  decays*,  
2279 Nucl. Phys. B **888** (2014) 169, [arXiv:1407.6211](https://arxiv.org/abs/1407.6211).

- 2280 [63] LHCb collaboration, R. Aaij *et al.*, *Measurement of the CKM angle  $\gamma$  using  $B^0 \rightarrow DK^{*0}$  with  $D \rightarrow K_S^0\pi^+\pi^-$  decays*, JHEP **08** (2016) 137, arXiv:1605.01082.
- 2281  
2282
- 2283 [64] A. Bondar and A. Poluektov, *Feasibility study of model-independent approach to  $\Phi_3$  measurement using Dalitz plot analysis*, The European Physical Journal C - Particles and Fields **47** (2006) 347.
- 2284  
2285
- 2286 [65] A. Bondar and A. Poluektov, *The use of quantum-correlated  $D0$  decays for  $\Phi_3$  measurement*, The European Physical Journal C **55** (2008) 51.
- 2287
- 2288 [66] Belle collaboration, H. Aihara *et al.*, *First measurement of  $\phi_3$  with a model-independent Dalitz plot analysis of  $B^\pm \rightarrow DK^\pm$ ,  $D \rightarrow K_S^0\pi^+\pi^-$  decay*, Phys. Rev. **D85** (2012) 112014, arXiv:1204.6561.
- 2289  
2290
- 2291 [67] LHCb collaboration, R. Aaij *et al.*, *A model-independent Dalitz plot analysis of  $B^\pm \rightarrow DK^\pm$  with  $D \rightarrow K_S^0h^+h^-$  ( $h = \pi, K$ ) decays and constraints on the CKM angle  $\gamma$* , Phys. Lett. **B718** (2012) 43, arXiv:1209.5869.
- 2292  
2293
- 2294 [68] A. Poluektov, *Unbinned model-independent measurements with coherent admixtures of multibody neutral  $D$  meson decays*, The European Physical Journal C **78** (2018) 121.
- 2295  
2296
- 2297 [69] CLEO Collaboration *et al.*, *Model-independent determination of the strong-phase difference between  $\hat{D}^0$  and  $\hat{\bar{D}}^0$  and its impact on the measurement of the CKM angle  $\gamma/\phi_3$* , Physical Review D **82** (2010) 112006.
- 2298  
2299  
2300  
2301  
2302
- 2303 [70] M. Ablikim *et al.*, *Model-independent determination of the relative strong-phase difference between  $D\bar{D}$  and  $\bar{D}\bar{D}$  and its impact on the measurement of the CKM angle  $\gamma/\phi_3$* , arXiv:2003.00091 [hep-ex] (2020) arXiv:2003.00091.
- 2304  
2305  
2306
- 2307 [71] R. Aaij *et al.*, *Near-threshold  $DD^-$  spectroscopy and observation of a new charmonium state*, Journal of High Energy Physics **2019** (2019) 35.
- 2308  
2309

- [72] C. Thomas and G. Wilkinson, *Model-independent  $\{D\bar{D}\}$ -mixing and  $CP$  violation studies with  $\{D\bar{D}\}$  to  $K_{\mathrm{S}}\bar{K}_{\mathrm{S}}$  and  $K_{\mathrm{L}}\bar{K}_{\mathrm{L}}$* , Journal of High Energy Physics **2012** (2012) 185.
- [73] LHCb collaboration, R. Aaij *et al.*, *Measurement of the CKM angle  $\gamma$  using  $B^\pm \rightarrow DK^\pm$  with  $D \rightarrow K_{\mathrm{S}}^0 \pi^+ \pi^-$ ,  $K_{\mathrm{S}}^0 K^+ K^-$  decays*, JHEP **10** (2014) 097, arXiv:1408.2748.
- [74] Y. Grossman and M. Savastio, *Effects of  $K - \bar{K}$  mixing on determining gamma from  $B \rightarrow DK$* , Journal of High Energy Physics **2014** (2014), arXiv:1311.3575.
- [75] J. Garra Ticó, *A strategy for a simultaneous measurement of  $CP$  violation parameters related to the CKM angle  $\gamma$  in multiple  $B$  meson decay channels*, arXiv:1804.05597.
- [76] Particle Data Group, P. A. Zyla *et al.*, *Review of particle physics*, Prog. Theor. Exp. Phys. **2020** (2020) 083C01.
- [77] A. Pais and O. Piccioni, *Note on the Decay and Absorption of the  $\theta$* , Physical Review **100** (1955) 1487.
- [78] M. L. Good, *Relation between Scattering and Absorption in the Pais-Piccioni Phenomenon*, Physical Review **106** (1957) 591.
- [79] W. Fetscher *et al.*, *Regeneration of arbitrary coherent neutral kaon states: A new method for measuring the  $K\bar{K} - \bar{K}\bar{K}$  forward scattering amplitude*, Zeitschrift für Physik C: Particles and Fields **72** (1996) 543.
- [80] E. Kou *et al.*, *The Belle II Physics Book*, Progress of Theoretical and Experimental Physics **2019** (2019) 123C01, arXiv:1808.10567.
- [81] LHCb collaboration *et al.*, *Physics case for an LHCb Upgrade II - Opportunities in flavour physics, and beyond, in the HL-LHC era*, arXiv:1808.08865 [hep-ex] (2019) arXiv:1808.08865.
- [82] I. I. Bigi and H. Yamamoto, *Interference between Cabibbo allowed and doubly forbidden transitions in  $D \rightarrow KS, L + i's$  decays*, Physics Letters B **349** (1995) 363.

- [83] CLEO Collaboration *et al.*, *Comparison of  $\bar{D} \rightarrow K_S \pi^0$  and  $\bar{D} \rightarrow K_L \pi^0$  Decay Rates*, Physical Review Letters **100** (2008) 091801.
- [84] Y. Grossman and Y. Nir, *CP violation in  $T^\pm \rightarrow i^\pm KS$  and  $D^\pm \rightarrow i^\pm KS$ : The importance of  $KS$ -  $KL$ interference*, Journal of High Energy Physics **2012** (2012) 2.
- [85] G. A. Cowan, D. C. Craik, and M. D. Needham, *RapidSim: An application for the fast simulation of heavy-quark hadron decays*, Computer Physics Communications **214** (2017) 239.
- [86] LHCb collaboration, *LHCb reoptimized detector design and performance: Technical Design Report*, Tech. Rep. CERN-LHCC-2003-030, LHCb-TDR-9, CERN, Geneva, 2003.
- [87] J. Gassner, M. Needham, and O. Steinkamp, *Layout and Expected Performance of the LHCb TT Station*, Tech. Rep. LHCb-2003-140, CERN, Geneva, 2004.
- [88] Belle Collaboration, A. B. Kaliyar *et al.*, *Measurements of branching fraction and direct cp asymmetry in  $B^\pm \rightarrow K_S^0 K_S^0 K^\pm$  and a search for  $B^\pm \rightarrow K_S^0 K_S^0 \pi^\pm$* , Phys. Rev. D **99** (2019) 031102.
- [89] N. Hiroshi, *Search for new physics by a time-dependent CP violation analysis of the decay  $B \rightarrow K_S^0$  eta gamma using the Belle detector*, PhD thesis, Tohoku University, Senday, 2015.
- [90] A. Gsponer *et al.*, *Precise Coherent  $K_S^0$  Regeneration Amplitudes for C, Al, Cu, Sn, and Pb Nuclei from 20 to 140 GeV/c and Their Interpretation*, Phys. Rev. Lett. **22** (1979) 13.
- [91] R. A. Briere and B. Weinstein, *Determining the Phase of a Strong Scattering Amplitude from Its Momentum Dependence to Better Than 1°: The Example of Kaon Regeneration*, Phys. Rev. Lett. **75** (1995) 402.
- [92] B. R. Ko, E. Won, B. Golob, and P. Pakhlov, *Effect of nuclear interactions of neutral kaons on cp asymmetry measurements*, Phys. Rev. D **84** (2011) 111501.
- [93] LHCb collaboration, *LHCb RICH1 Engineering Design Review Report*, Tech. Rep. LHCb-2004-121, CERN, Geneva, 2004.

- 2374 [94] LHCb Collaboration, *LHCb VELO Upgrade Technical Design Report*, Tech.  
2375 Rep. CERN-LHCC-2013-021. LHCB-TDR-013, 2013.
- 2376 [95] LHCb Collaboration, *LHCb PID Upgrade Technical Design Report*, Tech.  
2377 Rep. CERN-LHCC-2013-022. LHCB-TDR-014, 2013.
- 2378 [96] LHCb collaboration, R. Aaij *et al.*, *Measurement of the CKM angle  $\gamma$  from a*  
2379 *combination of LHCb results*, JHEP **12** (2016) 087, arXiv:1611.03076.
- 2380 [97] D. J. Lange, *The EvtGen particle decay simulation package*, Nucl. Instrum.  
2381 Meth. **A462** (2001) 152.
- 2382 [98] LHCb collaboration, M. W. Kenzie and M. P. Whitehead, *Update of the LHCb*  
2383 *combination of the CKM angle  $\gamma$* , LHCB-CONF-2018-002, 2018.
- 2384 [99] P. K. Resmi, J. Libby, S. Malde, and G. Wilkinson, *Quantum-correlated mea-*  
2385 *surements of  $D \rightarrow K_S^0 \pi^+ \pi^- \pi^0$  decays and consequences for the determination*  
2386 *of the CKM angle  $\gamma$* , JHEP **01** (2018) 082, arXiv:1710.10086.
- 2387 [100] L. Breiman, J. H. Friedman, R. A. Olshen, and C. J. Stone, *Classification and*  
2388 *regression trees*, Wadsworth international group, Belmont, California, USA,  
2389 1984.
- 2390 [101] H. Voss, A. Hoecker, J. Stelzer, and F. Tegenfeldt, *TMVA - Toolkit for*  
2391 *Multivariate Data Analysis with ROOT*, PoS **ACAT** (2007) 040.
- 2392 [102] A. Hoecker *et al.*, *TMVA 4 — Toolkit for Multivariate Data Analysis with*  
2393 *ROOT. Users Guide.*, arXiv:physics/0703039.
- 2394 [103] L. Anderlini *et al.*, *The PIDCalib package*,  
2395 <https://cds.cern.ch/record/2202412>, 2016.
- 2396 [104] W. Verkerke and D. P. Kirkby, *The RooFit toolkit for data modeling*, eConf  
2397 **C0303241** (2003).
- 2398 [105] T. Skwarnicki, *A study of the radiative cascade transitions between the Upsilon-*  
2399 *prime and Upsilon resonances*, PhD thesis, Institute of Nuclear Physics,  
2400 Krakow, 1986, DESY-F31-86-02.
- 2401 [106] LHCb collaboration, R. Aaij *et al.*, *Dalitz plot analysis of  $B^0 \rightarrow \bar{D}^0 \pi^+ \pi^-$*   
2402 *decays*, Phys. Rev. **D92** (2015) 032002, arXiv:1505.01710.

- 2403 [107] LHCb collaboration, R. Aaij *et al.*, *Constraints on the unitarity triangle angle*  
2404  $\gamma$  *from Dalitz plot analysis of  $B^0 \rightarrow DK^+\pi^-$  decays*, Phys. Rev. **D93** (2016)  
2405 112018, Erratum *ibid.* **D94** (2016) 079902, [arXiv:1602.03455](https://arxiv.org/abs/1602.03455).
- 2406 [108] LHCb collaboration, R. Aaij *et al.*, *Measurement of CP observables in*  
2407  $B^\pm \rightarrow D^{(*)}K^\pm$  *and  $B^\pm \rightarrow D^{(*)}\pi^\pm$  decays*, Phys. Lett. **B777** (2017) 16,  
2408 [arXiv:1708.06370](https://arxiv.org/abs/1708.06370).
- 2409 [109] LHCb collaboration, R. Aaij *et al.*, *Dalitz plot analysis of  $B_s^0 \rightarrow \bar{D}^0 K^- \pi^+$*   
2410 *decays*, Phys. Rev. **D90** (2014) 072003, [arXiv:1407.7712](https://arxiv.org/abs/1407.7712).